

5 RESEARCH ACTIVITIES

5.1 NUCLEAR PHYSICS

N. Madhavan

The first set of experiments using the recently commissioned National Array of Neutron Detectors (NAND) facility with 100 detectors was carried out in the just concluded LINAC cycle. The efficacy of the shielding of NAND beam dump and the VME based data acquisition system had successfully been tested prior to these experiments. Quasi-elastic back scattering measurements were also carried out in NAND chamber using several hybrid telescope detectors, to extract barrier distributions in highly fissile, heavy nuclei.

The second stage of HYbrid Recoil mass Analyzer (HYRA) has been aligned and vacuum tested. The first (gas-filled) stage of HYRA was used in five experiments last year with most of the measurements done in conjunction with the TIFR 4π spin spectrometer. There are indications that a gas-filled separator, such as the first stage of HYRA, is ideally suited for evaporation residue (ER) cross section measurements in heavy mass regions where long-lived isomers are present, in comparison with measurements made using a vacuum mode spectrometer such as HIRA. This is mainly due to the continuous reset of charge state of residues in a gas-filled separator which circumvents the need for charge state reset foil beyond the target, while preventing the loss in transport efficiency (usually arising from multiple-Auger processes following internal conversion).

Germanium Clover detectors (INGA pool) of other institutes are expected to be shipped to IUAC soon in order to start the INGA-HYRA campaign. Steps are being taken to have adequate number of Clover germanium detectors at IUAC in order to continuously cater to spectroscopic studies.

First phase facilities, HIRA, GDA and GPSC have been utilised in several user experiments, in the past year. ER cross sections could be measured extending well below the Coulomb barrier using HIRA, within the allotted beam time, due to stabilized, uninterrupted power and the migration to 0.5 μm thick window foil for the large area MWPC (focal plane) detector. Reaction based experiments carried out at GPSC include mass and angular distributions in fission reactions and incomplete fusion (ICF) studies. Spectroscopic studies carried out include g-factor and lifetime measurements.

Superdeformed band has been observed, for the first time in the country, by I. Mazumdar et al. This recent result in ^{133}Nd nucleus was the outcome of a short experiment carried out during last INGA campaign at IUAC.

A new isomeric state has been observed in ^{195}Bi nucleus, above the known 750 ns isomeric state, in an experiment at the focal plane of HYRA using a single Clover germanium detector by recording individual crystal signals. The primary beam rejection, efficiency and selectivity of gas-filled mode of HYRA enabled the success of this study even with limited beam current.

T. Banerjee et al., have carried out systematic calculations using published ER cross-sections for several heavy systems to explain the collective role of fissility, entrance channel mass asymmetry and charge product of colliding nuclei on fusion probability in order to understand the limitations of statistical model and onset of dynamical effects.

Dr. Maninder Kaur (Ph. D. student of Dr. Bivash R. Behera, Panjab University and presently teaching at SGTB, Khalsa College, Punjab) won the Best Poster Prize in the 12th International Conference on Nucleus-Nucleus Collisions held during June 21-26, 2015 at Catania, Italy, based on her thesis work carried out using HIRA and 14 BGO detectors at IUAC. We wish her many more laurels in her academic career.

5.1.1 RDM lifetime measurements in Pd nuclei with mass ~ 100

C.K. Gupta¹, Aman Rohilla¹, R.P. Singh², S. Muralithar², S. Chakraborty³, Siddharth Rai⁴, H.P. Sharma³, A. Kumar⁵, I.M. Govil⁵ and S.K. Chamoli¹

¹Department of Physics and Astrophysics, University of Delhi, Delhi 110007, India

²Inter University Accelerator Centre, Aruna Asaf Ali Marg, New Delhi 110067, India

³Department of Physics, Banaras Hindu University, Varanasi 221005, India

⁴Department of Physics, VisvaBharati, Santiniketan 731235, India

⁵Department of Physics, Panjab University, Chandigarh 160014, India

In the transitional nuclei of ~ 100 mass region, many interesting properties, like magnetic rotation (MR), anti-magnetic rotation (AMR) and chirality are found at high spin states. To understand the properties of transitional nuclei at high spin, a “tidal wave model” based on cranking mean field theory has been developed by S. Frauendorf [1,2]. This model has been already proved in the low spin states of this mass region but to prove the model at high spin, the B(E2) of the high spin states are highly desirable. Recently, DSAM lifetime measurements of the high spin states in ¹⁰²Pd have been done by Ayangeakaa and Garg et al. [3], which provided the B(E2) values up to I = 16⁺ excited states. However, the B(E2) data of 2⁺ and 4⁺ excited states were taken from reference [4]. So for explaining the properties of ¹⁰²Pd nucleus within the tidal wave model, the low spin data is highly important. By keeping this motivation in mind, excited states of Pd nuclei with mass ~100 were populated via ⁹⁴Zr(¹²C, 4n)¹⁰²Pd reaction, at a beam energy of 57 MeV. A sandwiched evaporated target [5] consisting of 520 μg/cm² thick ⁹⁴Zr backed by a 3.5 mg/cm² thick Ta with a coating of a thin gold layer has been used in this experiment. The results of the preliminary data analysis are very encouraging and hopefully we will be able to find lifetime of some high spin states of ¹⁰²Pd nucleus. Fig. 5.1.1 shows the nature of shifted and the unshifted peaks, for different target-stopper distances, of 556 keV (2⁺ → 0⁺), peak of yrast band in ¹⁰²Pd and the partial level scheme of yrast band of ¹⁰²Pd.

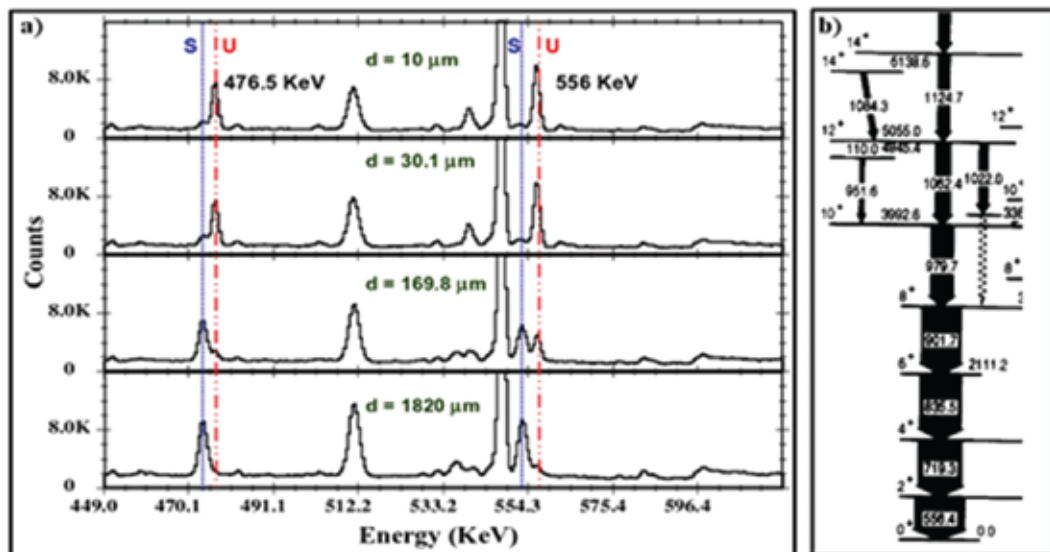


Fig. 5.1.1. (a) The shifted and unshifted peaks of γ -ray transitions in ¹⁰²Pd yrast band at different target to stopper distances obtained with a gamma detector at a backward angle of 144° with respect to the beam direction and (b) a partial level scheme of yrast band of ¹⁰²Pd.

References

- [1] S. Frauendorf, Y. Gu, and J. Sun, arXiv:0709.0254.
- [2] S. Frauendorf, Y. Gu and J. Sun, *Int. J. Mod. Phys. E* **20**, 465 (2011).
- [3] D. Ayangeakaa, U. Garg *et al.*, *Phys. Rev. Lett.* **110**, 102501 (2013).
- [4] D. D. Frenne, *Nucl. Data Sheets* **110**, 1745 (2009).
- [5] C.K. Gupta, et al., *Nucl.Instrum.Meth.A* **764**, 273 (2014).

5.1.2 Studying the superdeformed band in ^{133}Nd

I. Mazumdar¹, S. Roy¹, P. K. Joshi¹, S. Muralithar², R. P. Singh² and S. S.Ghugre³

¹Dept. of Nuclear and Atomic Physics, Tata Institute of Fundamental Research, Mumbai-400005, India

²Inter University Accelerator Centre, Aruna Asaf Ali Marg, New Delhi 110067, India

³UGC-DAE CSR, Kolkata Centre, Sector III, LB-8, Bidhan Nagar, Kolkata 700098, India

Since its first observation in the mid-eighties the studies in super deformed (SD) bands in rotating nuclei continue to be an important topic of research in nuclear structure [1]. Over the last three decades more than three hundred SD bands have been seen in different nuclei across the nuclear landscape. Notwithstanding the enormous data collected so far, the exact mechanisms of the formation, decay and linking of SD bands with normal deformed (ND) bands are yet to be fully understood.

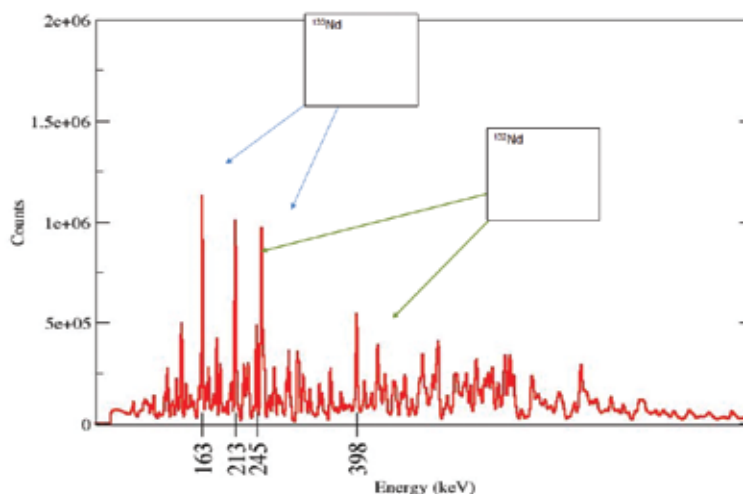


Fig.5.1.2 Total Projection.

We have initiated a programme to study the underlying mechanism governing the feeding and decay of superdeformed bands in the atomic nuclei. We plan to carry out a series of experiments to measure the feeding intensity of the superdeformed band in ^{133}Nd using different target-projectile combinations. The primary objective is to investigate the role of entrance channel effect in the feeding and decay of the SD band. The isotopes in the Ce-Nd region are particularly of interest for populating the SD bands with unusually large intensities compared to SD bands in other mass regions. The relative intensity of the SD band in ^{133}Nd has been reported to be reaching up to ~20% [1-2]. Such large feeding intensity of the SD band in ^{133}Nd produced in heavy-ion induced fusion-evaporation reaction remains an outstanding problem. As a first step in our investigation, an experiment was carried out at the IUAC, New Delhi. A 1.1mg/cm² thick, self-supporting ^{104}Pd target was bombarded by 135MeV ^{32}S beam from the IUAC Pelletron accelerator. The decay of the ^{136}Sm compound nucleus produces four major evaporation residues with significantly high

cross-sections, namely, ^{133}Pm , ^{133}Nd , ^{132}Nd and ^{130}Pr . The gamma rays were detected using the Indian National Gamma Array [3]. In this run, 13 Clover detectors placed at 32° , 57° , 90° , 123° and 148° with respect to the beam direction were used. A total of 500 million γ - γ coincidence events were collected over a period of two days. The analysis has been completed and all the major characteristic gamma rays from the dominant evaporation residues have been identified. Here we discuss the γ -rays observed from the super deformed and the normal deformed bands of ^{133}Nd . Fig. 5.1.2 shows the ground state transitions in ^{133}Nd and ^{132}Nd in the total projection spectrum. We have generated all the known bands of ^{133}Nd and have extracted their intensities from our analysis. Fig. 5.1.3 shows the extracted level scheme of ^{133}Nd . The bands of ^{133}Nd show the presence of normal deformation, γ -soft triaxiality and super deformation. Bands 1 and 2 are negative parity bands with similar configurations. Band 9 is positive parity and the two branches are signature partners. We have observed the SD band in ^{133}Nd from our analysis. Fig. 5.1.4 shows the spectrum gated over the two lowest transitions of the SD band, namely, 345 and 441 keV. The gated spectrum shows the known intra- and inter-band transitions of the SD band. Fig. 5.1.5 shows the SD band along with the linking transitions to the normal deformed bands. We have also determined the relative intensities of the transitions in the SD band. In conclusion we have carried out spectroscopy of ^{133}Nd and have observed the SD band with all the known transitions. As a next step we plan to carry out another measurement with more symmetric target projectile combination and compare the relative intensities of the SD band with the values obtained from the present measurement.

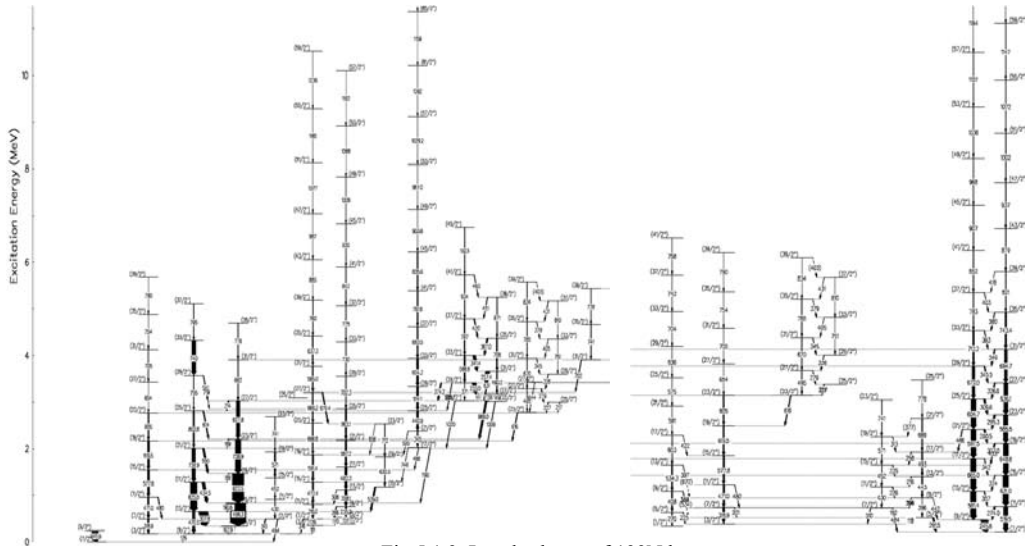
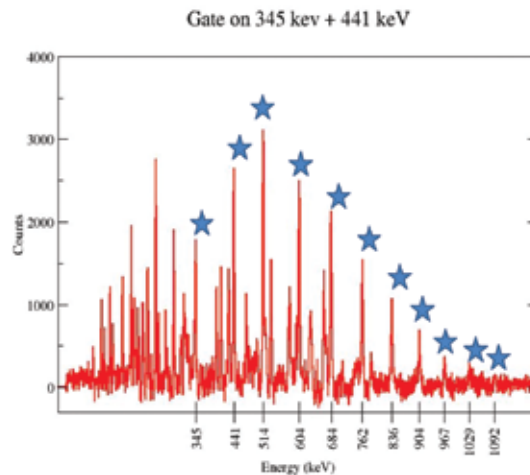
Fig.5.1.3 Level scheme of ^{133}Nd .

Fig. 5.1.4 Gated spectra showing all the intra band transition of the SD band.

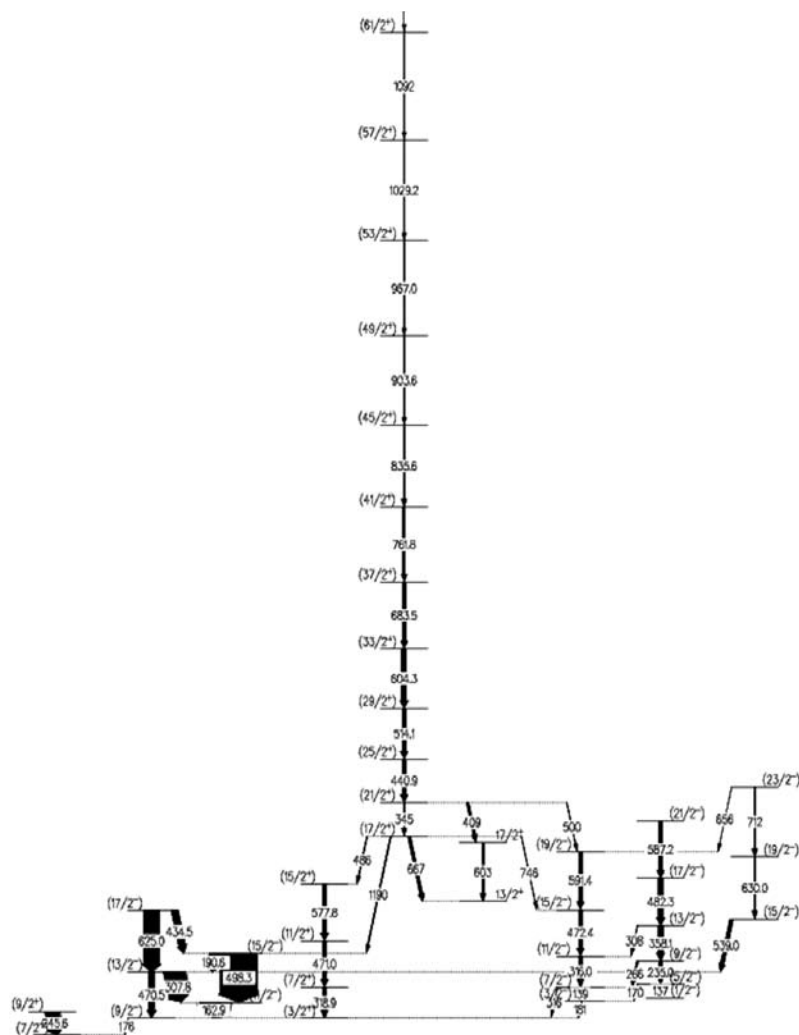


Fig. 5.1.5 Level scheme showing the SD band and linking transitions.

REFERENCES

- [1] P. J. Nolan and P. J. Twin *Ann. Rev. Nucl. Part. Sci.* **38**, 533 (1988).
- [2] D. Bazzacco *et. al.*, *Phys. Rev. C* **49**, R2281, (1994).
- [3] S. Muralithar *et. al.*, *Nucl.Instrum.Meth.A* **622**, 281 (2010).

5.1.3 Fission fragment mass distributions for ^{200}Pb

G. Mohanto¹, P.Sugathan², A. Jhingan², Saneesh N.², Tathagata Banerjee², Rakesh Dubey², IshMukul², MeenuThakur³, Gurpreet Kaur³, Ruchi Mahajan³, Maninder Kaur³, P. Laveen⁴, S. Nath³, N. Madhavan³ and A Roy⁵

¹Nuclear Physics Division, Bhabha Atomic Research Centre, Trombay, Mumbai 400085, India

²Nuclear physics Group, Inter University Accelerator Centre, ArunaAsaf Ali Marg, New Delhi 110067, India

³Department of Physics, Panjab University, Chandigarh160014, India

⁴Department of Physics, School of Mathematical and Physical Sciences, Central University of Kerala, Kasaragod 671314, India

⁵Variable Energy Cyclotron Centre, 1/AF, Bidhannagar, Kolkata 700064, India

Nuclear fission has been very intensively studied since it was discovered 75 years back. Fission is one of the major hurdles in heavy element production. In fusion fission the compound nucleus (CN) undergoes fission and heavy residue production is hindered. Moreover, in the last two decades another mode of fission, which is faster than fusion-fission, has been observed. This is known as quasi-fission [1,2] and it makes heavy element formation even a bigger challenge. In this case, fission takes place even before the CN is formed. The reaction mechanism and the parameters that influence quasi fission are not well understood. There are a few signatures of quasi-fission that are being studied to get a clearer picture about quasi fission. Fission fragment mass distribution is one such tool that can be used to study quasi fission contribution, where presence of quasi fission is reflected in wider mass distribution [3]. Earlier we reported comparison of evaporation residue spin distributions for $^{16}\text{O} + ^{184}\text{W}$, $^{19}\text{F} + ^{181}\text{Ta}$ and $^{30}\text{Si} + ^{170}\text{Er}$, forming CN ^{200}Pb . Results showed lower average spin for $^{30}\text{Si} + ^{170}\text{Er}$ than that of other two systems [4]. This was attributed to possible presence of quasi fission. To investigate the role of quasi fission, we measured fission fragment mass distributions for $^{16}\text{O} + ^{184}\text{W}$ and $^{30}\text{Si} + ^{170}\text{Er}$.

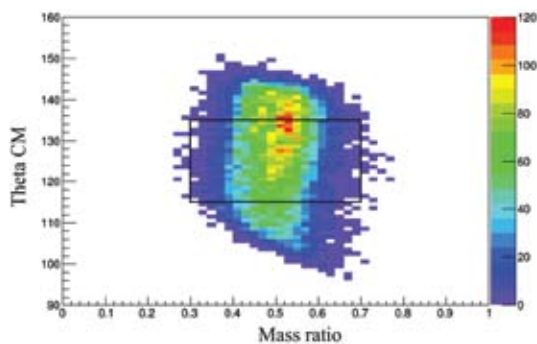


Fig. 5.1.6 Mass angle distribution for $^{30}\text{Si} + ^{170}\text{Er}$.

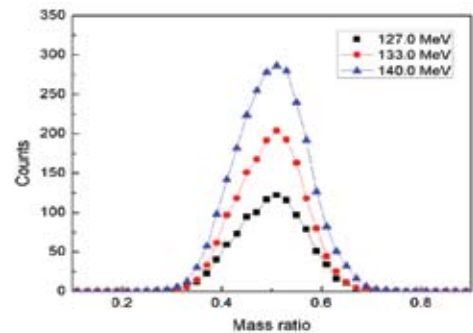


Fig. 5.1.7 Mass distribution for $^{30}\text{Si} + ^{170}\text{Er}$.

For this experiment we used beams of ^{16}O (78 to 108 MeV) and ^{30}Si (122 to 140 MeV) with repetition rate of 250 ns. Isotopically enriched targets of ^{184}W (100 $\mu\text{g}/\text{cm}^2$ on 30 $\mu\text{g}/\text{cm}^2$ C) and ^{170}Er (130 $\mu\text{g}/\text{cm}^2$ thick, sandwiched between 43 and 23 $\mu\text{g}/\text{cm}^2$ C) were prepared at target laboratory of IUAC. The experiment was performed in the General Purpose Scattering Chamber (GPSC) using two position sensitive multi-wire proportional counters (MWPC) of area $20 \times 10 \text{ cm}^2$. Two detectors were placed at folding angle. The positions (X and Y), time of flight (TOF) and energy signals were collected. Fission fragments were separated from other events in TOF coincidence spectrum. For beam monitoring, two silicon surface barrier detectors (SSBD) were placed at angles of $\pm 10^\circ$ with respect to beam direction. The data acquisition system was triggered by either of the fission fragments. The mass ratio ($m_r = m_1 / (m_1 + m_2)$) was obtained using the formula $m_r = v_1 / (v_1 + v_2)$, where v_1 and v_2 are velocities of two fragments in center of mass frame. Mass angle distribution (Fig. 5.1.6) was extracted by calculating the centre of mass angle $\theta_{\text{c.m.}}$. The mass ratio distributions (Fig. 5.1.7) were extracted for these two reactions and fitted with Gaussian functions. Widths of the mass distributions were extracted from the fits. Preliminary analysis shows indication of quasi fission in case of reaction $^{30}\text{Si} + ^{170}\text{Er}$ which is in agreement with the explanation given in our previous report.

REFERENCES

- [1] S. Bjornholm and W. J. Swiatecki, Nucl. Phys. A **391**, 471 (1982).
- [2] W. J. Swiatecki, Phys. Scr. **24**, 113 (1981).
- [3] R. Rafiei *et al.*, Phys. Rev. C **77**, 024606 (2008).
- [4] Gayatri Mohanto *et al.*, Nucl. Phys. A **890-891**, 62 (2012).

5.1.4 Excitation functions in $^{13}\text{C}+^{169}\text{Tm}$: A low energy incomplete fusion process

Vijay R. Sharma¹, Mohd. Shuaib¹, A. Yadav², P. P. Singh³, I. Bala², S. Gupta⁴, M. K. Sharma⁵, D. P. Singh⁶, R. Kumar², S. Muralithar², B. P. Singh¹, R. P. Singh², R. Prasad¹ and R. K. Bhowmik²

¹Accelerator Laboratory, Department of Physics, Aligarh Muslim University, Aligarh 202002, India

²Inter University Accelerator Centre, ArunaAsaf Ali Marg, New Delhi 110067, India

³Department of Physics, Indian Institute of Technology Ropar, Punjab 140001, India

⁴Physics Department, Agra College, Agra 282001, India

⁵Physics Department, S.V. College, Aligarh 202001, India

⁶Department of Physics, University of Petroleum Studies, Dehradun, UK 248007, India

In recent reports, incomplete fusion (ICF) has been found to be a significant contributor in light-heavy ion induced reactions even at slightly above barrier energies [1,2]. For better insights into the dynamics of ICF, the onset and influence of ICF need to be further investigated in terms of projectile energy (E_{lab}) and entrance channel mass-asymmetry (μ_A). A rich set of experimental data on ICF is in order to correlate the probability of ICF with the various entrance channel parameters, and eventually to develop a theoretical model code to predict ICF probability at low incident energies. Presently, there is no theoretical model code available which can explain low-energy ICF data. In this report, the excitation functions (EFs) of a number of complete fusion (CF) and ICF residues populated in the $^{13}\text{C}+^{169}\text{Tm}$ system have been measured using the activation technique followed by offline γ -spectroscopy. The evaporation residues have been identified on the basis of characteristic γ -lines and confirmed through the decay-curve analysis. In Fig. 5.1.8, the EFs for the xnand pxnchannels (i.e. σ_{CF}) are found to be in good agreement with the statistical model code PACE4 [3]; this suggests the population of these channels via CF only. The residue ^{177}W was found to have contribution from its precursor decay (i.e. the β -emission). The precursor contribution has been deduced from the cumulative cross section of the residue using the standard successive radioactive decay formulations [4]. The experimentally measured cross-sections of α -emitting channels have been found to be significantly enhanced as compared to the theoretical model predictions PACE4. This enhancement may be attributed to some physical effect which is not incorporated in PACE4 i.e. ICF processes. In Fig. 5.1.9 (a-b), experimentally and systematically deduced ICF strength function (F_{ICF}) for $^{13}\text{C}+^{169}\text{Tm}$ is compared with that obtained in $^{12}\text{C}+^{169}\text{Tm}$ system [5]. The x-axis observables are to incorporate the effect of Coulomb barrier. It has been found that one-neutron (1n) excess projectile ^{13}C (as compared to ^{12}C) results in a less ICF contribution due to its relatively large negative alpha-Q value. Recently proposed ‘‘alpha-Q-value systematics’’ [2] seems to explain ICF data satisfactorily. Detailed results and discussions are documented in ref. [1].

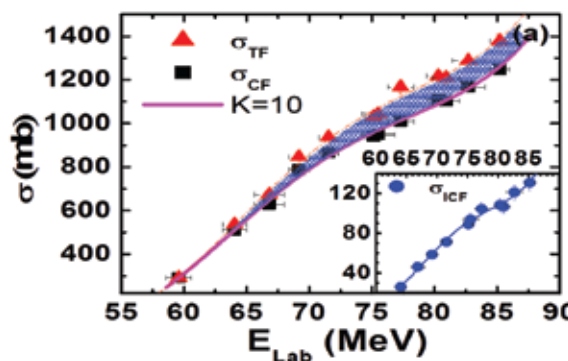


Fig. 5.1.8 Experimental EFs of CF events along with the total fusion and incomplete fusion events.

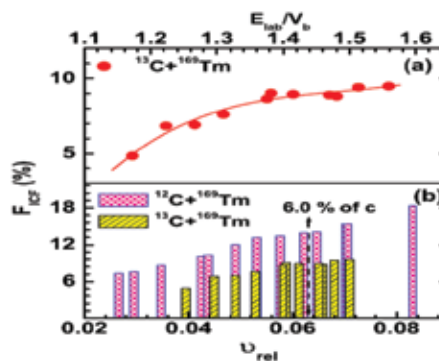


Fig. 5.1.9(a) Systematically deduced FICF as a function of normalized projectile energy. The lines and curves are drawn to guide the eyes. (b) the values of FICF are compared for $^{13,12}\text{C}+^{169}\text{Tm}$ systems as a function of relative velocity (v_{rel}/c).

REFERENCES

- [1] Vijay R. Sharma *et al.*, Phys. Rev C **89**, 024608 (2014).
 [2] Abhishek Yadav *et al.*, Phys. Rev. C **86**, 014603 (2012).
 [3] O.B. Tarasov and D. Bazin, Nucl. Instrum.Meth.B **204**, 174 (2003).
 [4] Unnatiet al., Nucl. Phys.A **811**, 77 (2008).
 [5] Pushpendra P. Singh *et al.*, J. Phys. Conf. Ser. **282**, 012019 (2011).

5.1.5 Angular distribution of fission fragments in $^{19}\text{F}+^{206}\text{Pb}$ reaction

R. Dubey¹, G. Kaur², Tathagata Banerjee¹, Abhishek Yadav¹, N. Saneesh¹, M. Thakur², A. Jhingan¹ and P. Sugathan¹

¹Inter University Accelerator Centre, ArunaAsaf Ali Marg, New Delhi 110067, India

²Department of Physics, Panjab University, Chandigarh 160014, India

The dynamics involved in the fission of heavy nucleus formed in heavy ion induced fusion reaction can be influenced by entrance channel mass asymmetry, Coulomb factor $Z_p Z_T$, deformation (shape), size of the reacting partners and their relative kinetic energy. Apart from these, the spin of the projectile and/or target and the shell closure of the compound system may also play significant role in the fission decay modes. In the present work, we try to investigate the role of entrance channel variables on angular distribution of fission fragments measured in the reaction of $^{19}\text{F}+^{206}\text{Pb}$ around sub barrier energies. The angular anisotropy measured in $^{19}\text{F}+^{206}\text{Pb}$ reaction has been compared with existing data for $^{16}\text{O} + ^{209}\text{Bi}$ reaction [1]. In the case of $^{19}\text{F}+^{206}\text{Pb}$ reaction, the projectile has prolate deformation (0.275) and ground state spin $\frac{1}{2}$ as compared to ^{16}O projectile which is spherical with ground state spin 0.

The angular distribution measurements were performed using the 15UD Pelletron accelerator facility at IUAC. DC beam of ^{19}F with energies ranging from 80 MeV to 112 MeV was used to bombard isotopically enriched ^{206}Pb target. The fission fragments were detected using the HYTAR (Hybrid Telescope ARray) detector setup, in which individual detectors were placed 10° apart. The hybrid detector is a combination of gas ionization chamber (ΔE detector) and silicon detector (E detector). The gas detector has 18 mm active depth and was operated at 90 mbar of isobutane gas. The thickness of silicon detector is 300 μm which is sufficient to completely stop the fragments and recoil particles. The telescope had 7 mm aperture with angular opening of 1.5° . The experimentally measured fission fragment angular distributions were transformed from laboratory frame to center-of-mass frame using Viola systematics for symmetric fission. The normalized fission yields are calculated as a function of angle at each energy point. Rutherford scattering events in the monitor detectors were used for the normalization to obtain the fission angular distribution.

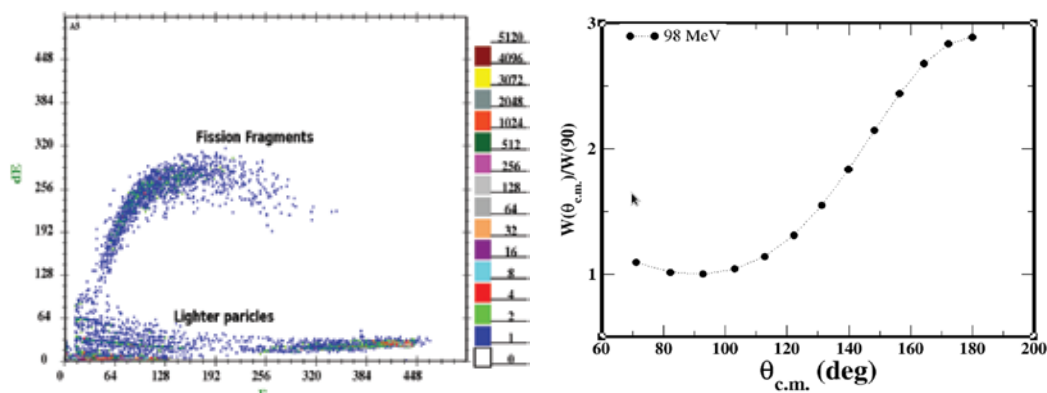


Fig. 5.1.10 (left) Particle identification spectrum from the telescope detector at 150° and (right) the fission fragment angular distributions for the $^{19}\text{F}+^{206}\text{Pb}$ reaction at $E_{\text{lab}}=98$ MeV.

Preliminary analysis shows that, angular anisotropy for the reaction $^{19}\text{F}+^{206}\text{Pb}$ (Fig. 5.1.10) is similar to the one observed in reaction $^{16}\text{O}+^{209}\text{Bi}$ indicating that ground state spin and deformation carried by projectile has little influence on the fusion-fission mechanism.

REFERENCE

- [1] A. M. Samant et al., Eur. Phys. J. A 7, 59 (2000).

5.1.6 Measurement of neutron multiplicity from fission of ^{227}Pa

N. Saneesh¹, Meenu Thakur², Ruchi Mahajan², Gurpreet Kaur², Kushal Kapoor², Priya Sharma², G. Mohanto¹, Davinder Siwal¹, R. Dubey¹, Tathagata Banerjee¹, N. Kumar³, Khushboo³, S. Goyal³, M. Shareef⁴, H. Singh⁵, B. R. Behera², A. Jhingan¹, A. Chatterjee¹ and P. Sugathan¹

¹Inter University Accelerator Centre, ArunaAsaf Ali Marg, New Delhi 110067, India

²Department of Physics, Panjab University, Chandigarh 160014, India

³Department of Physics, Delhi University, Delhi 110007, India

⁴Department of Physics, School of Mathematical and Physical Sciences, Central University of Kerala, Kasaragod 671314, India

⁵Department of Physics, Kurukshetra University, Haryana 136119, India

Neutron time of flight (TOF) measured in coincidence with fission fragments allows to determine the pre (v_{pre}) and post (v_{post}) scission neutron multiplicities in fusion-fission reactions which carries vital information regarding reaction dynamics [1]. Neutron multiplicity from fission of ^{227}Pa , formed by the reaction $^{19}\text{F}+^{208}\text{Pb}$, at an excitation energy of 50 MeV, has been measured using National Array of Neutron Detectors (NAND) facility at IUAC [2]. Fission fragments were detected by two multi-wire proportional counters (MWPC) mounted at 40° and 120° on either side w.r.t beam direction. The neutron detectors were mounted on a geodesic dome structure both in plane and out of plane positions giving a flight path of 175 cm. The threshold for neutron detectors was set to ~ 300 keV. TOF spectrum from one of the neutron detectors is shown in Fig. 5.1.11. The fission fragments were identified by TOF correlation in the MWPCs. TOF spectra from neutron detectors were gated with fission fragments and n- γ discrimination was applied. In order to avoid angular uncertainty caused by the finite size of fission detectors, we considered slices of six rectangles each of size 38 mm \times 42 mm. The neutron TOF data were converted into energy histograms with bin size of 0.25 MeV.

Neutron multiplicity values were extracted using moving source fit prescribed by Watt formula [3]. A fit to the full set of experimental spectra $d^2M/dE_n d\Omega_n$ was made in terms of the Watt expression, minimizing chi-square by considering both multiplicities and temperatures as free parameters. The extracted values of v_{pre} and v_{post} are 4.4 and 0.8, respectively. One of the 270 decomposed spectra with contributions from each source is shown in Fig. 5.1.12.

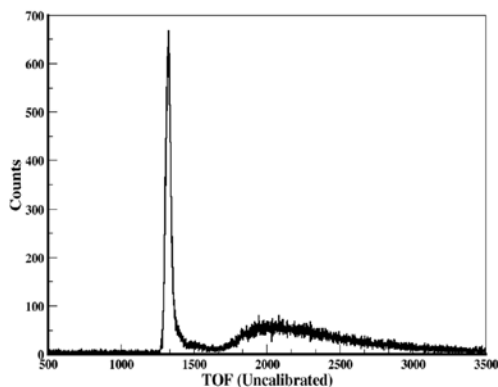


Fig. 5.1.11 TOF spectrum from one of the neutron detectors.

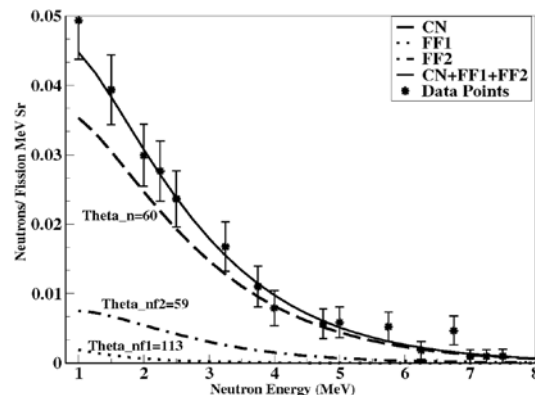


Fig. 5.1.12 Neutron energy spectra with contributions from three moving sources.

REFERENCES

- [1] D. J. Hinde et al., Phys. Rev. C 60, 054602 (1999).
- [2] P. Sugathan et al., Pramana- J. Phys.83, 807 (2014).
- [3] E. Holubet et al., Phys. Rev. C 28, 252 (1983).

5.1.7 Lifetime measurements in ^{188}Pt

Aman Rohilla¹, C. K. Gupta¹, R. P. Singh², S. Muralithar², Siddarth Roy³, Ashok Kumar⁴, I. M. Govil⁴, H. P. Sharma⁵, S. Chakarborty⁵, S. S. Tiwari⁵ and S.K. Chamoli¹

¹Department of Physics and Astrophysics, University of Delhi, Delhi 110007, India

²Inter University Accelerator Centre, ArunAsaf Ali Marg, New Delhi 110067, India

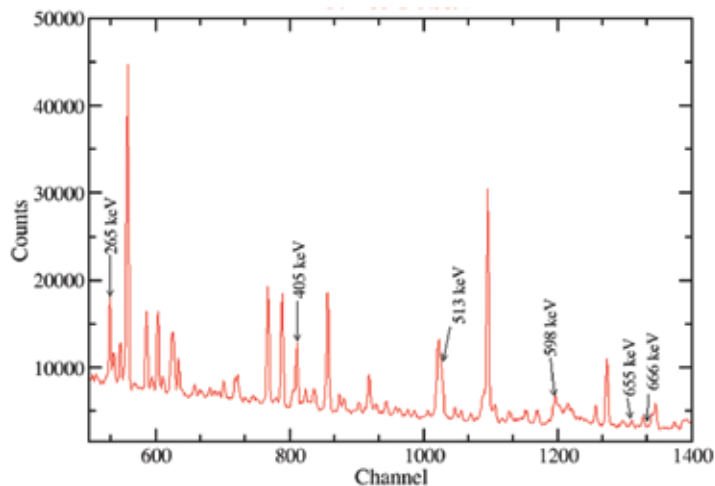
³Department of Physics, VisvaBharati, Santiniketan 731204, India

⁴Department of Physics, Panjab University, Chandigarh 160014, India

⁵Department of Physics, Banaras Hindu University, Varanasi 221005, India

The neutron deficient platinum isotopes lying in the transitional region are well known for exhibiting the shape co-existence phenomenon which can be related to the different deformations [1]. In odd A , $^{188-192}\text{Pt}$ nuclei the ground state is predicted to be of oblate shape which is indicated by the TRS calculations [2]. In the lifetime calculations done for $^{182-186}\text{Pt}$ [3, 4], the deformation obtained clearly demonstrate this fact. The deformation measurements are highly needed to test the predictions of oblate to prolate shape transition in Pt ($A \geq 188$) nuclei.

High spin states in ^{188}Pt were populated using the fusion reaction ^{174}Yb (^{18}O , $4n$). Beam energy of 84MeV was delivered by the 15UD Pelletron of IUAC. ^{174}Yb target of thickness $\sim 700\mu\text{g}/\text{cm}^2$ deposited on ^{181}Ta of thickness $\sim 3\text{mg}/\text{cm}^2$ was used and ^{197}Au of thickness $\sim 8\text{mg}/\text{cm}^2$ as stopper was used [5]. For experimental measurements GDA setup equipped with 6 Compton-suppressed HPGe detectors, 14 element BGO multiplicity filter and RDM plunger device were used. Four of the detectors were mounted in GDA backward ring at an angle of 144° and the remaining 2 were mounted in the forward ring at 50° . Data acquisition was done using the online data sorting program CANDLE. For the analysis purpose, data obtained in the detectors at same angle, after calibration and gain matching, are added together. The γ -peaks for ^{188}Pt yrast band are shown in Fig. 5.1.13. The detailed analysis is in progress[6].

Fig.5.1.13 Raw spectrum for ^{188}Pt .

REFERENCES

- [1] M.P. Robinson *et al.*, Phys. Lett. B **530**, 74 (2002).
- [2] T. Nikšić, D. Vretenar and P. Ring, Prog. Part. Nucl. Phys. **66**, 519 (2011).
- [3] J.C. Walpeet al. Phys. Rev. C **85**, 057302 (2012).
- [4] U. Garg *et al.* Phys. Lett. B **180**, 319 (1986).
- [5] C. K. Gupta, T. Rajbongshi, Aman Rohilla *et al.*, Proc. DAE Symp. Nucl. Phys. **59**, G71 (2014).
- [6] Aman Rohilla, C.K. Gupta *et al.*, Proc. DAE Symp. Nucl. Phys. **59**, A114 (2014).

5.1.8 Low energy incomplete fusion results with MARC model

Rakesh Kumar¹, Vijay R. Sharma², Mohd. Shuaib² and R. K. Bhowmik¹

¹Inter University Accelerator Centre, ArunaAsaf Ali Marg, New Delhi 110067, India

²Accelerator Laboratory, Department of Physics, Aligarh Muslim University, Aligarh 202002, India

Recently, much attention has been paid to the study of low energy heavy ion (HI) nuclear interactions to understand the reaction mechanisms involved. The observed fusion or fusion-like phenomena at the low energy nuclear reaction mechanisms such as complete fusion (CF \rightarrow where an excited composite object forms after intimate contact and transient amalgamation of projectile and target nucleus), and incomplete fusion (ICF \rightarrow where only a part of projectile fuses with target nucleus), have been extensively studied in the case of heavy targets region. The reaction mechanism of CF is well understood from both experimental and theoretical physics points of view. In spite of the availability of plenty of experimental data and various ICF models [1-2], a complete and satisfactory description of the CF and ICF simultaneous processes has yet to emerge. Even the Morgenstern *et al.* [3] study of the mass-asymmetry dependence of ICF prescription is unable to successfully explain the ICF data at relatively low energies of $\approx 3-7$ MeV/nucleon. As such, the study of HI reaction dynamics is still an active area of investigation at low projectile energies. Despite the absence of satisfactory theoretical models, investigated experimental data of reaction cross sections may help in elucidating the modeling of ICF processes.

In view of the above, recently a Multi-step pArTial Reaction Cross-section (MARC) code has been developed [4], which is able to reproduce relative yields of CF and ICF. The code first reproduces the cross-section for l-distribution. To incorporate deformation effects, the diffuseness parameter Δ is taken as an adjustable external parameter. More details on the code can be found elsewhere [4]. In the present work, testing of the code MARC for the $^{12}\text{C}+^{169}\text{Tm}$ [5], $^{13}\text{C}+^{169}\text{Tm}$ [6], $^{12}\text{C}+^{181}\text{Ta}$ [7], $^{16}\text{O}+^{169}\text{Tm}$ [8], and $^{16}\text{O}+^{181}\text{Ta}$ [7] systems have been done. The details of the experiments are given elsewhere [5-8]. The experimental ICF cross-section $\Sigma \sigma_{ICF}^{EXP}$ has been compared with the total partial cross section $\Sigma \sigma_{ICF}^{MARC}$ value which has been calculated using code MARC for different scaling parameters as a function of normalized angular momentum $(l_{max}/l_{crit})^2$

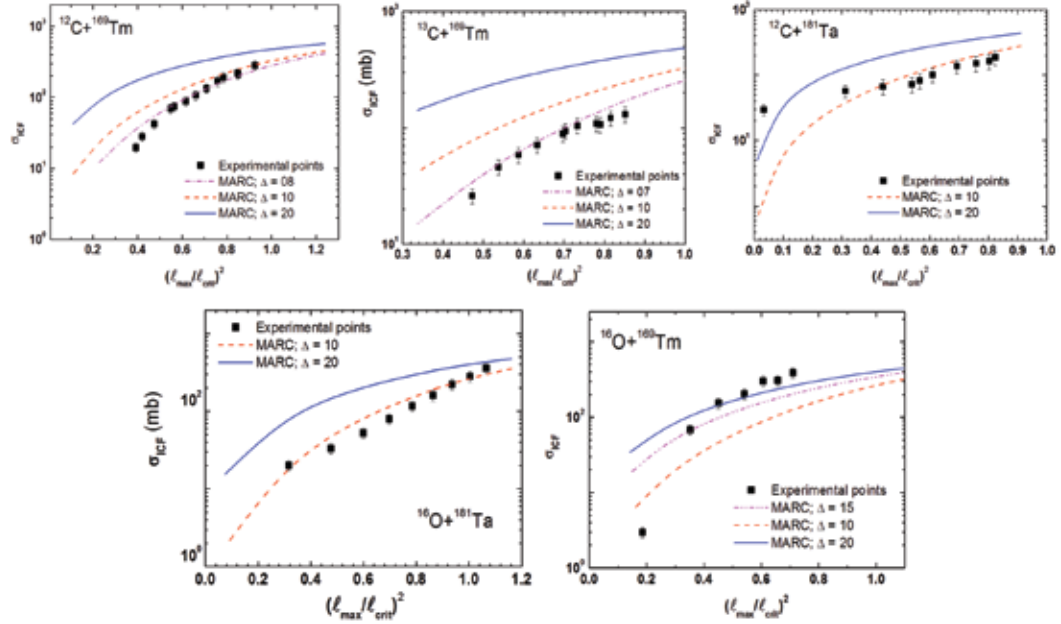


Fig.5.1.14(a)-(e). Total partial cross section $\Sigma \sigma_{ICF}^{MARC}$ using MARC code for different scaling parameters Δ (see text) as a function of normalized angular momentum.

As can be seen from the figure, the values of σ_{ICF} shows fair agreement with those predicted by MARC. Further, results presented in Fig. 5.1.14 (a-e) reveal a significant ICF contribution below l_{crit} which support our recent findings of ICF for system $^{13}\text{C}+^{169}\text{Tm}$ [6]. Hence, calculations with a semi-empirical code MARC for the presently studied systems has been found to work satisfactorily.

REFERENCES

- [1] J. Wilczynski et al., Phys. Rev. Lett. **45**, 606(1980); Nucl. Phys. A **373**, 109 (1982).
- [2] A. Diaz-Torres et al., Phys. Rev. Lett. **98**, 152701 (2007).
- [3] H.M. Morgenstern et al., Phys. Rev. Lett. **52**, 1104 (1984).
- [4] R. Kumar, Vijay R. Sharma et al., Act.Phys. Pol. B **46**, 1001 (2015).
- [5] P. P. Singh et al., J. Phys. Conf. Ser. **282**, 012019 (2011).
- [6] Vijay R. Sharma et al., Phys. Rev. C **89**, 024608 (2014).
- [7] Ettore Gadioli, Act.Phys. Pol. **B30**, 1493 (1999).
- [8] P. P. Singh et al., Phys. Rev. C. **77**, 014607 (2008).

5.1.9 Evaporation residue measurements in the $^{16,18}\text{O}+^{181}\text{Ta}$ reactions

A. M. Vinodkumar¹, P. Jisha¹, B. R. S. Babu², R. U. Amarnadh³, K. M. Varier³, M. Shareef⁴, P. V. Laveen⁴, A. Shamlath⁴, E. Prasad⁴, Tathagata Banerjee⁵, Ish Mukul⁵, J. Gehlot⁵, S. Nath⁵, A. Jhingan⁵, N. Saneesh⁵ and N. Madhavan⁵

¹Department of Physics, University of Calicut, Calicut 673635, India

²Department of Physics, Sultan Quaboos University, Muscat, Oman

³Department of Physics, University College, Thiruvanthapuram 695024, India

⁴Department of Physics, School of Mathematical and Physical Sciences, Central University of Kerala, Kasaragod 671328, India

⁵Inter University Accelerator Centre, ArunaAsaf Ali Marg, New Delhi 110067, India

The knowledge of evaporation residue (ER) cross sections at energies close to the Coulomb barrier is interesting from different aspects. Recently measured $^{18}\text{O}+^{197}\text{Au}$ forming ^{215}Fr compound nucleus [1] highlighted the importance of measuring the fusion evaporation and capture reaction cross sections in the ~ 200 mass region. The evaporation residue cross sections measured for reactions forming radium (Ra) compound nuclei is found to be significantly reduced even in very asymmetric combinations [2-4]. In the case of $^{18}\text{O}+^{197}\text{Au}$ (fissile compound nucleus ^{215}Fr), the ER cross sections at energies well above the Coulomb barrier are weakly sensitive to the form of nuclear potential and are mainly determined by standard statistical model (SSM) parameters describing compound nucleus (CN) de-excitation. The important parameters are the level density parameters in fission and evaporation channels, the scaling factor (k_f) at the rotating liquid drop (LD) fission barriers $B_f(L)$ and ground state shell corrections δW . Well above the Coulomb barrier energies, the calculations depend essentially only on k_f , which reduces the fission barrier $B_f(L)$.

For $^{18}\text{O}+^{197}\text{Au}$, a scaling factor $k_f=0.85$ was used for reproducing experimental results. Also, for $^9\text{Be} + ^{209}\text{Bi}$ forming ^{218}Fr compound nucleus, $k_f=0.85$ was used for calculations. However, for $^{16}\text{O}+^{197}\text{Au}$, $k_f=0.82$ is required for reproducing the experimental results. Also, as seen from [5], one can see that different scaling values are required for reproducing the evaporation residue cross sections and capture cross sections in the different reactions forming compound nucleus in the $A \sim 200$ region.

Sagaidak et al. [5] analysed ER and fission excitation functions obtained in the very asymmetric $^{12}\text{C}+^{204,206,208}\text{Pb}$ reactions leading to $^{216,218,220}\text{Ra}$ and more symmetric $^{48}\text{Ca} + ^{168,170}\text{Er}$ reactions leading to $^{216,218}\text{Ra}$ using SSM. The role of quasi-fission (QF) in C + Pb reaction appears to be negligible and they applied barrier penetration model (BPM) coupled with SSM. These reactions (C + Pb) cover the region of neutron numbers $122 < N < 130$, the effect of $N=126$ neutron shell closure was studied and then applied to $^{48}\text{Ca} + ^{168,170}\text{Er}$.

To study the mechanism of limitations observed in fusion [2] near the Businaro-Gallone point [6] for systems with similar entrance-channel mass asymmetry, we have measured evaporation residue cross sections for $^{18,16}\text{O}+^{181}\text{Ta}$ systems at near and above barrier energies using HIRA spectrometer. The ERs formed in the $^{18,16}\text{O}+^{181}\text{Ta}$ reactions were detected at the focal plane of HIRA using standard focal plane detector of HIRA. The measurements were done for beam energies from

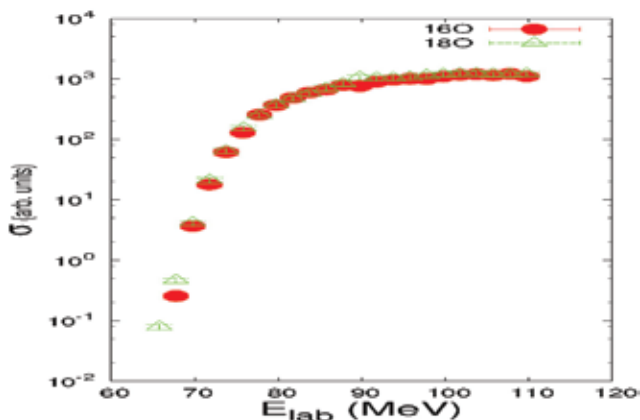


Fig. 5.1.15 Comparison of fusion ER excitation functions of $^{16}\text{O}+^{181}\text{Ta}$ and $^{18}\text{O}+^{181}\text{Ta}$ reactions.

110 MeV to 66 MeV with a step of 2 MeV. The total ER cross sections were measured using E-TOF generated between focal plane detector and RF. Preliminary results are shown in Fig. 5.1.15. In comparison with $^{16}\text{O}+^{181}\text{Ta}$ reaction, $^{18}\text{O}+^{181}\text{Ta}$ does not show any additional enhancement. A detailed analysis using statistical model is in progress.

REFERENCES

- [1] L. Corradi *et al.*, Phys. Rev. C **71**, 014609 (2005).
- [2] A. C. Berriman *et al.*, Nature (London) **413**, 144 (2001); D. J. Hinde *et al.*, J. Nucl. Radiochem. Sci. **3**, 31 (2002).
- [3] R. N. Sagaidak *et al.*, Phys. Rev. C **68**, 014603 (2003).
- [4] D. J. Hinde, M. Dasgupta and A. Mukherjee, Phys. Rev. Lett. **89**, 282701 (2002).
- [5] R. N. Sagaidak *et al.*, JINR Preprint E7-2003-149, Dubna(2003).
- [6] U. L. Businaro and S. Gallone, Nuovo Cimento **1**, 1277 (1955).

5.1.10 Measurement of evaporation residue excitation functions and barrier distributions for the reactions $^{16}\text{O}+^{174,176}\text{Yb}$

Tapan Rajbongshi¹, K. Kalita¹, S. Nath², N. Madhavan², J. Gehlot², A. Jhingan², T. Varughese², I. Mukul², Tathagata Banerjee², R. Dubey², P. Sharma³, N. Kumar⁴, A. Shamlath⁵, P. V. Laveen⁵, M. Shareef⁵ and P. Jisha⁶

¹Department of Physics, Gauhati University, Guwahati 781014, India

²Nuclear Physics Group, Inter University Accelerator Centre, Aruna Asaf Ali Marg, New Delhi 110067, India

³Department of Physics, Panjab University, Chandigarh 160014, India

⁴Department of Physics and Astrophysics, University of Delhi 110007, India

⁵Department of Physics, School of Mathematical and Physical Sciences, Central University of Kerala, Kasaragod 671314, India

⁶Department of Physics, University of Calicut, Calicut 673635, India

The study of fusion-fission reactions around the Coulomb barrier energies have been a topic of intense research during the past few decades [1-2]. Fusion-fission reactions at near barrier energies are dramatically influenced by the internal structure and entrance channel parameters of the interacting nuclei. Entrance channel properties such as mass asymmetry and deformation of the colliding partners are governed to affect the probability of compound nucleus (CN) formation. The deformation of one or both the partners in a heavy-ion reaction is expected to influence the effect on the fusion cross section at near barrier energies [3-6] to differ drastically. In order to study the role of negative hexadecapole deformation effect on sub-barrier fusion reaction we have performed experiments with the $^{16}\text{O}+^{174,176}\text{Yb}$ systems.

The experiments have been performed in the HIRA [7] facility using Pelletron beams of the Inter University Accelerator Centre (IUAC), New Delhi. A pulsed beam of ^{16}O with a pulse separation of 4 μs was used in the experiment to bombard isotopically enriched ^{174}Yb and ^{176}Yb targets of thickness 125 $\mu\text{g}/\text{cm}^2$ and 170 $\mu\text{g}/\text{cm}^2$ respectively, on carbon backing of thickness about 25 $\mu\text{g}/\text{cm}^2$. ER excitation function measurements were performed at laboratory beam energies of 64.6 - 79.6 MeV at 1 MeV steps and of 81.6 - 103.6 MeV at 2 MeV steps for the systems $^{16}\text{O}+^{174}\text{Yb}$ and $^{16}\text{O}+^{176}\text{Yb}$, respectively. Two silicon surface barrier detectors were placed inside the target chamber at angles of $\pm 15.5^\circ$ with respect to beam direction to measure Rutherford-scattered beam-like particles and to get absolute normalization of ER cross sections. A 30 $\mu\text{g}/\text{cm}^2$ carbon foil was placed downstream of target to reset the charge state of the ERs. At the focal plane (FP) of

the HIRA, a two-dimensional position-sensitive MWPC detector with an active area of 150 mm \times 50 mm was used to detect ERs. The transmission efficiency of HIRA was calculated by using the semi-microscopic Monte Carlo code, TERS [8] for each xn-evaporation channel at all E_{lab} . The average ER transmission efficiency for all the ERs through the HIRA was obtained by taking the weighted average of the efficiency for different evaporation channels at each energy (E_{lab}). The relative abundance of different exit channels were estimated by using the statistical model code PACE3 [9]. The preliminary ER cross-sections for both the systems are shown in Fig. 5.1.16 below. These are preliminary results and further analysis is in progress. In the measurement of the fusion cross section, the evaporation residue cross section was taken to be equal to the total fusion cross section since the fission contribution in this energy region is negligible. The coupled-channel (CC) calculations were performed with a modified version of the code CCFULL [10]. The aim of the present work is to extract fusion barrier distributions and to analyse the same using CCFULL.

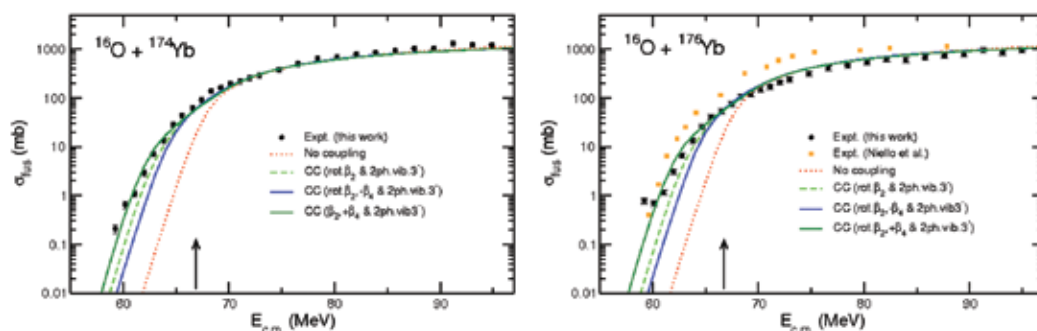


Fig 5.1.16 Experimental fusion excitation function for $^{16}\text{O} + ^{174,176}\text{Yb}$ systems compared with the results of coupled-channels calculation.

REFERENCES

- [1] M. Dasgupta, D. J. Hinde, N. Rowley, and A. M. Stefanini, *Annu. Rev. Nucl. Part. Sci.* **48**, 401 (1998).
- [2] A. B. Balantekin and N. Takigawa, *Rev. Mod. Phys.* **70**, 77 (1988).
- [3] J. O. Fernandez Niello *et al.*, *Phys. Rev. C* **43**, 2303 (1991).
- [4] M. J. Rhoades Brown and V. E. Oberacker, *Phys. Rev. Lett.* **50**, 1435 (1983).
- [5] J. O. Fernandez Niello and C. H. Dasso, *Phys. Rev. C* **39**, 2069 (1989).
- [6] T. Rajbongshi and K. Kalita, *Cent. Eur. J. Phys.* **12**, 433 (2014).
- [7] A. K. Sinha *et al.*, *Nucl. Instrum. Meth. A* **339**, 543 (1994).
- [8] S. Nath, *Comput. Phys. Commun.* **179**, 492 (2008); **180**, 2392 (2009).
- [9] A. Gavron, *Phys. Rev. C* **21**, 230 (1980).
- [10] K. Hagino, N. Rowley, and A. T. Kruppa, *Comput. Phys. Commun.* **123**, 143 (1999).

5.1.11 Fusion cross-section measurements for $^{28}\text{Si} + ^{96}\text{Zr}$ system

Khushboo¹, S. Mandal¹, S. Nath², N. Madhavan², J. Gehlot², A. Jhingan², T. Varughese², B. R. Behera³, S. Verma¹, P. Verma⁴, Davinder Siwal², R. Garg¹, Ish Mukul², M. Saxena¹, N. Kumar¹, A. Toshniwal¹, G. Kaur³, K. Rojeeta¹, A. Banerjee¹, Tathagata Banerjee² and Neelam¹

¹Department of Physics and Astrophysics, University of Delhi, Delhi 110007, India

²Inter University Accelerator Centre, Aruna Asaf Ali Marg, New Delhi 110067, India

³Department of Physics, Panjab University, Chandigarh 160014, India

⁴Department of Physics, Kalindi College, University of Delhi, New Delhi 110008, India

The study of heavy ion fusion dynamics around the Coulomb barrier plays an important role to examine the inelastic excitations and nucleon transfer channels effect on fusion cross-sections.

The enhancement observed in fusion cross-sections in sub-barrier region was well understood by coupling of transfer channels along with inelastic excitations [1, 2]. As one goes far below the Coulomb barrier, fusion cross-sections start deviating from the theoretical cross-sections. This deviation is termed as fusion hindrance [3, 4]. Therefore to investigate the fusion enhancement and hindrance phenomenon, an experiment was performed to measure the fusion cross-sections for $^{28}\text{Si}+^{96}\text{Zr}$ system. ^{96}Zr is a nearly spherical nucleus and the chosen system favours the transfer coupling due to its positive Q-value upto 6 neutrons transfer. Therefore, the effect of multi-neutron transfer on fusion cross-sections can also be studied.

The experiment was performed using the Heavy Ion Reaction Analyzer (HIRA) at IUAC [5]. HIRA was kept at 00 with respect to the beam direction with 10 mSr entrance aperture. ^{28}Si pulsed beam was used to bombard the enriched ^{96}Zr target ($\sim 230 \mu\text{g}/\text{cm}^2$ on $20 \mu\text{g}/\text{cm}^2$ carbon backing) which was prepared by electron beam evaporation method at the Target Laboratory of IUAC. Fusion cross-sections were measured from 120 MeV to 78 MeV (25% above the one-dimensional barrier to 18% below the barrier) in steps of 2 - 4 MeV. A Multi-Wire Proportional Counter (MWPC) with dimensions $152.4 \times 50.8 \text{ mm}^2$ was placed at the focal plane of HIRA for the detection of the Evaporation Residues (ERs). Two silicon surface barrier detectors (SSBD) were placed inside the target chamber at an angle of $\pm 25^\circ$ with respect to beam direction for normalization of cross-sections. A time of flight (TOF) was set up between anode of MWPC and RF signal to separate the beam-like particles from ERs. A two dimensional spectrum between energy loss in MWPC and TOF is shown in Fig. 5.1.17. The variation of raw fusion cross-sections with beam energy is shown in Fig. 5.1.18. Further analysis is in progress.

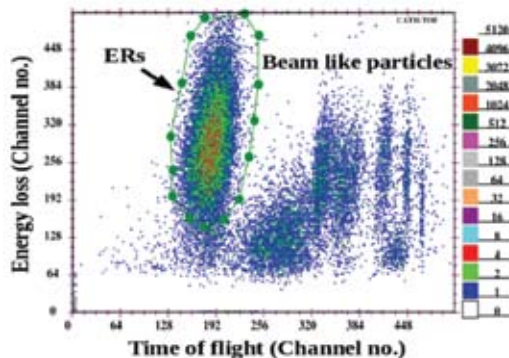


Fig. 5.1.17 Two-dimensional spectrum of Energy loss vs of TOF for $^{28}\text{Si}+^{96}\text{Zr}$ at 96 MeV projectile energy.

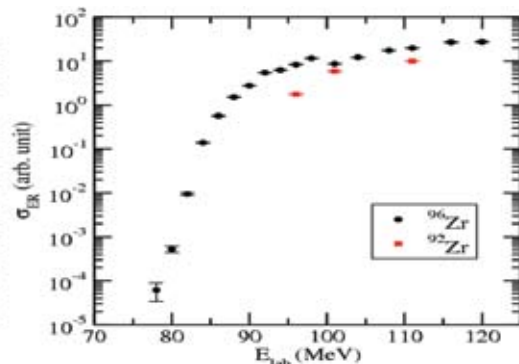


Fig. 5.1.18 Fusion cross-section as a function projectile energy for $^{28}\text{Si}+^{92,96}\text{Zr}$ systems.

REFERENCES

- [1] S. Kalkal *et al.*, Phys. Rev. C **81**, 044610 (2010).
- [2] H. Q. Zhang *et al.*, Phys. Rev. C **82**, 054609 (2010).
- [3] C. L. Jiang *et al.*, Phys. Lett. B **640**, 18 (2006).
- [4] M. Dasgupta *et al.*, Phys. Rev. Lett. **99**, 192701 (2007).
- [5] A. K. Sinha *et al.*, Nucl. Inst. Meth. A **339**, 543 (1994).

5.1.12 Systematic study of P_{CN} in pre-actinides

Tathagata Banerjee¹, S. Nath¹, A. Jhingan¹, Gurpreet Kaur², R. Dubey¹, Abhisek Yadav¹, A. Shamlath³, Shareef M.³, P. V. Laveen³, J. Gehlot¹, Saneesh N.¹ and P. Sugathan¹

¹Nuclear Physics Group, Inter University Accelerator Centre, Aruna Asaf Ali Marg, Post Box 10502, New Delhi 110067, India

²Department of Physics, Panjab University, Chandigarh 160014, India

³Department of Physics, School of Mathematical and Physical Sciences, Central University of Kerala, Kasaragod 671328, India

The cross section for producing a heavy evaporation residue, σ_{ER} , in a fusion reaction can be factorized as

$$\sigma_{ER} = \sum_{J=0}^{J_{max}} \sigma_{capture}(E_{c.m.}, J) \times P_{CN}(E_{c.m.}, J) \times P_{sur}(E_{c.m.}, J) \quad 5.1.1$$

where, $\sigma_{capture}(E_{c.m.}, J)$ is the capture cross section at center of mass energy $E_{c.m.}$ and spin J . P_{CN} is the probability that the projectile-target system will evolve inside the fission saddle point to form the compound nucleus (CN). P_{sur} is the probability that the CN will de-excite by emission of γ -rays and evaporation of light particles rather than fission (CNF).

The fusion probability P_{CN} is the *least known quantity* in equation 5.1.1. The dependence of P_{CN} on excitation energy [1,2] and the reaction entrance channel is not well established [2,3]. A large number of qualitative studies exist in literature showing presence of non-compound-nucleus-fission (NCNF) in heavy and super-heavy region. However, only a handful of studies have been attempted to experimentally *measure* P_{CN} [4, 5, 6, 7], which is a crucial quantity to understand fusion-fission dynamics in heavy region and formation of super-heavy elements (SHE). In our recent work [8], we have shown angular-momentum-averaged fusion probability, (P_{CN}) to vary with entrance channel mass asymmetry ($\eta = |A_p - A_t| / (A_p + A_t)$) or charge product ($Z_p Z_t$), as well as with fissility of the CN (χ_{CN}). Approximate boundaries have also been obtained from where P_{CN} starts deviating from unity. Unambiguous consensus between experimentally extracted PCN values using different probes is yet to be achieved.

We focused on a systematic and quantitative investigation of P_{CN} for pre-actinides ($Z = 83-88$) by measuring FF angular distributions above the Coulomb barrier at (approximately) matching η , $Z_p Z_t$, deformation (β_2) of the reactants, excitation energy (E^*) and fissility. The experiment was performed in the General Purpose Scattering Chamber (GPSC) of IUAC with ^{28}Si beam. ^{169}Tm , ^{176}Yb , ^{175}Lu , ^{180}Hf , ^{181}Ta and ^{182}W targets were used to populate CN covering the pre-actinide region. All these targets were fabricated at the target laboratory of IUAC. Thicknesses of these targets were $\sim 150 \mu\text{g}/\text{cm}^2$.

Target ladder was kept at 45° with respect to the beam direction. In all, nine hybrid telescope detectors were used. One hybrid detector module is a combination of a ΔE detector (gas) and a E detector (Si) [9]. Out of those, six were mounted on the upper arm covering the backward angles ($70^\circ-170^\circ$) while the other three were kept at the forward angles ($41^\circ-65^\circ$) on the lower arm. Gas pressure was kept constant at 75 mbar. The trigger for the data acquisition system was generated using the OR of the timing signals from all E and ΔE detectors. Measurements were carried out near or above the Coulomb barrier. Two monitor detectors were kept at $\pm 10^\circ$ for monitoring the beam and normalization.

Most of the fission fragments were stopped in ΔE detector due to higher energy loss. All high energy beam-like particles passed through the ΔE detector and were stopped in the E detector. Fission fragments were well separated from quasi-elastic events.

We shall further employ Back's formalism [4] to decompose fission fragment angular distribution into two components - one due to CNF and another due to NCNF and hence estimate P_{CN} . The fission fragment angular distributions for the reaction $^{28}\text{Si}+^{175}\text{Lu}$ are shown in Fig 5.1.19. Data are fitted with Legendre polynomials.

We thank members of the Pelletron and the target laboratories of IUAC for providing beam of excellent quality and help in fabrication of isotopic targets, respectively.

REFERENCES

- [1] V. I. Zagrebaev and W. Greiner, Phys. Rev. C 78, 034610 (2008).
- [2] R. S. Naik et al, Phys. Rev. C 76, 054604 (2007).
- [3] R. Yanez et al, Phys. Rev. C 88, 014606 (2013).
- [4] B. B. Back, Phys. Rev. C 31, 2104 (1985).
- [5] R. K. Choudhury and R. G. Thomas, J. Phys. Conf. Series 282, 012004 (2011).
- [6] A. C. Berriman et al, Nature (London)413, 144 (2001).
- [7] R. Yanez et al., Phys. Rev. C 85, 044620 (2012).
- [8] Tathagata Banerjee, S. Nathand Santanu Pal, Phys. Rev. C 91, 034619 (2015).
- [9] A. Jhingan et al., Proc. DAE Symp. Nucl.Phys. 59, 830 (2014).

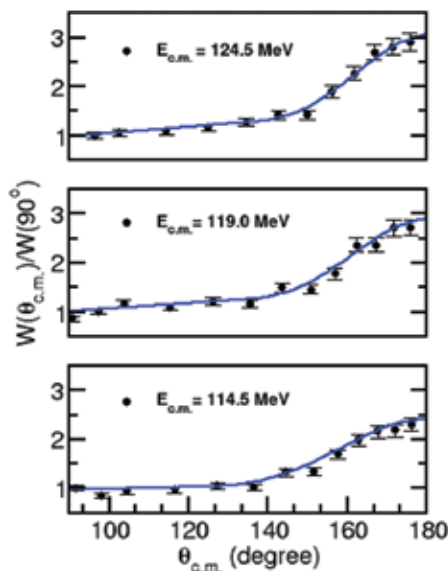


Fig 5.1.19 Fission fragment angular distributions for the reaction $^{28}\text{Si}+^{175}\text{Lu}$.

5.1.13 DCO ratio analysis of high spin states in ^{67}Ga

S. Rai¹, B. Mukherjee¹, S. Muralithar², R.P. Singh², R. Kumar², K. Rani², R.K. Bhowmik²

¹Dept. of Physics, Siksha-Bhavana, VisvaBharati, Santiniketan 731235, India

²Inter University Accelerator Center, Aruna Asaf Ali Marg, New Delhi 110067, India

With three protons above the magic $Z=28$ shell closure, Ga isotopes are ideal for studying the interplay of the single particle and collective behavior. For odd-A Ga isotopes, the valence particles occupy the negative parity $2p_{1/2}$, $2p_{3/2}$ and $1f_{5/2}$ orbitals outside the $N=Z=28$ Ni core. As a result of which the $^{63,65,67}\text{Ga}$ have $I^\pi = 3/2^-$ as ground state and $I^\pi = 5/2^-$ as the first excited state[3-4]. On the other hand, for higher excited states, occupation of positive parity $g_{9/2}$ intruder orbital plays an important role. In these nuclei, the $9/2^+$ state, whose configuration may be understood as due to the promotion of the unpaired proton into $g_{9/2}$ orbital, is the lowest positive parity state and lies at about 2 MeV excitation energy. Alignment of neutron pair may be expected at higher rotational frequency. In heavier $^{71,73,75}\text{Ga}$, addition of $g_{9/2}$ neutrons is expected to bring in more deformation and pronounced rotational band structure built on single proton level[5].

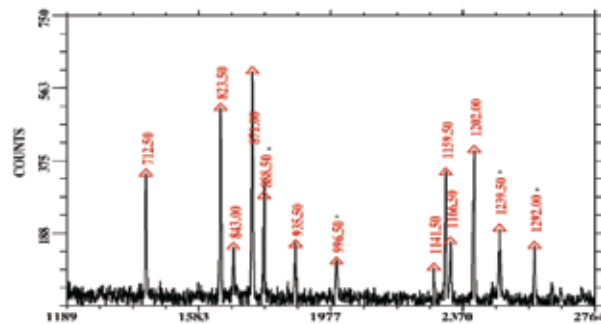


Fig. 5.1.20 Total projected spectrum gated by 958 keV γ -line of ^{67}Ga .

High spin state is revisited, particularly the rotational-like band structure based on $9/2^+$ state, using old data from GDA+CPDA experiment held in September, 2000. Previous spectroscopic data on high spin states of ^{67}Ga are available from $^{53}\text{Cr}(^{16}\text{O},\text{pn}\gamma)$ [1], $^{57}\text{Fe}(^{12}\text{C},\text{pn}\gamma)$ [2] and $^{12}\text{C}(^{58}\text{Ni},^3\text{p}\gamma)$ [3] reactions.

Fusion evaporation reaction $^{52}\text{Cr}(^{19}\text{F},2\text{p}2\text{n})$ was used to populate high spin states in ^{67}Ga at beam energy of 70 MeV provided by the 15UD Pelletron accelerator of IUAC, New Delhi. A 1 mg/cm^2 thin natural Cr(84% natural abundance) was evaporated onto 7 mg/cm^2 gold backing. Prompt γ -rays were detected using the Gamma Detector Array(GDA)[6] consisting of 12 Compton-suppressed germanium(HpGe) detectors in coincidence with the evaporated light charged particles for better channel selection. The HPGe detectors in GDA were arranged in three rings, four each at 53° , 99° , and 153° . The 4π charged particle detector array(CPDA)[7] comprised of 14 $\Delta\text{E-E}$ phoswich plastic scintillators (BC400 and BC444). More details on the experimental setup can be found in [7, 10]. Offline analysis of the data was performed using INGASORT [8] and Radware [9] suites of programs. The level scheme obtained in this work is consistent with the previous work of Zobel *et.al.*[2] and Danko *et.al.*[3]. Due to the weak population of the negative parity states, we were unable to observe some of the transitions as quoted in [3]. The rotational-like structure based on $9/2^+$ level was strongly populated in the fusion evaporation reaction. We have performed DCO analysis to confirm the quadrupole nature of the gamma rays belonging to the band. A γ - γ coincidence matrix was constructed with events detected at $153^\circ(\theta_1)$ versus those at $99^\circ(\theta_2)$. By gating a transition of known multi-polarity, DCO ratio was obtained,

$$R_{\text{DCO}} = I\gamma_1(\theta_1), \text{ gated by } \gamma_2(\theta_2) / I\gamma_1(\theta_2), \text{ gated by } \gamma_2(\theta_1) \quad (1)$$

Gating with a known quadrupole transition, the value of RDCO is expected to be approximately unity for quadrupole transition. A stretched dipole is expected to have RDCO between 0.4 and 0.6, while a value between 0.6 and 0.8 implies a mixed transition. For pure non-stretched dipole ($L = 1, \Delta J = 0$) transitions, RDCO value is also expected to be close to unity.

In our case, DCO ratio was obtained by putting gate on known quadrupole transition, 958 keV. The values obtained for the transition belonging to the band confirms the quadrupole nature of the transitions. The plot of DCO ratio for different transitions is shown in Fig. 5.1.21. Also the multipolarity of 935 keV transition originating from 5225 keV has been confirmed as $\Delta I=1$ transition, which was previously assigned as $\Delta I=2$ transition by Zobel *et.al.* [2] prior to that of [1].

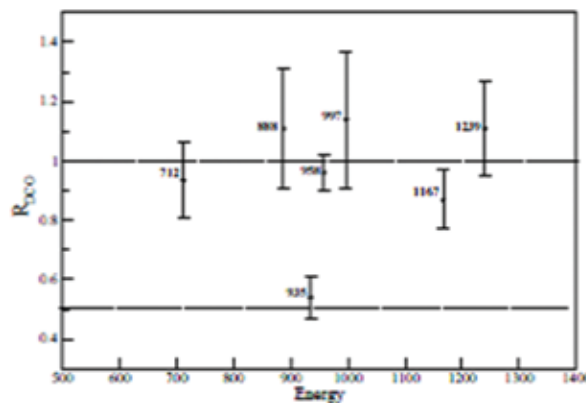


Fig. 5.1.21 DCO ratio of transitions belonging to ^{67}Ga gated by 958 keV γ -line.

We have revisited the level structure of the ^{67}Ga and studied the nature of its band structure using DCO analysis. Level scheme obtained is consistent with the previous works [2, 3]. It is suggested that polarization and lifetime measurements of the band in ^{67}Ga and its other isotopes are essential to understand the evolution of the collectivity of the $\pi g_{9/2}$ band. Further analysis of the data and study of the band structure using cranked shell model is in progress.

We would like to gratefully acknowledge Pelletron and target laboratory staff, IUAC for their support in this work. S. Rai acknowledges financial assistance received through IUAC UFR-project(UFR-49318).

REFERENCES

- [1] A.M. Al Naseret al. J. Phys. G 10, 1611(1978).
- [2] V. Zobelet al. Nucl.Phys. A316, 165(1979).
- [3] I. Dankoet al. Phys. Rev. C 59, 1956(1999).
- [4] M. Weiszfloget al. Eur. Phys. J.A11,25(2001).
- [5] I. Stefanscuet al. Phys. Rev. C 79, 064302(1999).
- [6] S. C. Pancholi and R. K. Bhowmik, Indian J. Pure Appl. Phys. 27,660 (1989).
- [7] S. Muralithar et al. Nucl.Instrum.Meth.A729, 849(2013).
- [8] R.K. Bhowmik et al., Proc. DAE Symp. Nucl.Phys.44B, 422 (2001).
- [9] D.C. Radford, Nucl. Instrum.Meth.A361,290(1995).
- [10] B. Mukherjee et al. Phys. Rev C 64, 024304(2001).

5.1.14 g-factor and quadrupole moment of $11/2^-$ and $23/2^+$ isomeric states in ^{135}La

N. Bansal¹, J. Kaur², A.K. Bhati², K. Kapoor² and R. Kumar³

¹Guru Nanak Girls College, Ludhiana 141002, India

²Centre of Advanced Study in Physics, Panjab University, Chandigarh 160014, India

³Inter University Accelerator Centre, ArunaAsaf Ali Marg, New Delhi 110067, India

The transitional nuclei in the $A \sim 130$ mass region with a few valence nucleons near shell closure offer to study a variety of shapes and structure, due to the interplay of various multi-quasiparticle excitations. The experimental studies based on γ -ray spectroscopy reveals the role of the unique parity orbital, $h_{11/2}$ for the various exciting phenomenon observed in this region [1]. The study of static nuclear electromagnetic moments is crucial to know the underlying particle configurations and shape of the nucleus as a test for various theoretical models. In the present investigation, the magnetic perturbation of the angular distribution pattern of the de-exciting γ -rays from, the respective isomeric states, has been exploited for the calibration of the internal magnetic field at La in iron and for determination of the g-factor of the isomeric state with spin- parity $23/2^+$ ($\tau_{1/2} = 28.4(8)\text{ns}$) in ^{135}La [2]. The Time Differential Perturbed Angular Distribution (TDPAD) technique was used for these measurements.

The isomeric states in ^{135}La were populated and aligned in the reaction $^{128}\text{Te}(^{11}\text{B}, 4n\gamma)^{135}\text{La}$ using ^{11}B pulsed beam at 60 MeV energy from the 15UD Pelletron accelerator facility at IUAC. An isotopically enriched $500 \mu\text{g}/\text{cm}^2$ ^{128}Te evaporated on $5.7 \text{ mg}/\text{cm}^2$ gold foil backed by iron foil (for g-factor) or $7 \text{ mg}/\text{cm}^2$ terbium foil (for Q-moment) was used as a target. The 99.99% pure iron foil was annealed after rolling to the desired thickness [3]. In the second part of the experiment, the $19/2^-$ isomeric state in ^{137}La was excited through the $^{130}\text{Te}(^{11}\text{B}, 4n\gamma)^{137}\text{La}$ reaction by 55 MeV ^{11}B pulsed beam with $1 \mu\text{s}$ time interval to calibrate the internal magnetic field at La in Fe. In these

experiments, the iron foil was polarized by 0.2 T external magnetic field, perpendicular to the beam-detector plane. The delayed γ -rays from the respective isomeric states were detected by two LaBr_3 detectors placed at $\pm 135^\circ$ in a horizontal plane w.r.t the beam at a distance of 20 cm from the target. The data were collected in list mode with four parameters, the energy and time signals for each LaBr_3 detector.

The spin rotation spectrum for the magnetic interaction is shown in Fig 5.1.22. The preliminary analysis has shown the magnetic hyperfine field at La in Fe, $B_{\text{in}} = 22(5)$ T. The values of g-factor so deduced is $g(23/2^+) = 0.11(2)$.

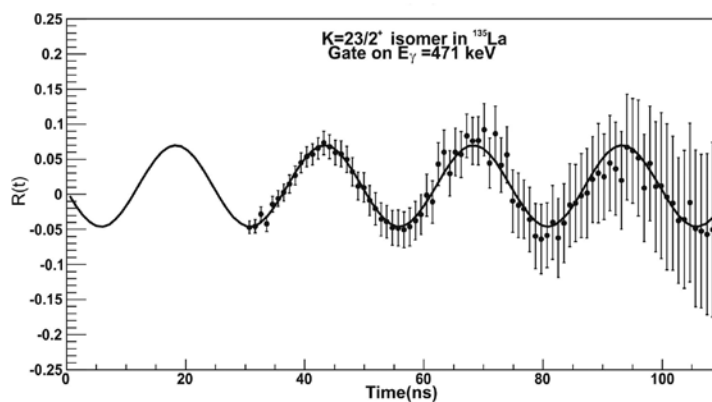


Fig. 5.1.22 Spin rotation spectra for the magnetic interaction of $23/2^+$ isomeric state in ^{135}La .

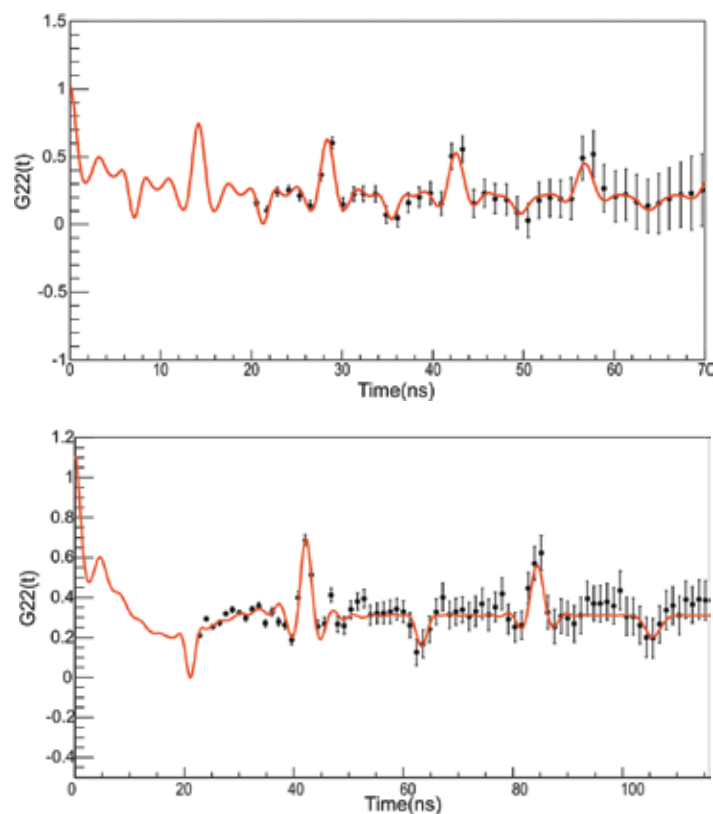


Fig. 5.1.23 Spin rotation spectra for quadrupole interaction of $11/2^-$ and $23/2^+$ isomeric states in ^{135}La .

The values of quadrupole interaction frequencies are, $\omega_{01}(11/2^-) = 443.6(6)$ mrad/s and $\omega_{01}(23/2^+) = 148.5(6)$ mrad/s. The quadrupole precession spectra are shown in Fig. 5.1.23.

REFERENCES

- [1] R.F. Casten and P. von Brentano, Phys. Lett. B **152**, 22 (1985).
- [2] R. Leguillon *et al.*, Phys. Rev. C **88**, 044309 (2013).
- [3] P. Maier-Komor, K. H. Spiedel and A. Stolarz, Nucl. Instrum. Meth. A **334**, 191 (1993).

5.1.15 Measurement of barrier distribution for the $^{28}\text{Si}+^{154}\text{Sm}$ system through quasi-elastic scattering

Gurpreet Kaur¹, B.R. Behera¹, A. Jhingan², Priya Sharma¹, Meenu Thakur¹, Ruchi Mahajan¹, R. Dubey², N. Saneesh², T. Banerjee², Khushboo³, A. Kumar¹, S. Mandal³, B.K. Nayak⁴, A. Saxena⁴ and P. Sugathan²

¹Department of Physics, Panjab University, Chandigarh 160014, India

²Inter University Accelerator Centre, Aruna Asaf Ali Marg, New Delhi 110067, India

³Department of Physics and Astrophysics, Delhi University, Delhi 110007, India

⁴Nuclear Physics Division, Bhabha Atomic Research Centre, Trombay, Mumbai 400085, India

It is well established that the interplay between nuclear structure and reaction dynamics can lead to enhancement of sub-barrier fusion cross sections, when compared with single-barrier predictions. However, the role of neutron transfer in heavy-ion fusion is still not well understood. Systems like $^{40}\text{Ca}+^{124,132}\text{Sn}$ [1], and $^{28}\text{Si} + ^{124}\text{Sn}$ [2] show effects on the enhancement, and on the related barrier distributions, due to the presence of positive Q-value neutron-transfer channels. However, fusion in systems such as $^{58,64}\text{Ni} + ^{124,132}\text{Sn}$, despite the presence of positive Q-value channels, does not show such a correlation [3]. Recently, it has been reported that coupling to positive Q-value neutron transfer channels are important if they lead to a change in the deformation of the colliding nuclei. However, most of the systems studied involved spherical nuclei where the couplings take place to surface vibrations. It is, therefore, of interest to look for possible transfer effects in the presence of a static deformation of the target and/or projectile. Moreover, the fusion barrier distribution (BD) has been shown to permit deeper insight into fusion dynamics than the cross section itself.

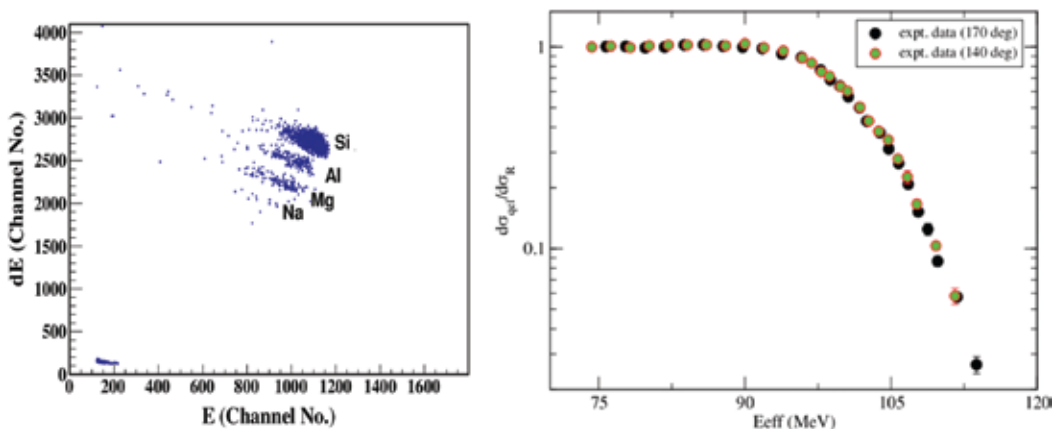


Fig.5.1.24 Online ΔE vs. E spectra obtained at angle of 170° with respect to beam direction for $E_{\text{lab}}=118$ MeV (left) and obtained quasi-elastic excitation function (right).

With the above motivation in mind, a quasi-elastic BD measurement has been carried out for the $^{28}\text{Si} + ^{154}\text{Sm}$ system, whose target possesses a large static deformation. The measurements have been performed employing HYTAR (HYbrid Telescope ARray for quasi-elastic measurements) facility, using ^{28}Si beam from 15UD Pelletron at IUAC, New Delhi. HYTAR comprises of thirteen hybrid detectors with four detectors at 170° in the ring arrangement and six detectors at angles from 140° to 40° with angular separation of 20° and other three detectors at angle of 45° , 57° and 69° with respect to beam direction. The hybrid detector is a combination of gas ionization chamber (as ΔE) and silicon detector (as E). The active length of ΔE detector is 18 mm and has been operated at 90 mbar of isobutane gas. The thickness of E detector is 300 μm which is sufficient to completely stop the particles with residual energies. The defining apertures of all the telescopes are 7 mm with angular opening of 1.5° . Online ΔE versus E energy spectra and measured quasi-elastic excitation function have been shown in Fig.5.1.24. Precise quasi-elastic cross sections have been used to extract BD for the $^{28}\text{Si} + ^{154}\text{Sm}$ system. Further analysis of the data is under progress.

REFERENCES

- [1] J.J. Kolataet al., Phys. Rev. C 85, 054603 (2012).
- [2] L.S. Danu et al., Phys. Rev. C 89, 044607 (2014).
- [3] Z. Kohleyet al., Phys. Rev. Lett. 107, 202701 (2011).

5.1.16 Study of entrance channel dynamics in fusion-fission reactions through fission fragment mass distributions

A.Chaudhuri¹, T. K. Ghosh¹, K. Banerjee¹, S. Bhattacharya¹, P. Roy¹, T. Roy¹, C. Bhattacharya¹, S. Kundu¹, J. K. Meena¹, G. Mukherjee¹, Md. A. Asgar¹, A. Dey¹, S. Manna¹, R. Pandey¹, T. K. Rana¹, V. Shrivastava¹, R. Dubey², J. Gehlot², Gurpreet Kaur³, N. Saneesh², P. Sugathan² and P. Bhattacharya⁴

¹Variable Energy Cyclotron Centre, 1/AF Bidhan Nagar, Kolkata 700064, India

²Inter University Accelerator Centre, ArunaAsaf Ali Marg, New Delhi 110067, India

³Department of Physics, Panjab University, Chandigarh 160014, India

⁴Saha Institute of Nuclear Physics, 1/AF Bidhan Nagar, Kolkata 700064, India

Fusion of two nuclei to produce heavy elements is known to be hindered by competing process of non-equilibrium fission, in which the two colliding nuclei form a composite system at the onset of the fusion process, but undergoes fission before fusion is complete. Pre-equilibrium fission [1] and quasi-fission [2] are examples of such processes which show strong entrance channel correlation. Understanding the dynamics and entrance channel dependence of the non-compound nuclear fission process may be the key to find the optimum route to form the super heavy elements (SHE).

Recent Evaporation Residue (ER) measurements [3] of $^{19}\text{F}+^{181}\text{Ta}$ and $^{16}\text{O}+^{184}\text{W}$ populating the same compound nucleus ^{200}Pb showed significant suppression of normalised ER cross-section and moments of gamma multiplicity distribution, thereby suggesting a suppression of higher values of spin for the more symmetric $^{19}\text{F}+^{181}\text{Ta}$ system at higher excitation energies. The two systems have entrance channel mass asymmetries (α) on either side of the Businaro-Gallone critical mass asymmetry (α_{BG}) for the composite nucleus ^{200}Pb . The experimental finding [3] suggested that pre-equilibrium fission [1] is the dominant channel which reduces the cross-section of the more symmetric system. However, the ER cross-section for the two systems could be very well explained in the framework of di-nuclear system (DNS) model if the fusion cross-section, which was used to

normalize the ER cross-section data, is taken to be the total capture cross-section [4]. Analysis in the framework of DNS would also suggest that quasi-fission and fast fission cause some hindrance to fusion in the more symmetric $^{19}\text{F}+^{181}\text{Ta}$ channel as compared to $^{16}\text{O}+^{184}\text{W}$.

Fission fragment mass distribution, which has been demonstrated as a sensitive probe [5] to quasi-fission, can shed light into the decay dynamics of the initial di-nuclear system formed. In particular, any entrance channel effect on mass distribution would suggest disintegration of the initial di-nucleus without mass equilibration i.e. quasi-fission. Thus measurement of fission fragment mass distribution can test the validity of the prediction of the DNS model framework.

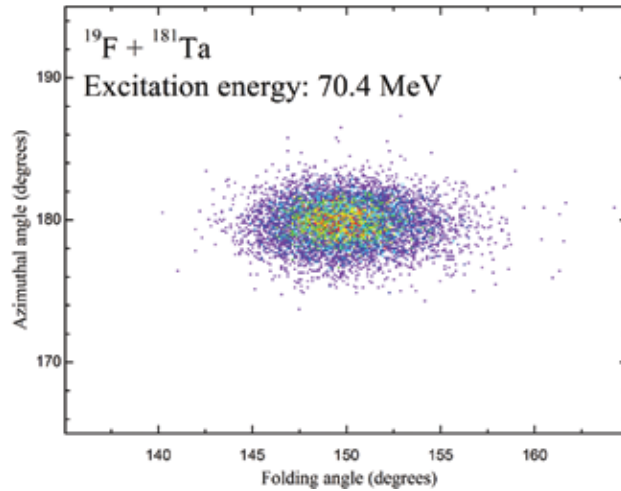


Fig. 5.1.25 Folding angle distribution of complementary fission fragments for the reaction $^{19}\text{F} + ^{181}\text{Ta}$.

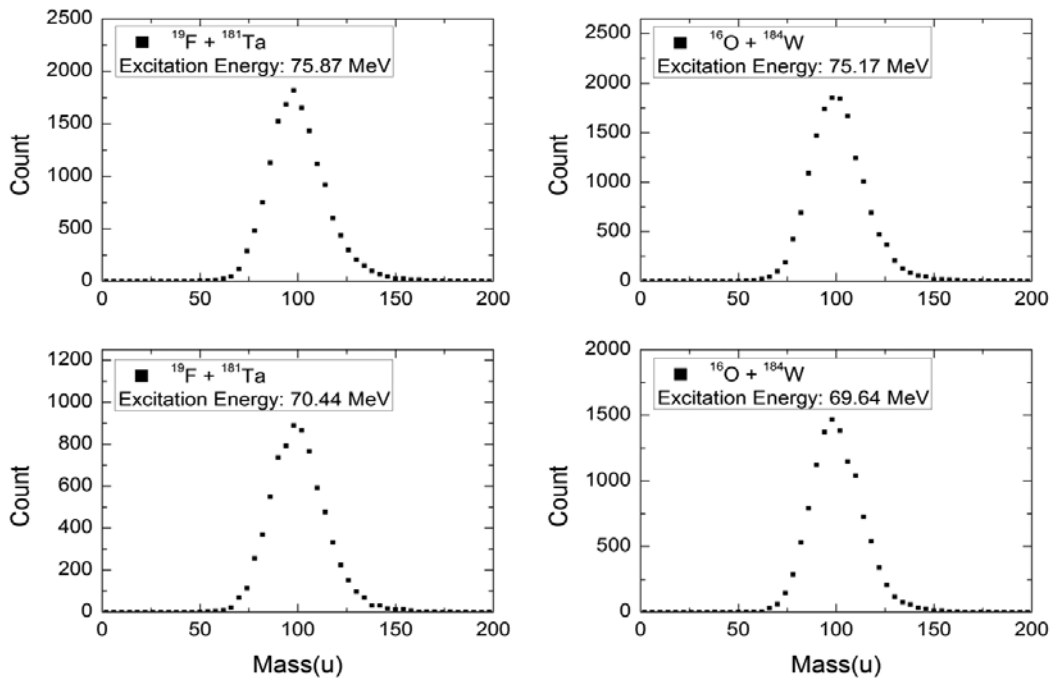


Fig. 5.1.26 Mass distributions of fission fragments at a few representative energies for both $^{19}\text{F} + ^{181}\text{Ta}$ and $^{16}\text{O} + ^{184}\text{W}$ at similar excitation energies.

The experiment to measure the fragment mass distributions in the reactions $^{19}\text{F}+^{181}\text{Ta}$ and $^{16}\text{O}+^{184}\text{W}$ was carried out at the IUAC Pelletron facility with pulsed beam of ^{19}F and ^{16}O using the General Purpose Scattering Chamber (GPSC). Fission fragments were detected with two large area position sensitive MWPC [6]. The detectors were placed at 41 cm and 29 cm from the target at angles corresponding to complementary fission fragments. The detectors were operated at a low pressure of 3 Torr of iso-butane gas so as to make them transparent to elastic and quasi-elastic particles. The flight time of the fragments, the coordinates of the impact points of the fragments on the detector (θ , ϕ) and the energy loss of the fragments in the gas detectors were recorded on an event by event basis to yield the fragment mass distributions. Beam flux monitoring as well as normalization was performed using a silicon surface barrier detector placed at forward angle and the Faraday cup.

Fig.5.1.25 shows typical folding angle (θ , ϕ) distributions of all fission fragments. The nature of the folding angle distribution is consistent with the expected value for complete transfer of momentum of the projectile. Preliminary mass distributions at a few representative energies are shown in Fig.5.1.26. The mass distributions are peaked at symmetric fission around $A_{\text{CN}}/2$. Ongoing investigation is expected to reveal the evolution of this mass distribution with excitation energy.

REFERENCES

- [1] V. S. Ramamurthy, S. S. Kapoor, Phys. Rev. Lett. **54**, 178 (1985).
- [2] D. J. Hinde, M. Dasgupta, et al, Phys. Rev. Lett. **74**, 1295 (1995).
- [3] P. D. Shidling, N. Madhavan, et al., Phys.Lett. B **670**, 99 (2008).
- [4] A. K. Nasirov, G. Mandaglio, et al., Phys.Lett. B **686**, 72 (2010).
- [5] T. K. Ghosh et al., Phys. Rev. C **79**, 054607 (2009); Phys. Lett.B **627**, 26 (2005); Phys. Rev. C **70**, 011604 (2004).
- [6] T. K. Ghosh et al., Nucl. Instrum.Meth.A **540**,285 (2005).

5.1.17 Two-quasiparticle band structures in ^{70}Ge

M.Kumar Raju^{1,2}, P. V. Madhusudhana Rao¹, S.Muralithar², R. P. Singh², G. H. Bhat³, J. A. Seikh³, S. K. Tandel⁴, P. Sugathan², T.Sheshi Reddy¹, B. V. Thirumala Rao¹ and R. K. Bhowmik²

¹Nuclear Physics Department, Andhra University, Visakhapatnam530003, India

²Inter-University Accelerator Centre, ArunaAsaf Ali Marg, New Delhi 110067, India

³Department of Physics, University of Kashmir, Srinagar 190006, India

⁴UM-DAE Centre for Excellence in Basic Sciences, Mumbai400098, India

The study of high spin structures and collective properties of nuclei in mass 70 region is of particular interest in recent years due to the observation of wide variety of nuclear phenomena with increasing angular momentum and excitation energies. The nuclei in this mass region show transitional character in nature with increasing proton or neutron number, which lies in between two magic numbers (Z or $N \sim 28$ and 50). Therefore the availability of a number of nucleons outside the closed shells favors this region to observe coexistence of prolate and oblate shapes (due to larger shell gaps which exist at $Z \sim N \sim 34, 36, 38$) and rapid shape transition between them.

The systematic observation of band structures in even-A Ge isotopes $^{66-70}\text{Ge}$ [1, 2, 3] shows interesting features as the low lying positive parity band structures built over different nuclear shapes. This is due to the occupation of valance neutrons and protons in unique parity $g_{9/2}$ orbital which plays an important role in deciding the structure of yrast and non-yrast band structures.

The ground state bands in these isotopes are based on two quasiparticle configurations involving alignment of a pair of $g_{9/2}$ neutrons. The observed ground state band structures in $^{66-68}\text{Ge}$ are forked into two different branches after their first band crossing. Infact, triple forking has been observed in ^{68}Ge at 6^+ state which evolves into two- quasiparticle band structures at high spins. Two of these band structures were interpreted as neutron quasiparticle states and the third 8^+ state was suggested to be continuation of oblate ground state band. In the present work, we have observed similar such forking in ^{70}Ge ; the ground state band is forked at 6^+ state into two distinct band structures and extended to high spins.

High spin states in ^{70}Ge nucleus have been populated via fusion evaporation nuclear reaction $^{64}\text{Ni}(^{12}\text{C}, 2p4n)^{70}\text{Ge}$ at an incident beam energy of 55 MeV. The target consisted of $\sim 1.5 \text{ mg/cm}^2$ thick isotopically enriched ^{64}Ni on a 7.5 mg/cm^2 thick gold backing. The ^{12}C beam was delivered by the 15UD Pelletron accelerator at IUAC. The de-excited γ -rays emitted in the reaction have been measured using the Gamma Detector Array (GDA) [4] at IUAC comprising of twelve Compton suppressed HPGe detectors. These detectors were arranged into three groups each consists of four detectors at 50° , 98° , and 144° with respect to the beam direction [3]. The distance between the target and the detector is $\sim 18 \text{ cm}$.

Two and higher fold Clover coincidence events were recorded using CANDLE, an online CAMAC based data acquisition system. The coincidence events were sorted into the conventional γ - γ symmetric matrices for construction of level scheme as well as asymmetric matrices for multipolarity assignments. The software package RADWARE [5] and INGASORT were used for the data analysis.

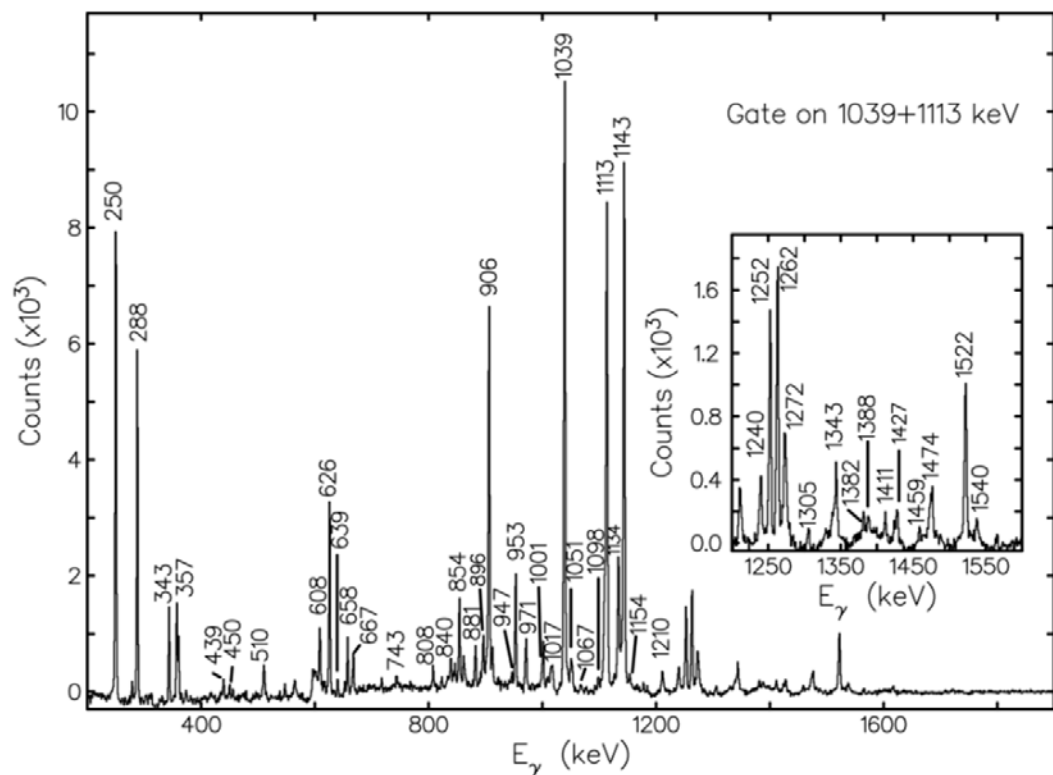


Fig. 5.1.27 γ -coincidence spectrum gated on 1039 and 1113 keV transitions of ground state band in ^{70}Ge

The ground state band in ^{70}Ge was known up to spin 12^+ in previous works. In the present work we have extended it to 14^+ through an addition of 1051 keV γ -ray transition. We have observed a new positive parity band built over ground state band due to forking at 6^+ state. This band is extended to 20^+ state through addition of five new γ -ray transitions on top of 10^+ state. The observed alignment in new positive parity band at $\hbar\omega \sim 0.53$ MeV is similar to the observed alignment ($\hbar\omega \sim 0.50$ MeV) in ground state band which are attributed to the configurations based on two neutron quasiparticle alignments. In addition, we have also observed several new γ -ray transitions in other positive and negative parity bands. A coincidence γ -ray spectrum gated on yrast ground state transitions is shown in Fig. 5.1.27, which illustrates the observed γ -ray transitions in ^{70}Ge along with the new ones. Detailed microscopic calculations are in progress to understand the nature of forking in positive parity band structures.

REFERENCES

- [1] E. A. Stefanova *et al.*, Phys. Rev. C **67**, 054319 (2003).
- [2] D. Ward *et al.*, Phys. Rev. C **63**, 014301 (2000).
- [3] M. Sugawara *et al.*, Phys. Rev. C **81**, 024309 (2010).
- [4] S. Muralithar, Pramana – J.Phys **82**, 769 (2014).
- [5] D. C. Radford, Nucl. Instrum.Meth. A **361**, 297(1995).

5.1.18 Feeding intensity profiles from spin distribution measurements in $^{16}\text{O}+^{159}\text{Tb}$ system

Vijay R. Sharma¹, P. P. Singh², Mohd. Shuaib¹, A. Yadav³, I. Bala³, S. Gupta⁴, M. K. Sharma⁵, D. P. Singh⁶, R. Kumar³, S. Muralithar³, B. P. Singh¹, R. P. Singh³, R. Prasad¹ and R. K. Bhowmik³

¹Accelerator Laboratory, Department of Physics, Aligarh Muslim University, Aligarh 202002, India

²Department of Physics, Indian Institute of Technology Ropar, Punjab 140001, India

³Inter University Accelerator Centre, ArunaAsaf Ali Marg, New Delhi 110067, India

⁴Physics Department, Agra College, Agra 282001, India

⁵Physics Department, S.V. College, Aligarh 202001, India

⁶Department of Physics, University of Petroleum and Energy Studies, Dehradun 248007, India

Recent studies on spin distributions for the system $^{16}\text{O}+^{169}\text{Tm}$, at ≈ 90 MeV beam energy show significantly different patterns in the spin distributions for the reaction products produced by complete fusion (CF) and incomplete fusion (ICF) processes [1, 2]. To get more information about input angular momentum involved for various degrees of ICF dynamics, a particle- γ coincidence experiment has been performed for the system $^{16}\text{O}+^{159}\text{Tb}$ at $\approx 4\text{-}7$ MeV/A projectile energy [3]. In this report, the deduced feeding intensity profiles (FIPs) from the spin distribution measurements of various residues at projectile energy 97.6 ± 1.4 MeV have been presented. It may be mentioned that FIPs is a direct evidence of feeding probability of γ population during the de-excitation of CF and ICF residues obtained from the analysis of spin distributions. The FIPs of evaporation residues ^{171}Ta (4n), ^{170}Hf (p4n)-B, $^{170,168,167}\text{Lu}$ (αn , $\alpha 3\text{n}$, $\alpha 4\text{n}$)-B and $^{168,167}\text{Lu}$ ($\alpha 3\text{n}$, $\alpha 4\text{n}$)-F populated via CF and/or ICF are plotted in Fig. 5.1.28 and 5.1.29. The 'B' and 'F' represent the reaction products identified from backward- α -gated spectra and forward- α -gated spectra, respectively. However, the neutron channels were identified from the singles spectra. It can be seen from Fig 5.1.28 that the feeding intensity for CF channels (4n) and (p4n) show a linear rise towards smaller l-values, which indicates a regular population with a strong feeding contribution for each γ transition up to minimum observed spins (J_{obs}). For better comparison of B and F α -channels populated via

ICF and CF, respectively, the feeding intensity patterns for backward α -channels, ^{168}Lu ($\alpha 3n$) and ^{167}Lu ($\alpha 4n$), along with forward α -channels, ^{170}Lu (αn), ^{168}Lu ($\alpha 3n$) and ^{167}Lu ($\alpha 4n$), have also been plotted in Fig. 5.1.29. As can be observed from Fig. 5.1.29 the FIPs of the αn channels identified from backward α -gated spectra shows a similar trend as that observed for xn and pxn channels. However, the FIPs for the ICF reaction channels show a relatively smooth rise to a peak followed by a reduction towards smaller l-value. This may be attributed due to less feeding probability in the ICF process caused by de-excitation of the residual nucleus. This trend indicates that the low-spin states do not contribute in the case of ICF channels and are less populated. Detailed results and discussions are documented in ref. [3].

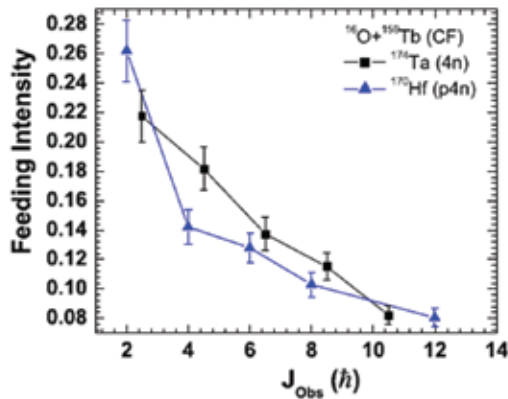


Fig. 5.1.28 Deduced feeding intensities of γ -cascades of different reaction products expected to be populated via (a) CF-4n, and CF-p4n. Lines and curves are drawn as guides to the eyes.

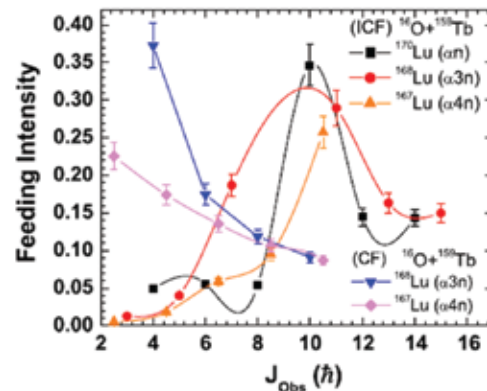


Fig. 5.1.29 Deduced feeding intensities of γ -cascades of different reaction products expected to be populated via CF- $\alpha 3n$, CF- $\alpha 4n$ (identified from backward- α -gated spectra), ICF- αn , ICF- $\alpha 3n$, ICF- $\alpha 4n$ (identified from forward α -gated subtracted from the backward- α -gated spectra). Lines and curves are drawn to guide the eyes.

REFERENCES

- [1] P. P. Singh *et al.*, Phys. Lett. B **671**, 20 (2009) and references therein.
- [2] P. P. Singh *et al.*, Phys. Rev. C **80**, 064603 (2009).
- [3] Vijay R. Sharma *et al.*, J. Phys. G: Nucl. Part. Phys. **42**, 055113 (2015).

5.2 MATERIALS SCIENCE

D. K. Avasthi

Various type of materials such as nanostructures, metallic, semiconducting and insulating were investigated either in form of thin film on substrate or bulk materials in form of pellets under low energy (up to a few hundred keV) and high energy ion (in regime of about 100 MeV) irradiations. There were seventy three irradiation experiments using high energy heavy ion beams from Pelletron. The experiments were in both beam hall I and beam hall II. The facilities of in-situ XRD, in-situ Raman and irradiation under high temperature were used in a few experiments in beam hall II.

The swift heavy ion irradiation of thin films of shape memory alloy NiTi was studied for the structural phases and phase transitions. The ion velocity effect in swift heavy ion induced mixing was studied in Ni/Bi bilayer films indicating that the low velocity ions cause higher mixing of bilayer at the interface. The radiation damage and retention of hydrogen and deuterium in irradiated Tungsten were studied. The resistive switching in Ar ion irradiated nanocrystalline TiO_2 was investigated. The influence of ion flux and ion fluence was studied on phonon modes under 300 keV ion irradiation by Raman spectroscopy.

It was observed that the enhancement in photo absorption and super paramagnetic behavior takes place under 300 keV Ar ion irradiation. The effect of 200 keV Ar ion irradiated carbon nitride films were studied. The p-n junctions were formed by Te implantation of p type InSb. The transport properties of PEDOT:PSS were studied under low energy ion irradiation. The disappearance of impurity phases were shown in Mn doped TiO₂ under ion irradiation. The structural evolution studies were performed in GaAs and InP under ion irradiation. The behavior of electrical of Ni/n-GaAs was studied under swift heavy ion irradiation. Other than these, the ZnO and TiO₂ films synthesized by different routes were investigated under ion irradiation.

It was shown that a monoclinic phase evolves in swift heavy ion irradiation of cubic Gd₂O₃. In-situ XRD studies revealed that the stress in GaFeO₃ film is created with swift heavy ion irradiation. The luminescence in Nd³⁺ doped Y₂O₃ was studied under ion irradiation. The morphology of the PZT films under swift heavy ion irradiation was studied by SPM and NSOM. The studies were performed on PVA containing Zn incorporated HAP coatings. The resistive switching behavior in ion irradiated LaCoCo₃ was studied under ion irradiation. The multi ferroics and different polymers were also investigated under ion irradiation. Swift heavy ion irradiation was used to generate the calibration curve for neutron dosimetry.

5.2.1 Study of swift heavy ion induced modifications of multiferroic epitaxial GaFeO₃ thin films

V. Raghavendra Reddy¹, Kavita Sharma², Ajay Gupta², D.K.Avasthi³ and Pawan Kumar Kulriya³

¹UGC-DAE Consortium for Scientific Research, Khandwa Road, Indore

²Amity Center for Spintronic Materials, Amity University, Noida

³Inter-University Accelerator Centre, Aruna Asaf Ali Marg, New Delhi 110 067

Epitaxial GaFeO₃ (GFO) film of 170 nm thickness grown on (001) oriented YSZ substrate is subjected to swift heavy ion irradiation (SHI) using 100 MeV Cu⁺ beam for different doses. The films were irradiated to different fluence and the in-situ 2θ-θ diffraction measurements are carried out as a function of fluence. In-situ 2θ-θ measurements are carried out using M/s Bruker make advanced D8 x-ray diffractometer installed at the materials science beam line of IUAC, New Delhi.

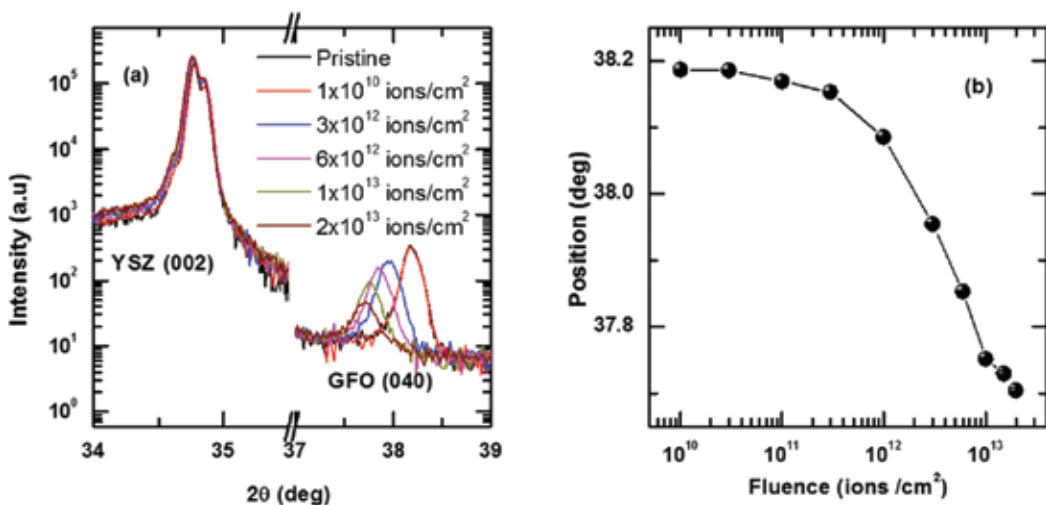


Figure 5.2.1: (a) 2θ-θ diffraction patterns recorded in-situ during the irradiation as a function of fluence (b) Variation of peak position of GaFeO₃ (040) reflection as a function of irradiation fluence.

Homemade sample holder mounted on a small goniometer controlled with *dc*- motor was installed on the x-ray diffractometer for sample alignment.

Figure-5.2.1 shows the in-situ XRD data and one can clearly see that no significant change is observed for YSZ substrate (matching with literature), but the film GFO (040) peak shifts to lower angles i.e., away from its bulk value, which implies the generation of stress with irradiation. The generation of stress with SHI is expected to have implications on the film morphology and crystallographic relation between the substrate and the film. To explore these aspects, reciprocal space mapping (RSM) measurements are carried out on the pristine and irradiated films at UGC-DAE Consortium for Scientific Research, Indore using M/s Bruker make D8- Discover HRXRD (high resolution x-ray diffractometer).

Figure 5.5.2 shows the RSM data of all the films measured in symmetric and asymmetric configurations i.e., about GFO (040) and GFO (062) reflections. The first conclusion that can be drawn from the RSM data is that the epitaxy is maintained even for the highest irradiated film i.e., 2×10^{13} ions/cm². The second striking observation that one can make is that for 2×10^{13} sample, the reciprocal lattice point corresponding to GFO (040) is not symmetric with the substrate lattice point. This is due to a tilt introduced between GFO and YSZ due to irradiation induced re-arrangement. Such tilts are known as Nagai tilt in literature, which is further confirmed from RSM measurements as a function of in-plane rotation (not shown). A tilt of about 0.18° is observed from the data. Such tilting is reported in perovskite thin films prepared on vicinal / miscut substrates and explained in terms of controlled structural anisotropy leading to anisotropic epitaxial relaxation. Therefore, the present measurements demonstrate conclusively that one can make use of ion irradiation to generate structural anisotropy in epitaxial films. The morphological and magnetic properties of GFO films are also affected (not shown) with SHI.

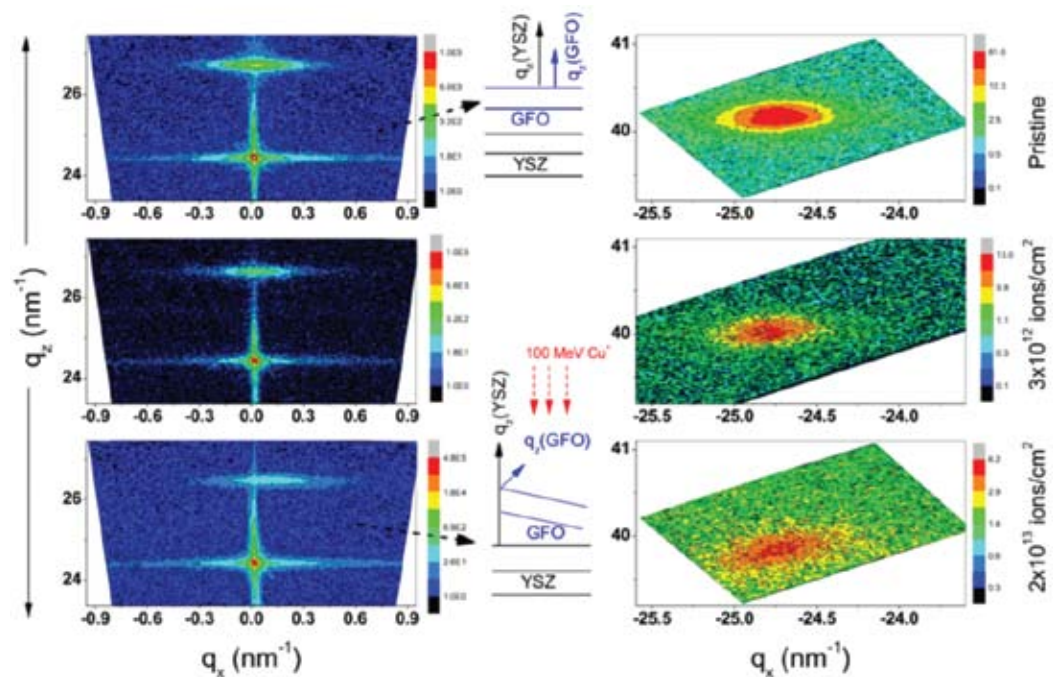


Figure 5.2.2: Reciprocal space maps (RSM) of pristine and irradiated GaFeO₃ films. (Left) RSM data for GFO (040) & YSZ (002) reflections. Bottom reflections are for YSZ (002) and the top reflections are for GFO (040). Note the shift of GFO (040) lattice point about YSZ (002) point for the film irradiated with 2×10^{13} ions/cm² implying a tilt of about 0.18° , known as Nagai tilt (shown by the schematic in the middle) induced by irradiation. (Right) RSM data for GFO (062) reflection implying the persistence of epitaxy till the highest irradiation dose.

5.2.2 Synthesis of zinc oxide nanostructures by swift heavy ion irradiation

Vidya U. Kondkar, Deepti. Rukade

Department of Physics, University of Mumbai, Mumbai 400 098, India

Zinc oxide films of thickness 100nm were deposited on fused silica substrates using e-beam evaporation method. These films were then irradiated with Au^{+9} ion beam with energy 120 MeV and fluence 1×10^{11} ions/cm². The energy of the Au ions in ZnO is calculated using SRIM software such that the beam passes through the film resulting in nanostructure formation at the surface. Post-irradiation films were characterized by Glancing angle X-Ray diffraction technique, Raman spectroscopy and UV-Visible spectroscopy.

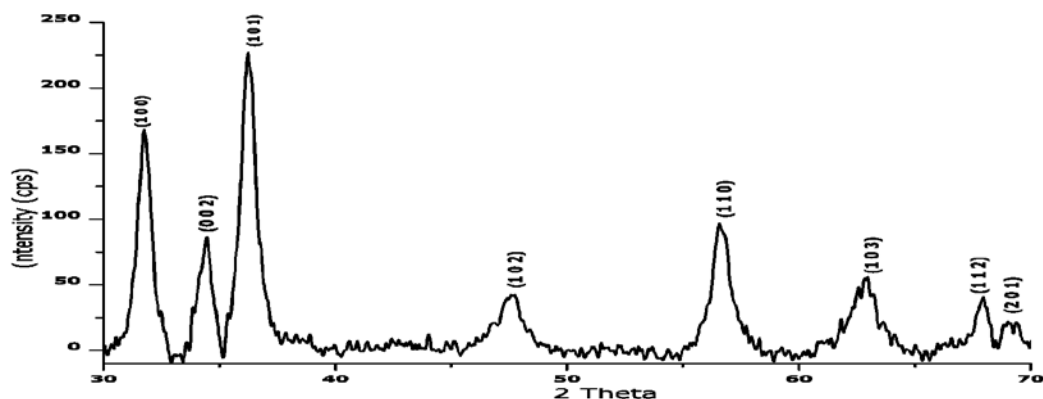


Figure 5.2.3: GAXRD pattern of irradiated ZnO thin film

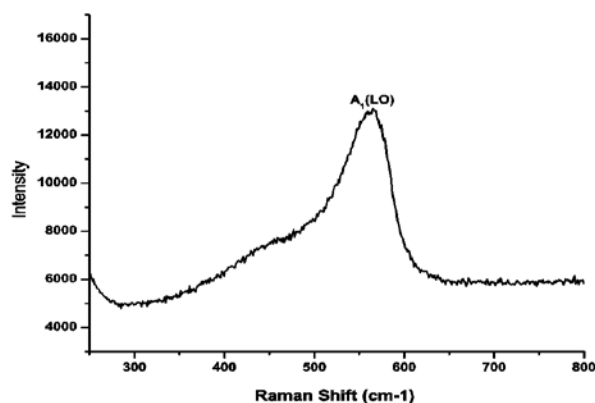


Figure 5.2.4: Micro-Raman spectra of irradiated thin film.

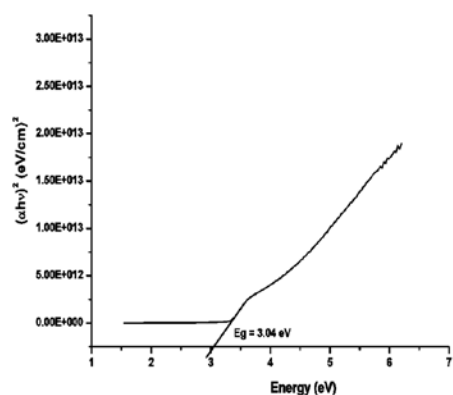


Figure 5.2.5: Band gap calculations from UV-Vis spectroscopy

Fig. 5.2.3 shows GAXRD pattern of the irradiated thin film. Diffraction peaks correspond to hexagonal wurtzite crystal structure of ZnO with lattice constant $a = 3.249 \text{ \AA}$ and $c = 5.205 \text{ \AA}$ (JCPDS card No.- 05-0664). Presence of the reflections at (100), (002), (101), (102), (110), (103), (112) and (201) planes indicate polycrystalline nature of the films. The average particle size determined by Debye-Scherrer formula is 11 nm which shows nanostructure formation. Fig. 5.2.4 shows Micro-

Raman spectra of irradiated thin film. Broad peak observed around 565 cm^{-1} is attributed to A_1 (LO) mode of ZnO. This softening of the phonon mode with theoretical value around 574 cm^{-1} is attributed to oxygen vacancies and irradiation induced stress in the film [1-3]. Fig. 5.2.5 shows band gap of calculated by Tauc plot for the irradiated film is 3.04 eV. In summary, we report the synthesis of ZnO nanostructures by Au ion irradiation of ZnO thin films. Surface morphology of irradiated films will be further studied using AFM.

REFERENCES

- [1] F. Singh, R. G. Singh, V. Kumar, S. A. Khan and J. C. Pivin, *Jour. App. Phys.*, 2011, 110, 083520.
- [2] M. Harati, D. Love, W. Lau and Z. Ding, *Materials Letters*, 2012, 89, 339–342
- [3] F. Singh, P.K. Kulriya and J.C. Pivin, *Solid State Comm.*, 2010, 150, 1751-1754.

5.2.3 Effect of 80 MeV Carbon ion irradiation on hydrothermally derived, elongated oxide nanostructures

Rizwin Khanam¹, Samiran Hazarika¹, D. Mohanta¹, and D.K. Avasthi

¹Nanoscience and Soft Matter Laboratory, Department of Physics, Tezpur University, Tezpur-784 028, Assam, India

²Inter-University Accelerator Centre, Aruna Asaf Ali Marg, New Delhi 110 067

The present work highlights the influence of 80 MeV C^{6+} ion irradiation on the morphological and structural responses of TiO_2 nanotubes and Gd_2O_3 nanorods. The elongated nanostructures were synthesized via a hydrothermal route [1,2] and later dispersed in a polymer matrix to help cast solid films. The formation of titaniananotubes and gadolinium oxide nanorods was confirmed through high resolution transmission electron microscopy (HRTEM) studies. As for irradiation experiment, 80 MeV C^{6+} ion irradiation was carried out in the Material Science chamber of IUAC, New Delhi, under high vacuum ($\sim 10^{-6}$ mbar) condition and using a beam current of ~ 1 pA. The fluence was varied in the range of 10^{11} - 10^{12} ions/cm².

Figure 5.2.6(a) depicts a TEM micrograph of a ~ 58 nm long, isolated multi-walled titania nanotube with an inter layer spacing of 0.32 nm. The multi-walled structure seems to be dismantled by energetic ion irradiation at a fluence of 3×10^{12} ions/cm² (Fig. 5.2.6(b)). The tubular structures are believed to be squeezed and bent as can be observed in the distributed view of the irradiated nanotubes (Fig. 5.2.6(b)). From XRD studies (not shown), the diffraction peaks located at $2\theta \sim 25^\circ, 38^\circ, 48^\circ, 55^\circ$ and 62° corresponded to the crystallographic planes of (101), (004), (200), (105) and (204) thereby representing anatase phase of TiO_2 [3]. Figure 5.2.6(c) represents a TEM micrograph of the randomly oriented Gd_2O_3 nanorods. From statistical analysis, the average length and diameter of the rods were found as ~ 116 nm and ~ 29 nm; respectively. As revealed from XRD studies (not shown), the pristine sample is characterized by four prominent peaks located at $2\theta \sim 28.59^\circ, 33.18^\circ, 47.59^\circ$ and 56.32° which corresponded to (222), (400), (440) and (622) planes of the cubic phase of the Gd_2O_3 system [4]. Upon irradiation, the Gd_2O_3 system of rods was found to undergo transformation from the cubic phase to the monoclinic one. At a low fluence (1×10^{11} ions/cm²), however, the irradiated Gd_2O_3 sample exhibited a mixed phase with coexistence of cubic and monoclinic phases. A reverse effect was previously encountered in case of Gd_2O nanoparticles subjected to low energy Ar ions [5].

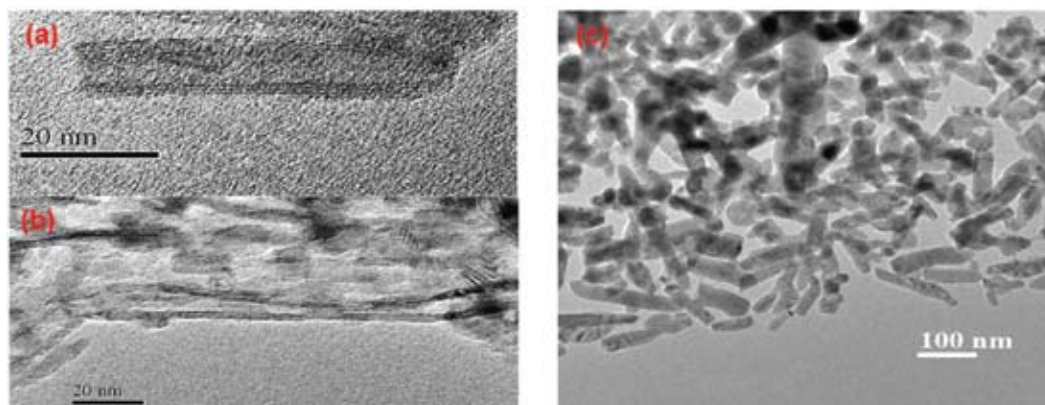


Figure 5.2.6: TEM micrographs of a) an isolated, multi-walled TiO_2 nanotube, b) distributed view of irradiated TiO_2 nanotubes, and c) randomly distributed nanorods of cubic phase Gd_2O_3 system.

REFERENCES

- [1] T. Kasuga, M. Hiramatsu, A. Hoson, T. Sekino, K. Niihara, *Langmuir* 14 (1998) 3160.
- [2] N. Dhananjaya, H. Nagabhushana, B.M. Nagabhushana, B. Rudraswamy, C. Shivakumara, R.P.S. Chakradhar, *Physica B*, 406 (2011) 1639
- [3] D.J. Park, T. Sekino, S. Tsukda, A. Hayashi, T. Kusunose, S.I. Tanaka, *J. Solid State Chem* 184 (2011) 2695.
- [4] N. Paul, S. Hazarika, A. Saha, D. Mohanta, *J. Appl. Phys.* 114 (2013) 134903
- [5] N. Paul, M. Devi and D. Mohanta, *Bull. Mater. Res.* 46 (2011) 1296

5.2.4 Study of the radiation induced modification in the properties of nanostructures

Pallavi Rana¹, Chetna Narula¹, Suresh Panchal¹ and R.P. Chauhan¹

¹Department of Physics, National Institute of Technology, Kurukshetra-136119, Haryana, INDIA

The nerve of exceptionality of the nanowires originated in their two dimensional confinement of flow of carriers that leaves only one degree of freedom for the transportation of the charge carriers. When diameter of the nanowires is of the order of Bohr exciton radius, the charge carriers are confined in two dimensions. This confinement endows nanowires with exceptional properties compared with their corresponding bulk counterpart [1–4]. The advancement in the engineering and exploration of the materials with radiation provides immense opportunities to mechanize the benefits of radiation in favour of mankind. The concept of engineering the properties and physics of the materials put a prospect to their functional applications in the field of radiation imaging, solar cells, and sensors etc. with minimum ecological disruption and resistant to radiation. Present work is an effort to study the ion beam irradiation effect on the electrical properties of semiconducting nanowires.

50 MeV Li^{3+} ion beam with a fluence variation of 3×10^{11} , 1×10^{12} , 3×10^{12} and 1×10^{13} ions/cm² was made incident on cylindrical cadmium selenate nanowires along their axis, perpendicular to both of its faces. The optical absorption spectra in pre- and post-irradiation cases were recorded for cadmium selenate nanowires embedded in polycarbonate membrane (Fig. 5.2.7). The absorption edge observed around 600 nm for the pristine case varied to 770 nm corresponding to irradiated nanowires. The absorption peak corresponds to 380 nm pragmatic to the membrane and remains invariant after irradiation even with nanowires embedded in it. The band gap of cadmium selenate nanowires varied from 1.96 eV to 1.31 eV as the fluence of the ion beam increases. I-V characteristics (IVC) of pristine nanowires showed almost symmetric non-linear nature; while an enhancement was found in the current with the increase in the ion fluence compared with pristine.

In another study, copper oxide selenite nanowire of 100 nm diameter were irradiated with 160 MeV Ni^{+12} ion beam along their axis with a fluence variation of 1×10^{11} , 3×10^{11} , 1×10^{12} , 3×10^{12} and 1×10^{13} ions/cm² and characterized their morphological, elemental, structural and electrical properties. In spectra of irradiated nanowires, no shifting and inception of any new peak was observed in the diffraction peaks. The IVC of the pristine and irradiated nanowires denotes the variation in the flow of charge carriers with an increase of ion fluence (Fig. 5.2.8). To assess the modifications in IVC of irradiated nanowires, the electrical conductivity was calculated using slope of the graphs and calculated value of the conductivity corresponds to one nanowire revealed enhancement in the charge conduction with the increase in ion fluence. Hence, ion irradiation onset the flow of the charge carriers and enhanced the conductivity of the nanowires.

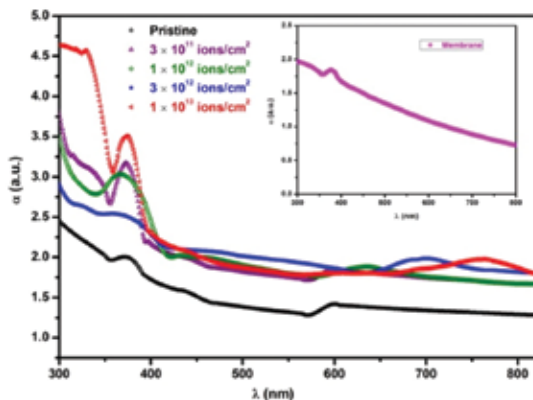


Figure 5.2.7: Optical absorption spectra of cadmium selenate nanowires [Rana & Chauhan, J Mater Sci: Mater Electron (2014). 25, 5630–5637]

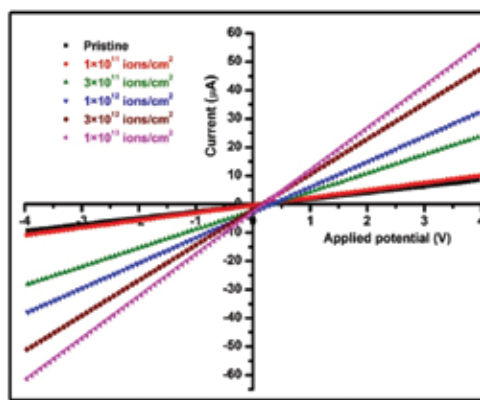


Figure 5.2.8: IVC of pristine and ion irradiated copper oxide selenite nanowires [Rana & Chauhan, Nucl. Instr. Meth. Phys. Res. B 349 (2015) 50–55]

REFERENCES

- [1] M. Tana, Y. Deng, Y. Wang, Nano Energy 3, 144 (2014)
- [2] C. Cheng, H.J. Fan, Nano Today 7, 327 (2012)
- [3] Chauhan RP, Gehlawat D, Kaur A, Rana P (2013) Radiation Effects & Defects in Solids 168(7–8):484–489.
- [4] Gehlawat, D. and Chauhan, R.P. (2014). Materials Chemistry and Physics, 145(1), 60-67.

5.2.5 Effect of high energy carbon ion beam irradiation on the electrocatalytic activity of carbon nanotube modified glassy carbon sensor

Rosy, Pankaj Gupta, Rajendra N. Goyal

Department of Chemistry, Indian Institute of Technology Roorkee, Roorkee -247667

Multi-walled carbon nanotubes (MWCNT) modified glassy carbon surfaces were irradiated with high energy carbon ion beam and the surface morphology of the irradiated sensor was analyzed using Raman spectroscopy, FE-SEM, AFM and Electrochemical Impedance Spectroscopy (EIS). Several glassy carbon sheets (10×10 mm²) coated with multi wall carbon nanotubes were irradiated with 50 MeV Carbon ion beam at a fluence of 1×10^{12} ions/cm² with 0.5 pA current. The irradiation leads to nanotubes with smaller length and diameter in comparison to the carbon nanotubes (CNT) present in the pristine form. The diameter of pristine CNTs was in the range of 20-150 nm which decreased to ~2-27 nm on exposure to high energy carbon beam. In EIS, the diameter of the circular portion of Nyquist plot for irradiated sensor reduced to almost half of that obtained for pristine MWCNT/GCE, which was further confirmed from the larger R_{CT} values of unirradiated MWCNT/GCE in comparison to that of irradiated MWCNT/GCE.

The purpose of these irradiation experiments was to explore the increase in the electro-catalytic activity of sensors after irradiation towards biomolecules oxidation. Several biomolecules such as dopamine, uric acid, guanosine, adenosine etc. were initially studied by electrochemical methods at irradiated and unirradiated sensors. In most of these cases, the peak current increased in the case of irradiated sensor, however, the shift in peak potential was relatively small, when voltammograms were recorded using differential pulse voltammetry. Detailed experiments are in progress.

5.2.6 100 MeV Si⁹⁺ ion irradiation effects on structural and antimicrobial properties of polypyrrole nanotubes-silver nanoparticle nanocomposites

J. Upadhyay and A. Kumar

Department of Physics, Tezpur University, Napaam, Tezpur-784028, Assam, India

Swift heavy ion irradiation offers the possibility of material modification at nanoscale with the nature of ion-matter interaction and structural modifications inside the target material depends primarily on the ion type, ion energy and fluence. Interaction of polymer with the high energy ion beam results in the formation of gaseous products along with degradation i.e., scissioning bonds and/or cross linking i.e., formation of intermolecular bonds as a results of which the properties of the target materials are modified [1]. In this report we present the effects of 100 MeV Si⁹⁺ swift heavy ion irradiation over polypyrrole nanotubes:silver nanoparticle (PPy NTs:Ag NPs) nanocomposites with four different fluences i.e., 5×10^{10} , 1×10^{11} , 5×10^{11} and 1×10^{12} of 100 MeV Si⁹⁺ ion beam. PPy NTs:Ag NPs nanocomposite with 15 wt. % of Ag NPs with respect to PPy NTs has been synthesized by two step chemical method. The nanocomposite is cast into film form by mixing with 2 wt. % polyvinyl alcohol to carry out the irradiation. We have investigated the effect of swift heavy ion irradiation on structural, morphological and antimicrobial properties of the nanocomposites.

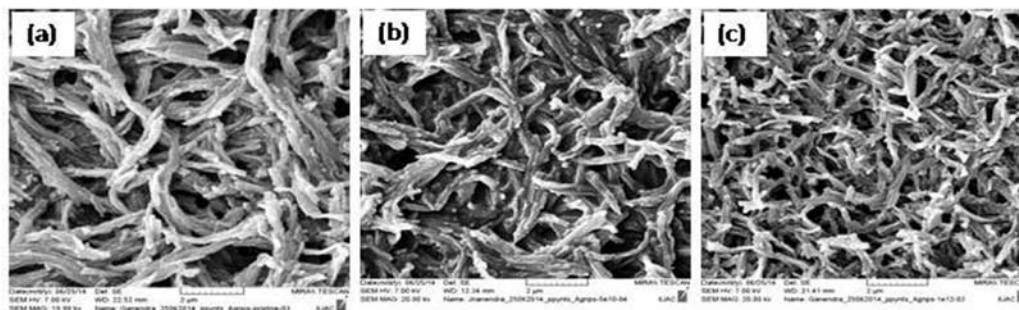


Figure 5.2.9: SEM image of PPy-NTs:Ag-NPs nanocomposites (a) pristine, (b) irradiated with 5×10^{10} ion/cm² and (c) 1×10^{12} ion/cm².

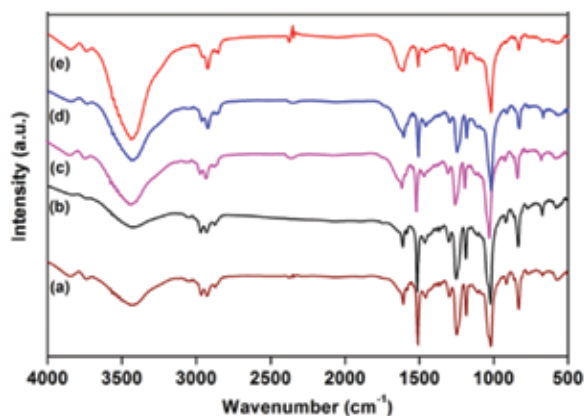


Figure 5.2.10: FTIR spectra of PPy-NTs:Ag-NPs nanocomposites (a) pristine, (b) irradiated with 5×10^{10} ion/cm², (c) 1×10^{11} ion/cm², (d) 5×10^{11} ion/cm² and (e) 1×10^{12} ion/cm².

The reduction in size and fragmentation of PPy NTs has been observed upon irradiation using scanning electron microscopy (Fig. 5.2.9), which is attributed to very high electronic energy deposition [2]. In the x-ray diffraction patterns of pristine and irradiated samples, Ag NPs exhibit diffraction peaks at $2\theta = 38.2^\circ$, 44.6° and 64.4° corresponding to the (hkl) values (111), (200) and (220), respectively in addition to the broad diffraction band centred at $2\theta = 25^\circ$ of PPy NTs. With the increase in ion fluence the intensity of the polymeric broad band decreases with no shift in 2θ position, suggesting a decrease in crystallinity of the nanocomposites. In the UV-vis spectra of the nanocomposites a broad absorption band at around 450 nm is attributed to the overlapping $\pi-\pi^*$ absorption of polypyrrole and surface plasmon resonance of Ag NPs. Slight blue shifting of the absorption maximum from 467 nm to 457 nm is observed in the case of sample irradiated with 5×10^{12} ion/cm² as compared to that of pristine sample. This band shifting is attributed to the decrease in conjugation length of polymer during swift heavy ion interaction. In the FTIR spectra of PPy NTs-Ag NPs nanocomposites (Fig. 5.2.10), the characteristics pyrrole ring stretching is observed at 1508 cm⁻¹. Band at 1457 and 1030 cm⁻¹ describes the C-N stretching vibration and C-H deformation vibration, respectively [3]. Bands at 1172 and 887 cm⁻¹ represents the doping state of polypyrrole. The intense band at 3150-3700 cm⁻¹ is attributed to the C-H and N-H stretching vibrations. It has been observed that upon increase in irradiation fluence the intensity of prominent bands of pyrrole decreases, which is attributed to the scissioning of polypyrrole chain leading to the increase in amorphicity within the sample. Antibacterial activity of pristine and irradiated PPy NTs:Ag NPs nanocomposites has been investigated by using diffusion plate method against both *Escherichia coli* and *Staphylococcus aureus* bacteria. The zone diameter is measured to be 12 mm for all the samples. No irradiation effect has been observed on the antimicrobial activity of the nanocomposites as there is no structural modification of Ag NPs due to irradiation. PPy NTs can also kill the bacteria due to electrostatic interaction between the positively charged PPy molecule and negatively charged bacteria cell membrane, but as the antimicrobial activity of PPy NTs is too less to produce clear zone in the diffusion plate method, no clear change in zone diameter is observed in the case of irradiated samples. It has been reported that the structural change of metal nanoparticles due to irradiation are observed at a fluence of 3×10^{13} ion/cm² [4]. Beyond the fluence of 1×10^{12} ion/cm², the polymeric matrix gets burnt. As the highest fluence used is 1×10^{12} ion/cm², no significant structural modification of the Ag NPs is expected.

REFERENCES

- [1] N.L. Singh, S. Shah, A. Qureshi, F. Singh, D.K. Avasthi, V. Ganesan, Polymer Degradation and Stability 93 (2008) 1088-1093.
- [2] D. Kanjilal, Current Science, 80 (2001) 1560-1566.
- [3] D. Zhanga, X. Zhang, Y. Chena, P. Yua, C. Wang, Y. Ma, Journal of Power Sources 196 (2011) 5990-5996.
- [4] M.C. Ridgway et al., Nuclear Instruments and Methods in Physics Research B 267 (2009) 931-935.

5.2.7 Ion velocity effect on SHI induced mixing

Nisha Bansal¹, Sarvesh Kumar¹, Saif Ahmad Khan², R.S. Chauhan³

¹Department of Physics, FET, Manav Rachna International University, Sector-43, Faridabad-121 001, India

²Inter-University Accelerator Centre, Aruna Asaf Ali Marg, New Delhi 110 067

³Department of Physics, R.B.S. College, Agra- 282 002, India

In a study of ‘swift heavy ions in insulating and conducting oxides’, it was mentioned that the velocity of the incident ion has a direct influence on the damage production: the lower the velocity,

the higher the damage [1]. Ion-velocity-dependent track formation in yttrium iron garnet [2] reported that for irradiations with low and high ion velocities the efficiency of the energy deposition in the thermal spike is 35% and 19%, respectively, leading to a lower damage cross section in the latter case. Recently in a study of Te/Bi bilayer system, it has been found that slower Au ions have considerable effect on mixing variance and higher sputtering yield compared to the higher velocity Ag ions [3].

In the present report we tried to explain the effect of different velocity of ions used for irradiation in Ti/Bi bilayer system having same value of electronic energy loss in Ti at room temperature. We used two different ions Au and Ag for irradiation at different energies with same value of S_e (~18.5 keV/nm) for Ti. Ti (100 nm), Bi (50 nm) and C (10 nm) was deposited on Si substrate at room temperature by electron gun in the high vacuum deposition system. Carbon layer is deposited on top to avoid oxidation of the samples. The velocity of 100 MeV Ag ions is greater than that of 80 MeV Au ions with the fact that S_e value remains the same for both ions at respective energies for Titanium. The samples were irradiated with both the ions to the fluences 1×10^{13} , 5×10^{13} and 1×10^{14} ions/cm². RBS was performed using 2 MeV He⁺ ions at scattering angle of 165°. The RUMP simulation was used for the analysis of RBS spectra and to generate the depth profiles. It has been found that mixing rate is higher for low velocity Au ions in comparison to high velocity Ag ions as can be seen from Fig. 5.2.11. The result could be explained as due to less energy deposition in thermal spike by high velocity Ag ions.

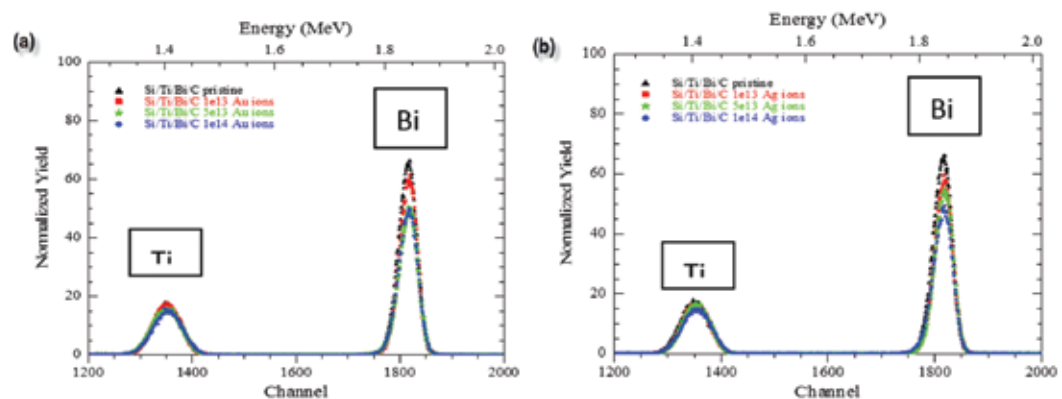


Figure 5.2.11: (a) RBS spectra of Si/Ti/Bi/C samples pristine and irradiated using 80 MeV Au ions (b) RBS spectra of Si/Ti/Bi/C samples pristine and irradiated using 100 MeV Ag ions

REFERENCES

- [1] M. Toulemonde, S. Bouffard and F. Studer, Nuclear Instruments and Methods in Physics Research B 91(1994) 108-123.
- [2] G. Szenes PHYSICAL REVIEW B VOLUME 52, NUMBER 9 1 SEPTEMBER 1995.
- [3] T Diana, D C Agarwal, P K Kulriya, S K Tripathi and H N K Sarma Indian J Phys (November 2014) 88(11):1163–1167.

5.2.8 Effect of 100 MeV Au ion irradiation on Ni/Bi bilayer system

V. Siva¹, K. Senapati¹, B. Satpati², S. Prusty¹, D. K. Avasthi³, D. Kanjilal³, and P. K. Sahoo¹

¹School of Physical Sciences, NISER, Bhubaneswar, Odisha 751005, India.

²Surface Physics and Materials Science Division, SINP, 1/AF Bidhannagar, Kolkata 700064, India.

³Inter-University Accelerator Centre, Aruna Asaf Ali Marg, New Delhi 110067, India.

Ni/Bi bilayers were prepared on Si substrates by thermal evaporation and it has been found that spontaneous formation of NiBi₃ phase at the interface of Ni and Bi films. This observed phase, confirmed by X-ray diffraction (XRD) and transmission electron microscopy, is a type-II superconductor with the transition temperature ~ 4 K, with large upper critical field (H_{c2}). A set of samples were made to irradiate with 100 MeV Au ions as a function of different ion fluences (1×10^{12} to 1×10^{14} ions/cm²) to confirm the robustness of the superconducting phase at radiation environments. Fig. 5.2.12 shows the XRD patterns of as-deposited films and irradiated films and the inset shows the variation of FWHM as a function of irradiation fluence. Fig. 5.2.13 shows the variation of critical field as a function of the transition temperatures for irradiated samples. The inset of Fig. 5.2.13 clearly shows an almost constant critical field throughout the irradiation fluences. This aspect of robustness in superconducting NiBi₃ makes it a suitable material for applications in high radiation environments. For more details of the above study, see *J. Appl. Phys.* 117,083902 (2015).

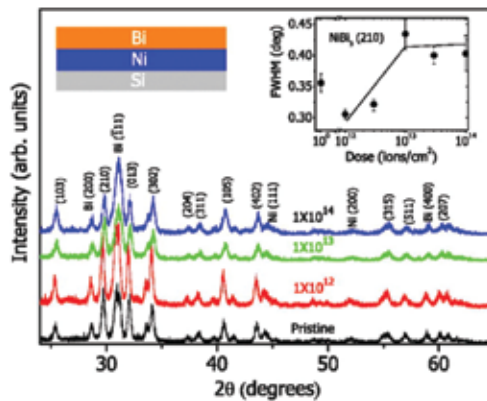


Figure 5.2.12: XRD patterns of the pristine and irradiated bilayers. All index peaks belong to NiBi₃, unless specified otherwise. Inset shows FWHM of NiBi₃ (210) peak as a function of ion fluences.

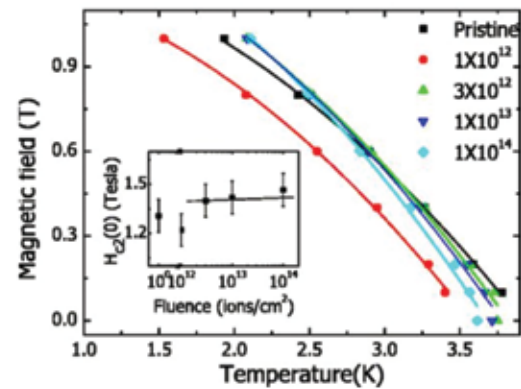


Figure 5.2.13: The field-temperature phase diagrams obtained from the R-T measurements for all samples. Inset: the zero temperature upper critical field, obtained as fitting parameters, as a function of fluences

5.2.9 Effects of transition metal Swift Heavy Ion Irradiation on 4H-SiC

A. Ashraf Ali¹, R. Mohankumar¹, K. Asokan², D. Kanjilal², J. Kumar¹

¹Crystal Growth Centre, Anna University, Chennai, India

²Inter-University Accelerator Centre, Aruna Asaf Ali Marg, New Delhi 110 067, India

Measurement of Raman shift provides information about the electronic states, defects and also prohibited optical modes. 4H-SiC was subjected to swift heavy ion irradiation of varying fluence to study the shift in the Raman lines with respect to the virgin sample. It is seen in this study that there

are previously unidentified optical modes surfacing on the spectrum alongside the characteristic modes of 4H-SiC. There is also a change in the relative intensity and the FWHM of these modes.

As seen in the Fig.5.2.14 (a), the $E_1(\text{TO})$ at 776.26 cm^{-1} mode appears as the dominant mode and the shape of the $A_1(\text{LO})$ mode at 981.53 cm^{-1} depends on the concentration of nitrogen doping in the 4H-SiC. The low intensity and the broadening of the peak denotes that the nitrogen levels are quiet high. On the other hand, the quality of the samples is high as we are able to see the second order acoustic modes around 500 cm^{-1} and between 1400 and 1800 cm^{-1} in Fig. 5.2.14(b).

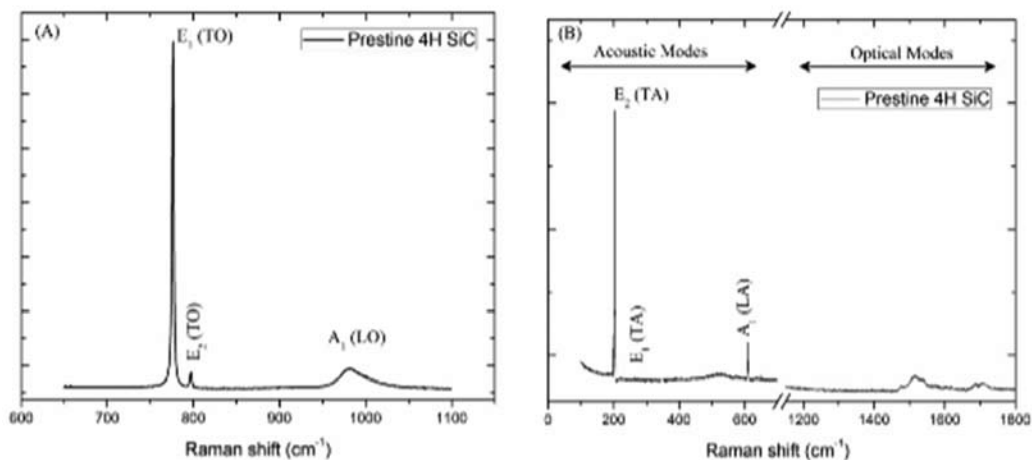


Figure 5.2.14: (a) first order Raman peaks and (b) second order Raman peaks

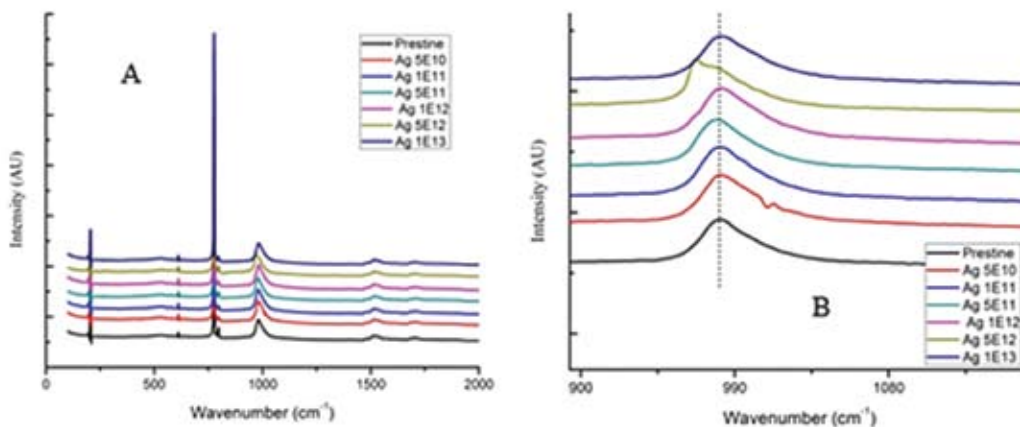


Figure 5.2.15: Raman Spectra of Ag ions irradiated 4H-SiC

The Fig. 5.2.15 (A) shows the spectra of pristine and Ag ions irradiated samples with the increasing fluence. It is noted from Fig. 5.2.15(B) that there is not much of a change in the spectra of the standard peaks. The Lorentzian fitting on the individual curves evidences that the FWHM remains almost constant with a slight variation of the intensity for all the spectra.

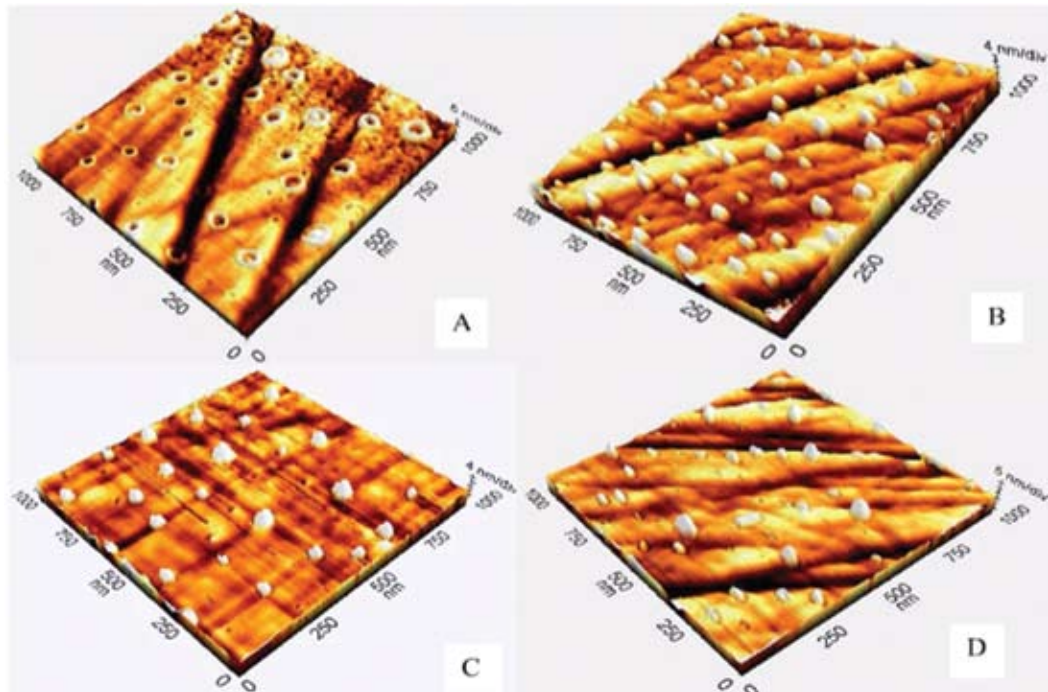


Figure 5.2.16: AFM images of SiC irradiated with transition metals Silver (Ag) and Nickel (Ni) ions with varying fluences A) 5×10^{10} B) 1×10^{11} C) 5×10^{11} D) 1×10^{12} ions/cm²

The AFM results (Fig. 5.2.16) and analysis provides adequate data of formation of pits due to the impact of the implantation leading to alloying of the materials and growth of hillocks as the fluence increases. It can be seen from the image that the increase of fluence leads to damage on the surface resulting in amorphous nature which can be concluded from the average roughness.

REFERENCES

- [1] Gallium Nitride (GaN) vs. Silicon Carbide (SiC) In the High Frequency (RF) and Power Switching Applications, in: Digikey Publitek.
- [2] S. Nakashima, H. Harima, Akademie Verlag, Berlin (1997) 39.
- [3] Ziegler F, Biersack J P, L. U, Stopping and Range of Ions in Matter (SRIM), in: 2013.
- [4] J. C. Burton, L. Sun, M. Pophristic, S. J. Lukacs, F. H. Long, Z. C. Feng, I. T. Ferguson, J. Appl. Phys 84 (1998).

5.2.10 Reduction of graphene oxide by 100 MeV Au ion irradiation

K Hareesh¹, K Asokan², D Kanjilal², S S Dahiwal¹, V N Bhoraskar¹, S D Dhole¹

¹Department of Physics, Savitribai Phule Pune University, Pune-411007, India

²Inter-University Accelerator Centre, Arun Asaf Ali Marg, New Delhi-110067, India

Graphene oxide (GO) is considered as a precursor for graphene synthesis which exhibits a large amount of oxygen functional groups such as hydroxyl, carboxyl and epoxy groups on its basal plane and edges, introducing sp³ defect sites and distorting the intrinsic conjugated π system that lowers the overall strength and conductivity [1]. GO can be reduced by different techniques like

Hydrazine, Thermal, Chemical doping, using transition metal oxide and by irradiation method [1]. When compared to other conventional chemical methods, irradiation method is termed as clean and efficient method to reduce the GO.

Raman spectroscopic results (Fig. 5.2.17(a)) showed the increase in disorder parameter after irradiation demonstrating the formation of large number of small sp^2 domain which is caused by the electronic energy loss transfer [2]. The electrochemical performance of GO showed improvement after irradiation (Fig. 5.2.17(b)). Figure 1 (a) shows the high resolution C1s XPS spectra of GO indicated the presence of C-C (284.5 eV), C-O (286.6 eV) and C=O (288.4 eV). Fig. 5.2.17(b) shows that, after gold ion irradiation the intensities of the peaks C-O and C=O decreased demonstrating the removal of oxygen containing groups which in turn indicates the reduction of graphene oxide [2,3]. The present work suggests that ion beams may be one of the clean methods for the reduction of graphene oxide [2].

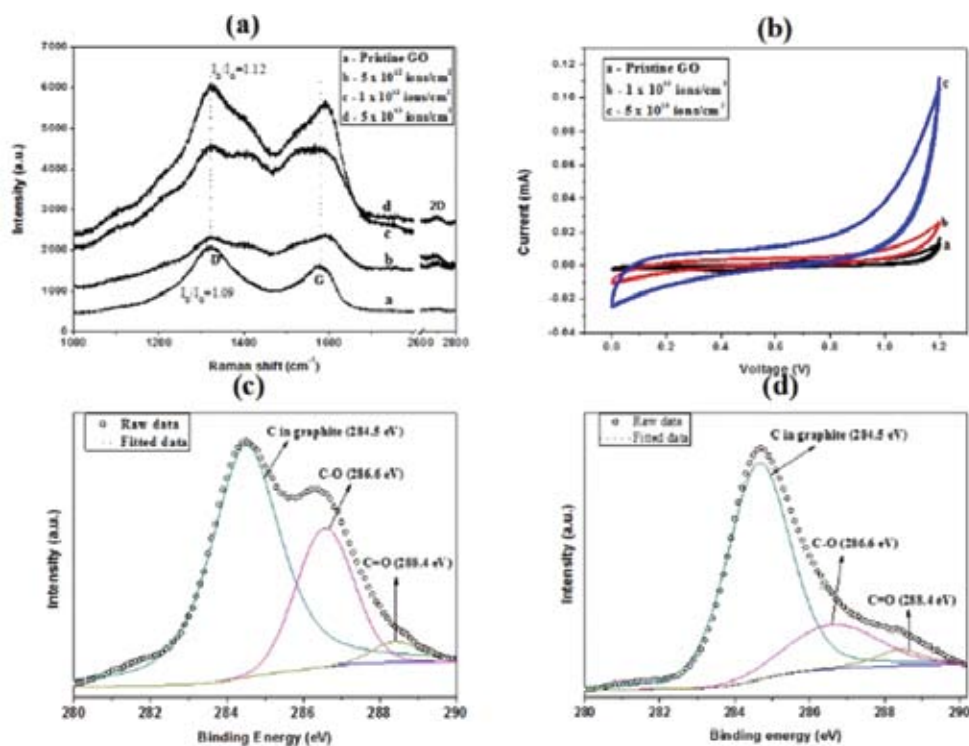


Figure 5.2.17: (a) Raman spectrum, (b) Cyclic voltammograms for GO and Au ions irradiated GO; Analysis of C1s spectra of (c) pristine GO (d) Au irradiated GO at a fluence of 5×10^{13} ions/cm².

REFERENCES

- [1] Chen D *et al.*, *Chem. Reviews* 112 (2012) 6027-53.
- [2] Hareesh K *et al.*, *Journal of Physics D: Applied Physics* (in press).
- [3] Zhang Y *et al.*, *J. Mater. Chem.* 22 (2012) 13064-9.

5.2.11 Swift heavy ion induced Optical and Structural modification in ZnO Thin Film

Shushant Kumar Singh¹, R. Singhal¹, V.V. Siva Kumar², D.K. Avasthi²

¹Department of Physics, Malaviya National Institute of Technology Jaipur, JLN Marg, Malaviya Nagar, Jaipur-302017, India

²Inter-University Accelerator Centre, Aruna Asaf Ali Marg, New Delhi-110067, India.

ZnO (N-type semiconductor) is a very promising material of II-VI group with wide band gap (3.35 eV) and used in many fields such as transparent conductive contacts, solar cells, laser diodes, thin film transistors, optoelectronics devices and gas sensors. There is a great scientific interest to fabricate a device which shows many interesting phenomenon due to functionality of the physical properties of oxides in ZnO type semiconductor. ZnO target (2 inch diameter) is prepared from ZnO powder (Alfa Aesar) using hydraulic press machine and sintered the target at 1200°C in tube furnace for 24 hours in the continuous flow of oxygen gas. ZnO thin films were deposited on glass and silicon substrate by RF sputtering technique, using ZnO target of 2 inch diameter and 3 mm thickness, in the presence of argon atmosphere in sputtering chamber. The films were irradiated with 100 MeV Ag⁷⁺ ions using the 15UD Pelletron accelerator at Inter University Accelerator Centre (IUAC) New Delhi in Materials Science beam line.

Pristine and irradiated thin films were characterized with different techniques such as Rutherford Backscattering Spectroscopy (RBS), XRD measurements, UV-visible spectroscopy, Raman Spectroscopy and Scanning Electron Microscopy (SEM). The structural properties has been studied by X-ray diffraction (Bruker D8 AXS diffractometer using CuK_α (1.5406 Å)) and it reveals that the film was grown in c-axis (002) orientation (Fig. 5.2.18(a)) at higher fluence and average crystallite size were increased from 10.8 nm up to 20.5 nm by increasing the ion fluence. Surface morphology has been investigated by atomic force microscope (Bruker) and scanning electron microscope (SEM). There is a marginal change in the roughness of film with ion irradiation estimated by AFM. Transmittance of films (Fig. 5.2.18(b)) was observed to decrease with an increase in ion fluences as confirmed by UV-visible spectroscopy (dual beam U-3300 Hitachi Spectrometer) so it can be used in different properties based on absorbance/transmittance of materials and easily tuned with ion fluence. Marginal change was observed in band gap of pristine and irradiated thin films with ion irradiation. Raman spectra of pristine and irradiated films are shown in Fig. 5.2.18(c).

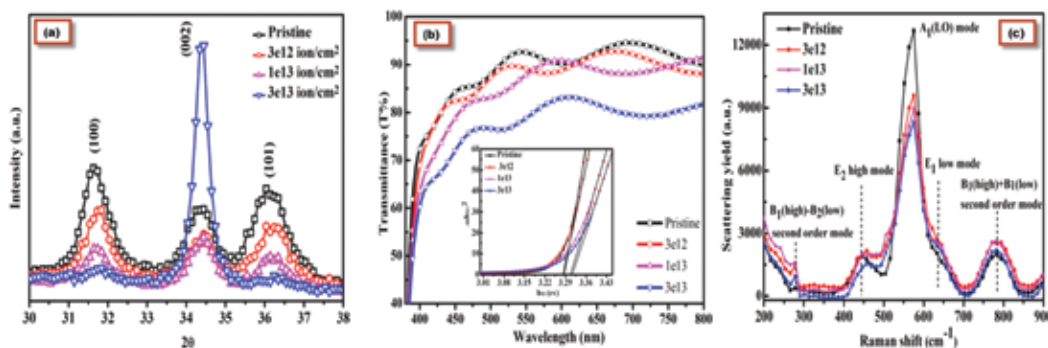


Figure 5.2.18: Pristine and 120 MeV Ag Irradiated ZnO film
(a) X-ray diffraction, (b) Transmittance spectra (c) Raman spectra

REFERENCES

- [1] D.C. Agrawal *et al.*, J.Phys. D: Appl. Phys. 41 (2008) 045305.
- [2] C.S. Chen, C.T. Kuo, T.B. Wu, and I.N. Lin, J. Appl. Phys. 36 (1997) 1169.

5.2.12 Ferromagnetism in oxygen ion irradiated SnO₂

A. Sarkar¹, D. Sanyal², P. Nath³, M. Chakrabarti³, S Pal³, S. Chattopadhyay⁴, D. Jana³ and K. Asokan⁵

¹Department of Physics, Bangabasi Morning College, 19 R. C. Sarani, Kolkata 700009

²Variable Energy Cyclotron Centre, 1/AF, Bidhannagar, Kolkata 700064

³Department of Physics, University of Calcutta, 92 A.P.C. Road, Kolkata 700009

⁴Department of Physics, Maulana Azad College, 8 Rafi Ahmed Kidwai Road, Kolkata 700013

⁵Inter-University Accelerator Centre, Aruna Asaf Ali Marg, New Delhi 110067

Defect-induced ferromagnetism in different metal oxide systems, which are otherwise diamagnetic, is a matter of intense research at present [1-3]. In this regard, ZnO has been studied most. Relatively fewer investigations exist on TiO₂ [4] and SnO₂ [5]. SnO₂ is a wide band gap (~ 3.6 eV at 300 K) n-type semiconductor. In the present study, density functional theory (DFT) has been employed to observe the effect of Sn and O vacancies on the electronic structure of SnO₂. The the *ab-initio* DFT calculations have been carried out using the code MedeA VASP based on linear basis set expansion. Super cell size is 2×3×3 *i.e.*, 108 atoms are taken for simulation with periodic boundary condition along the lattice vectors. DFT results predict that Sn vacancies are responsible for inducing ferromagnetism in SnO₂ (Table 5.2.1 & Fig. 5.2.19). On the experimental side, defects in SnO₂ have been created by 96 MeV oxygen ion beam (fluence 3.3×10¹³ions/cm²) from IUAC Pelletron. Doppler broadened electron-positron annihilation radiation lineshape (CDBEPARL) have been recorded in a dual ADC based-multiparameter data acquisition system (MPA-3 of FAST ComTec., Germany) having energy per channel – 146 eV. The peak to background ratio of this measurement system with ± Δ^E selection is ~ 10⁵:1. The CDBEPARL spectrum has been analyzed by evaluating the ratio curve analysis [6]. The magnetization measurements were done in a MPMS-XL SQUID (superconducting quantum interference device; Quantum Design) magnetometer. The irradiated sample has been found to be ferromagnetic (Fig. 5.2.20). Positron annihilation spectroscopic investigation reveals the abundance of more Sn vacancies compared to O vacancies in the irradiated material [7]. Further details have been reported in ref. 7. Our results agree well with the recent experimental and theoretical investigations on ferromagnetism in SnO₂ system [8].

Table 5.2.1. Theoretically calculated parameters (using DFT) for the non-defective SnO₂, oxygen vacancy incorporated SnO₂, and tin vacancy incorporated SnO₂.

System	Defect formation energy (eV)	Bond length (Å)	Magnetic moment (μB)
Pristine	0.0	1.952	0.0
V _O	8.69	1.842	0.0
V _{Sn}	16.0	1.884	3.63

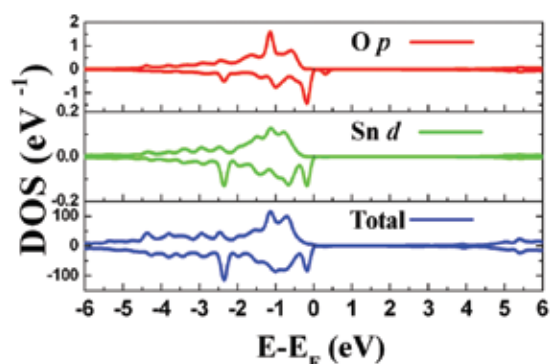


Figure 5.2.19: Spin polarized density of states for SnO₂ with Sn vacancy (Sn₁₅O₃₂)

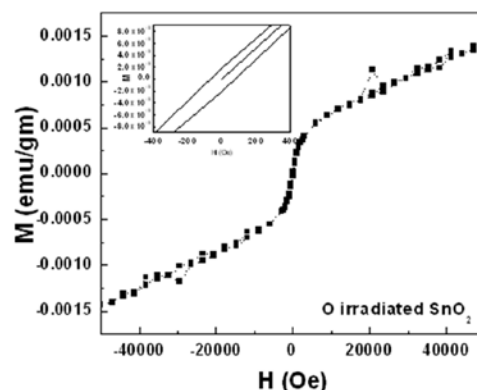


Figure 5.2.20: Room temperature magnetic hysteresis loop of O irradiated SnO₂

REFERENCES

- [1] S. Mal *et al.*, *Acta Mater.* 61, 2763 (2013).
- [2] S. Ghosh *et al.*, *J. Appl. Phys.* 114, 073516 (2013).
- [3] P. Satyarthi *et al.*, *J. Mag. Mag. Mater.* 385, 318 (2015)
- [4] D. Sanyal *et al.*, *J. Phys. D: Appl. Phys.* 47, 025001 (2014).
- [5] G. S. Chang *et al.*, *Phys. Rev. B* 85, 165319 (2012).
- [6] S. Dutta *et al.*, *J. Appl. Phys.* 98, 053513 (2005).
- [7] A. Sarkar *et al.*, *RSC Adv.* 5, 1148 (2015).
- [8] P. Chetri *et al.*, *J. Mater. Chem. C* 2, 9294 (2015).

5.2.13 Swift Heavy Ion irradiation induced phase transformation in undoped and Niobium doped Titanium Dioxide thin films

Subodh K. Gautam¹, Naina Gautam², R.G. Singh³, S. Ojha¹, and Fouran Singh¹

¹Inter-University Accelerator Centre, Aruna Asaf Ali Marg, New Delhi 110 067, India

²Department of Electronic Science, University of Delhi South Campus, New Delhi-110023,India.

³Department of Physics, Bhagini Nivedita College University of Delhi, New Delhi 110043, India

The Swift Heavy Ion Irradiation (SHI) effect on undoped and doped TiO₂ thin films has generated great interest for the fundamental understanding of phase transformation and the response of their physio-chemistry properties due to change in crystallite size, structural defects and stoichiometry and lattice parameters. Nb:TiO₂ is a unique semiconductor oxide material which exhibits salient superior properties for various applications such as transparent conductor solar cells, gas sensors and photo-catalytic applications [1, 2]. Present study is focused on the effect of SHI on the undoped and 5% Nb:TiO₂ thin films. The investigations were carried out mainly on doped anatase phase for study of their structural properties as structural defects, phase transformation and the phonon dynamics and to understand the underlying ion interaction processes. Hence, 120 MeV Ag ions irradiation was carried out on high temperature (900° C) annealed sol-gel synthesized thin films. The pristine (undoped and doped) films are highly stable in anatase phase (no contain of rutile phase). However, doped films show the weak existence of TiNb₂O₇ phase due to formation of new bonds of substitutional doped Nb with Ti and O atoms at high temperature. The Ag ion irradiation effect on undoped and doped films is studied by GIXRD and micro-Raman as shown in Fig. 5.2.21 (a & b). GI-XRD result reveals that at low fluence of 1×10^{11} ions/cm², the undoped film shows the

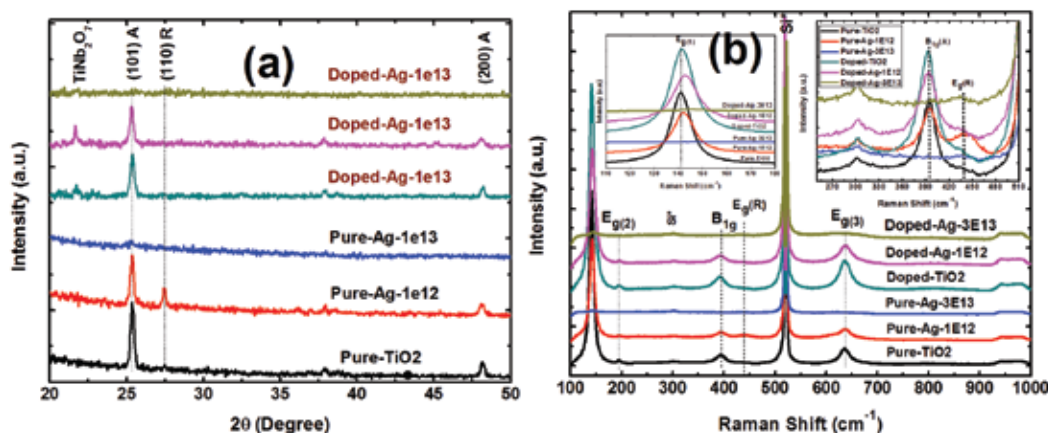


Figure 5.2.21: (a) GI-XRD spectra of pristine and irradiated films, and (b) micro-Raman spectra of pristine and irradiated films inset shows the variation in anatase E_g mode and the response of evolved rutile E_g mode.

partial anatase to rutile phase transformation. The further increase in fluence leads to decrease in the crystallinity of both anatase phase and rutile phase fraction and show completely disappearing of XRD peaks at fluence of 1×10^{13} ions/cm². However, the doped films remains stable in anatase phase with weak TiNb₂O₇ phase upto 1×10^{12} ions/cm² and no anatase to rutile phase transformation is occur. Similarly, further increase in fluence to 1×10^{13} ions/cm² leads to dissolution of weak TiNb₂O₇ and the amorphization of anatase TiO₂ phases. The phonon dynamics of various Raman modes of the anatase and rutile TiO₂ films under electronic excitation as are studied by micro-Raman as they are seldom reported [3].

Raman results reveals that pristine films exhibit all anatase Raman modes. The doped pristine films shows the initial small shift in peak position of main low frequency anatase E_g mode which demonstrate the presence of Nb doping in TiO₂ lattice. In contrast to GI-XRD results, the Raman spectra also exhibit the same anatase to rutile phase transformation at low fluence by the evolution of rutile E_g (R) and A_{1g} (R) Raman mode at fluence 1×10^{12} ions/cm² as shown in inset of Fig. 5.2.21(b). The further increasing the fluence to 1×10^{13} ions/cm², the all anatase and rutile Raman modes disappeared which show the nano-crystallization followed by amorphization in both doped and undoped films. However, the E_g mode of anatase phase shows the stiffening along with increase peak width as increasing the fluence dose. No TiNb₂O₇ phase is detected in Raman spectra of doped films. The stiffening of E_g Raman mode is attributed to disorder in TiO₆ octahedra by producing the oxygen vacancy and reduction of crystallite size in the framework of phonon confinement model [4]. The Ag ion leads to reduction in crystallite size and increase in the non-stoichiometry of both undoped and doped films with increase in fluence. In our previous study, it is well evidenced that Ag ions are registered to produce ion tracks by deposited electronic energy loss 20.61 keV/nm is more than the threshold energy 12.12 keV/nm in TiO₂[3]. Therefore, at low fluence, the deposited energy produces the non-stoichiometry and increases the sufficient oxygen vacancies in the lattice which act as nucleation sites for the growth of rutile phase [5]. However, in case of doped films the deposited energy is dissipated to the grain boundaries and to composite phase of TiNb₂O₇ which inhibit the nucleation to the rutile phase. The further increase in fluence of 1×10^{13} ions/cm² resulting in overlap of the registered ion tracks and production of huge density of oxygen vacancies and non-stoichiometry in lattice which leads to nano-crystallization followed by amorphization of TiO₂ anatase and rutile phases and other phases. The results are further evidenced by various other characterization techniques which is published elsewhere. The fundamental understanding of interaction, involved processes and tailoring capabilities will be exploited for the development of new class of conducting oxides, to improve the performance of solar cells, sensors and optoelectronic devices.

REFERENCES

- [1] V.L. Kuznetsov, Mrs Bull. 25 (2011) 15–18.
- [2] X. Lü, X. Mou, et al., Adv. Funct. Mater. 20 (2010) 509–515
- [3] Subodh K. Gautam, Fauran Singh, et al J. Appl. Phys. 115, 143504 (2014).
- [4] D. Bersani, et al., Appl. Phys. Lett. 72 (1998) 73–75.
- [5] J. Arbiol, et al., J. Appl. Phys. 92 (2002) 853–861.

5.2.14 100 MeV Si Ion Irradiation Effect on Multiferroic nanocomposite

Renuka Chauhan¹, R. C. Srivastava¹, H.M. Agrawal¹ and K. Asokan²

¹G. B. Pant University of Ag. and Technology Pantnagar, 263145 Uttarakhand, India

²Inter-University Accelerator Centre, Aruna Asaf Ali Marg, New Delhi 110 067, India

SHI irradiation with suitable energy and fluence generates structural strain as well as columnar amorphization in multiferroic materials [1,2]. Presently we are reporting the effect of irradiation of 100 MeV Si^{8+} beam on structural and dielectric properties of multiferroic nanocomposite.

Barium Zirconate-Nickel Zinc Ferrite (ZF40) composite was prepared by Solid state reaction method and irradiated with 100 MeV Si^{8+} beam at fluence 5×10^{13} ions/cm². X-ray diffraction (XRD) of pristine sample confirms the Perovskite phase formation with small spinel phase of ferrite as evident in fig. 5.2.22(a). The XRD pattern show that composite loses their crystallinity at higher fluence (5×10^{13} ions/cm²). The observed structural disorder may be due to strain as well as columnar amorphization induced by SHI. Fig. 5.2.22(b) shows the dielectric response of composite with respect to temperature. The dielectric loss at 100 kHz shows decrement after irradiation with Si^{8+} ion beam. The dielectric loss indicates stability in temperature ranges from 100 to 200K and 320 to 380K which are useful from application point of view. We also found a shift in transition temperature from 220 to 330K which corresponds to Barium Zirconate. Further analysis is underway.

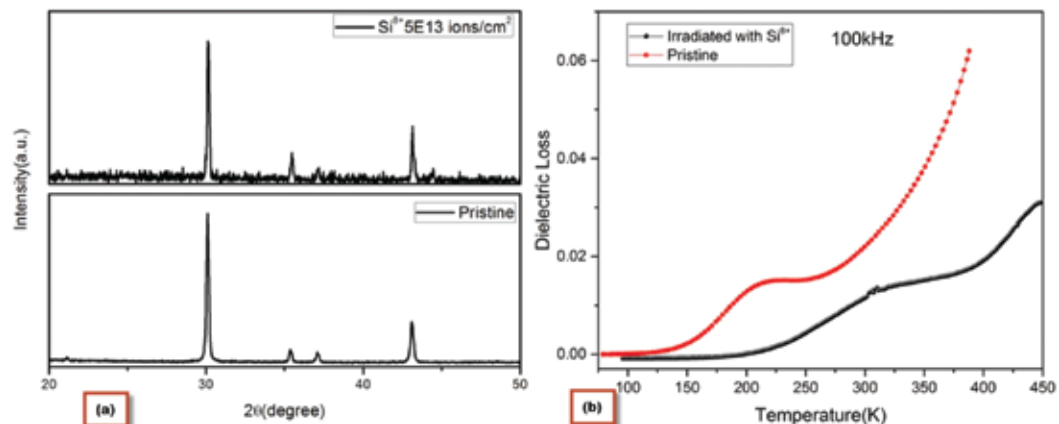


Figure 5.2.22: (a) XRD pattern and (b) Dielectric constant vs. Temperature for pristine and irradiated ZF40 sample.

REFERENCES

- [1] S. Shanmuga Sundari, Binay Kumar, K. Asokan and R. Dhanasekaran, Applied Surface Science 265 (2013) 296– 301
 [2] R. N. Parmar et al., Applied Physics Letters 89 (2006) 202506.

5.2.15 Swift heavy ion induced structural modification in $\text{Ni}_{0.58}\text{Zn}_{0.42}\text{Fe}_2\text{O}_4$ nanoferrite

Sarveena¹, Sucheta Sharma¹, K. Asokan² and M.Singh¹

¹Department of Physics, Himachal Pradesh University, Shimla-171005

²Inter-University Accelerator Centre, Aruna Asaf Ali Marg, New Delhi 110 067, India

Ferrites have a plethora of applications in the myriad fields of technology. Among the soft ferrites, NiZn ferrites are one of the most versatile well-known mixed spinel ferrite, widely used because of its multipurpose and outstanding properties such as high resistivity, high dielectric, high initial permeability, mechanical hardness, high Curie temperature, chemical stability, high saturation magnetization and lower power loss [1]. In magnetic materials the super-exchange interactions between the magnetic ions is highly sensitive to any change in the crystallographic positions leading to change in the magnetic properties. Swift heavy ion (SHI) irradiation provides interesting

tool in understanding the damage creation and materials modification. The magnetic interactions, especially the superexchange interactions, are highly sensitive to any change in bond length, bond angle, cation distribution and the defects present in the materials [2]. In the present work, we report structural studies of substituted NiZn nanoferrites irradiated with 200 MeV Ag beam and 100 MeV Oxygen beam respectively.

XRD was performed to ensure the single phase nature of the prepared nanoferrite samples and to study the structural changes induced by ion beam irradiation. Fig.5.2.23 (a) and (b) shows XRD pattern for the pristine and irradiated samples with 200 MeV Ag beam and 100 MeV Oxygen beam respectively. It is evident from the figures that the basic single-phase spinel structure remains practically the same after irradiation. On the other hand, parameters such as the peak intensities, peak positions and widths are slightly altered, which may be due to the fact that SHI has generated some defect states in the system. The peak position slightly shifted towards higher side after irradiation which may be due to the stress induced by the irradiation. Crystallite size remains almost constant. Slight increase in crystallite size (Table 5.2.2) for higher fluence may be due to the agglomeration of nanoparticles [3]. The heat produced by SHI may amorphize the materials such that the closely placed nanoparticles agglomerate to form larger size particles.

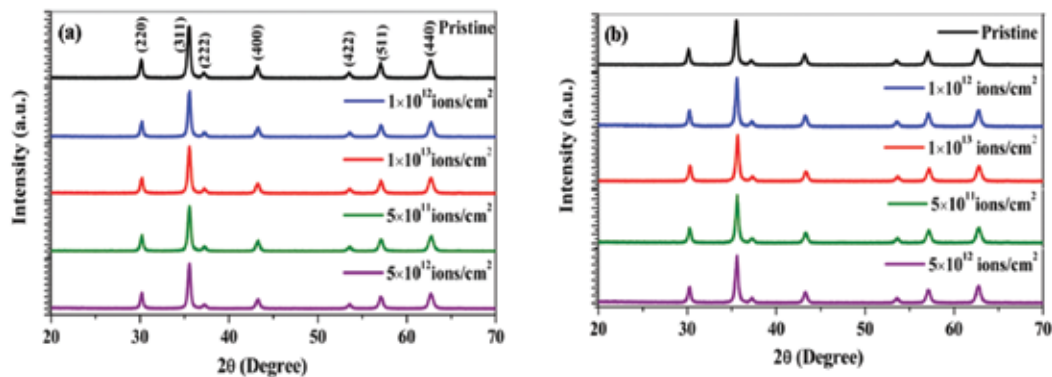


Figure 5.2.23: XRD spectra of $\text{Ni}_{0.58}\text{Zn}_{0.42}\text{Fe}_2\text{O}_4$ nanoferrite irradiated with (a) 200 MeV Ag beam (b) 100 MeV O beam

Table 5.2.2. Variation of crystallite size with (a) 200MeV Ag beam and (b) 100 MeV O beam

(a)		(a)	
Fluence (ions/cm ²)	Crystallite size (nm)	Fluence (ions/cm ²)	Crystallite size (nm)
Pristine sample	20.81	Pristine sample	20.81
1×10^{12}	21.71	1×10^{12}	21.80
1×10^{13}	20.21	1×10^{13}	20.26
5×10^{11}	20.31	5×10^{11}	20.96
5×10^{12}	21.25	5×10^{12}	20.07

REFERENCES

- [1] A. S. Albuquerque, J. D. Ardisson and W. A. A. Macedoa, Journal of Applied Physics, 87 (2000) 9.
- [2] A. Dogra, R. Kumar, S.A. Khan, V.V. Siva Kumar, N. Kumar and M. Singh, Nucl. Instr. Meth.in Physics Research B, 225 (2004) 283.
- [3] S.K. Sharma et al., Nucl. Instr. Meth. in Phys. Res. B, 248 (2006) 37.

5.2.16 The effect of 120 MeVAg⁹⁺ irradiation on the composite ferrites

N. R. Panchal¹, R. B. Jotania² and F. Singh³

¹Department of Physics, M. G. Science Institute, Ahmedabad, India

²Department of Physics, Gujarat University, Ahmedabad, India

³Inter-University Accelerator Centre, Aruna Asaf Ali Marg, New Delhi 110 067, India

Objective of present investigation is to study the effect of Ag⁹⁺ SHI irradiation on synthesized composite ferrite containing Spinel and Hexaferrite with different weight ratio. There is no report which shows the effect of irradiation on composite ferrites. The composites of CoFe₂O₄-SrFe₁₂O₁₉ ferrite nanoparticles were prepared by Self-propagating High temperature Synthesis (SHS) route. The composition of Soft ferrite, CoFe₂O₄ and Hard ferrite, SrFe₁₂O₁₉ were made in two different weight ratios of 1:1 and 1:2. The codes given here for these samples are SH11 and SH12 respectively. These nanocrystalline composite ferrites were irradiated with 120 MeV Ag⁹⁺ ions to five different fluences of 3×10¹¹, 1×10¹², 3×10¹², 1×10¹³ and 2×10¹³ ions/cm².

To study the SHI induced modification in structural properties, the samples before and after irradiation were characterized by using Fourier Transform Infrared (FTIR) spectroscopy and X-Ray Diffractograms (XRD). With the irradiation, the impurities due to some nitrates and moisture; which were present in both the samples got removed. The absorption peaks at 440 and 580cm⁻¹ are clearly formed which is the evidence of ferric oxide formation.

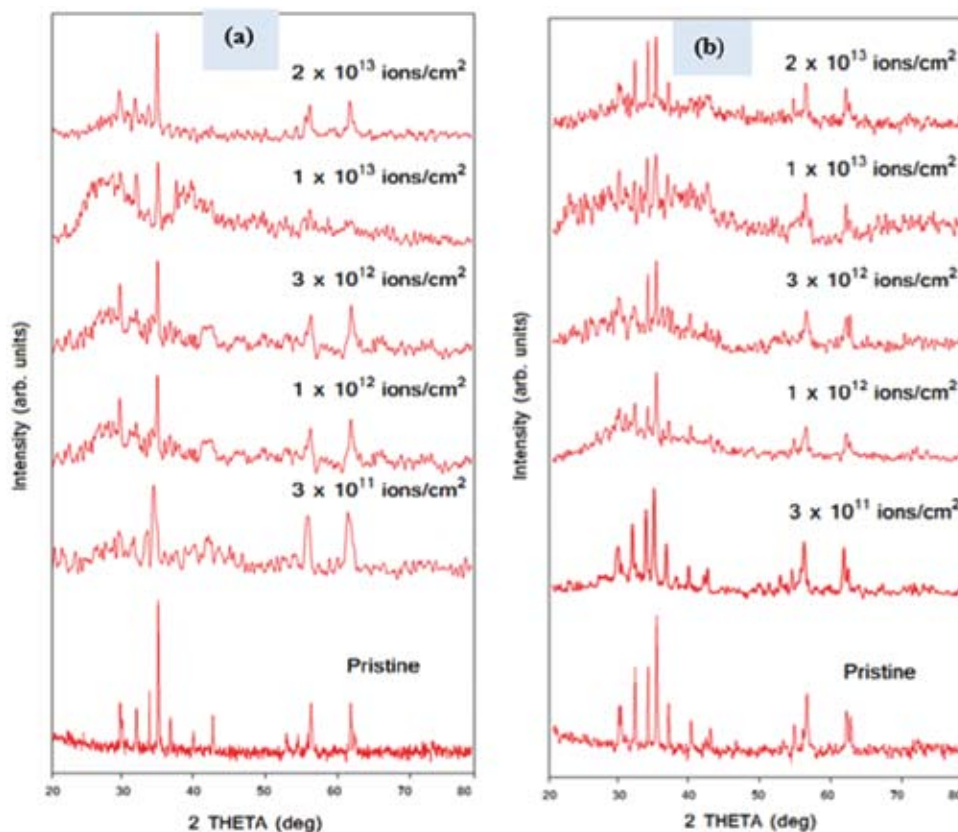


Figure 5.2.24: XRD of samples (a) SH11 and (b) SH12 Pristine and irradiated

As shown in Fig. 5.2.24 (a), pristine sample of SH11 gives the mixed phase of Spinel ferrite and M-type ferrite with 1:1 ratio. With increasing the fluence of irradiation, the Spinel-M hexaferrite phase changes to W-type hexaferrite. For sample SH12 (Fig. 5.2.24(b)), mixed phase diffuses and M-type phase matching has increased with increasing fluence. At highest fluence, pure M-phase is achieved.

Further supporting characterizations like measurement of dielectric and magnetic properties, surface morphology and data analysis are in progress for drawing more conclusive features in this system.

5.2.17 Resistance switching and structural properties of 120 MeV Au⁺⁹ irradiated LaCoO₃ (LCO) Thin film nanostructures

Nirav C. Pandya¹, U.S. Joshi¹ and D. K. Avasthi²

¹Department of Physics, School of Sciences, Gujarat University, Ahmedabad-380 009

²Inter University Accelerator Centre, Post Box-10502, New Delhi-110 067

Resistive Switching (RS) phenomena had been extensively observed and analyzed in recent times and oxide perovskite materials are mostly used by the researchers to study the RS phenomena and subsequently its potential use as resistive random access memory devices [1]. In present work, perovskite LaCoO₃ (LCO) was chosen as functional oxide material. LCO solution was made by Polyvinyl Alcohol (PVA) route and was spun coated on Fluorine doped Tin Oxide (FTO) Glass substrates [2].

To prepare LCO solution, stoichiometric amount of La(NO₃)₃·6H₂O and Co(NO₃)₂·6H₂O were added in the mixture of 2.5 %wt. Poly vinyl alcohol dissolved distilled water. Solutions were stirred till clear and homogenous solution was found. The 0.2 M solutions were aged for 48 hours and no precipitates were found. Solution were deposited on FTO substrates (Aldrich) and dried at 250°C by spin coating technique. This process was repeated for all samples till desired thickness was achieved. Samples were finally sintered at 500°C for 1 hour. Five identical samples were irradiated by 120 MeV Au⁺⁹ ions with different fluence of 10¹¹ ions/cm² and 10¹² ions/cm² in UHV at MS beam line of IUAC, New Delhi. GIXRD and AFM results are shown in Fig. 5.2.25.

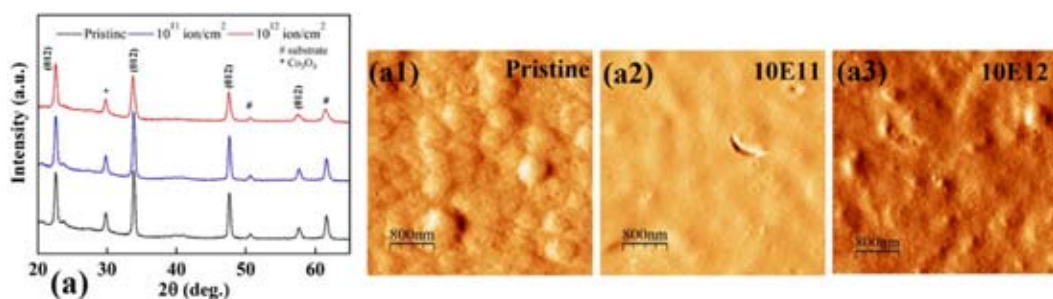


Figure 5.2.25: (a) GIXRD pattern of pure and irradiated LNCO films grown on FTO coated glass (a1-a3) AFM images of pure and irradiated films with different fluences

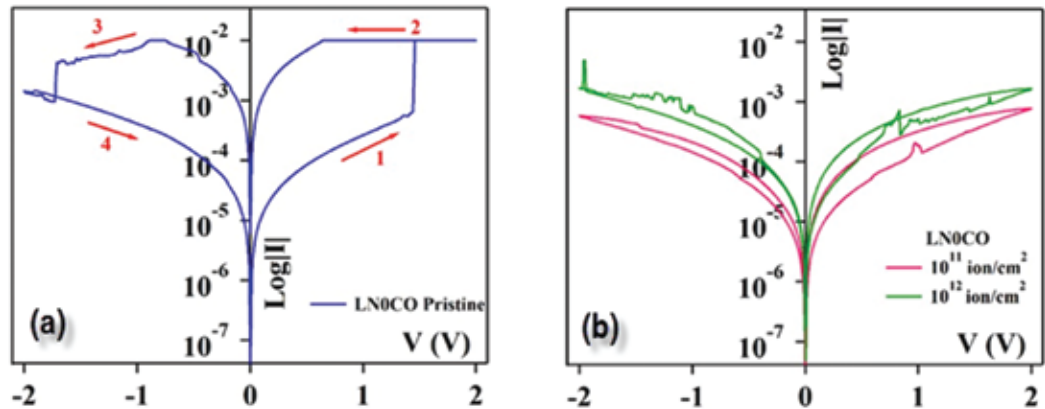


Figure 5.2.26: I-V plots of (a) pristine and (b) SHI irradiated Al/LNCO/FTO sandwich structure

Resistance switching was observed in LCO pristine samples (Fig. 5.2.26(a)). The MIM structure Al/LCO/FTO was found to switch from high resistance state (HRS) to low resistance state (LRS) at +1.4V (Fig. 5.2.26(b)). Resistance switching (RS) ratio was found to be more than one order of magnitude. All samples when irradiated, regardless of any fluence, did not show any RS effect. Irradiated LCO films showed linear or rectifying current voltage relation. The observed behaviour is attributed to the oxygen vacancies being compensated in crystal structure upon SHI irradiation and the decrease in the oxygen vacancy eliminates the switching effect. Further, the interface between LCO/FTO may have role to play in vanishing the RS, which needs to be checked.

REFERENCES

- [1] X.-J. Zhu, J. Shang and R. W. Li, *Front. Mater. Sci.* 2012, 6(3): 183–206
- [2] Nirav C. Pandya and U.S. Joshi, *J. Mater. Sci.: Mater. for Electr. J. of Mater.Sci.: Mater. in Electronics*, 26:2445–2450 (2015)

5.2.18 The Effect of 120 MeV Au⁹⁺ Ion Beam Irradiation on Structural, Optical, Electrical and Magnetic Properties of Sn_{0.9}Mn_{0.1}O_{2.8} Thin Films

Sushant Gupta¹, Fouran Singh² and B. Das¹

¹Department of Physics, University of Lucknow, Lucknow-226007, India.

²Inter-University Accelerator Centre, Aruna Asaf Ali Marg, New Delhi 110 067, India

Thin films of Sn_{0.9}Mn_{0.1}O_{2.8} were irradiated using a 15UD Pelletron accelerator at the Inter-University Accelerator Centre (IUAC), New Delhi. The irradiation was done in different batches using 120MeV Au⁹⁺ ions with fluences of 1×10¹¹, 3×10¹¹, 1×10¹², 3×10¹², 1×10¹³ and 3×10¹³ ions/cm². The electronic energy loss, S_e, nuclear energy loss, S_n and the projected range of ion, R_p, calculated by using standard SRIM simulation program, are 27.79 keV/nm, 0.4851 keV/nm and 8.33 μm, respectively. The threshold value of electronic energy loss (S_{eth}) for Sn_{0.9}Mn_{0.1}O_{2.8} was calculated according to Szenes' [1] thermal spike model and was found to be 31.97 keV/nm. In the present case, the S_e value is less than the threshold value S_{eth} required to produce columnar defects/tracks and we expect that only point defects or clusters of point defects will be produced in conducting Sn_{0.9}Mn_{0.1}O_{2.8} (n ≈ 2×10²⁰ cm⁻³) thin films. Efforts have also been made to calculate equilibrium substrate/film temperature during irradiation using the Nakata's [2] model and the calculated temperature (834 K) for the Sn_{0.9}Mn_{0.1}O_{2.8} matrix has been found to be quite higher than the crystallization temperature of tin oxide. The increase rate of the substrate/film temperature during irradiation has been determined also by the difference between the input power density and

the heat dissipation via radiation, divided by the heat capacity of the substrate (see Fig. 5.2.27). Through this it has been concluded that, in the case of high fluence, irradiation time is very much greater than the time taken to reach equilibrium temperature. So, almost for the entire time during irradiation, substrate/film remains at equilibrium temperature. Whereas, in the case of low fluence, irradiation time is less (or comparable) than, the time taken to reach equilibrium temperature. Therefore, in this case, almost for whole time during irradiation, substrate/film remains in 'low-temperature transient region' (see Fig. 5.2.27). The analysis of x-ray diffraction patterns (see Fig. 5.2.28) revealed that the pristine and irradiated films are pure crystalline tetragonal rutile phase of tin oxide which belongs to the space group P42/mnm (number 136). Measurement of resistivity, mobility, carrier density, and transmissivity to visible light as a function of ion fluence (1×10^{11} to 3×10^{13}) promulgates that increasing fluence results in degradation in electrical and optical properties of $\text{Sn}_{0.9}\text{Mn}_{0.1}\text{O}_{2-\delta}$. In this paper, the formation and the migration energies of all possible charged and neutral intrinsic defects ($\text{V}_{\text{Sn}}^{4-}$, Sn_i^{4+} , V_O^0 , O_i^{2-} , Sn_O^{4+} , $\text{O}_{\text{Sn}}^{2-}$, H_O^+) present in $\text{SnO}_{2-\delta}$ have been summarized and afterwards from the correlation between experimentally-observed and theoretically-calculated results, it has been concluded that the large amount of H_O^+ defects are present in pristine samples and concentration of these pre-existing H_O^+ defects is decreasing on increasing fluence value of irradiation. Because of this self-annealing, the conductivity of the irradiated samples has been greatly reduced in comparison to pristine samples (see Fig. 5.2.29). Along with this self-annealing, some fresh electron donor (Sn_O^{4+}) and electron-killer ($\text{V}_{\text{Sn}}^{4-}$, O_i^{2-} , $\text{O}_{\text{Sn}}^{2-}$) present in $\text{SnO}_{2-\delta}$ type defects are also being generated in the samples through irradiation. Because of all these mixed effects irradiated samples have small net conductivity, which becoming smaller along with the fluence rising up to 3×10^{12} ions/cm². Then again, the conductivity of the irradiated samples is greatly diminished for 1×10^{13} and 3×10^{13} ions/cm² fluence and samples have acquired the insulating state (see Fig. 5.2.29). Through electrical investigation it has also been found that the main doping mechanism reducing the intra-grain mobility of the electrons in pure $\text{SnO}_{2-\delta}$ films is the ionized impurity scattering. Ionized impurity scattering with singly ionized H_O^+ donor best describes the mobility of pure $\text{SnO}_{2-\delta}$ samples, which also supports our assumption of H_O^+ defects to act as shallow donors in the pure $\text{SnO}_{2-\delta}$ samples. The optical band gap (E_g) of the films has been determined from the spectral dependence of the absorption coefficient α by the application of conventional extrapolation [3] and Hamberg [4] methods. The present data have been analyzed by taking into account the narrowing, which is due to electron-electron and electron-impurity scattering, and the Burstein-Moss widening [3], which is due to the filled lower states in the conduction band. The magnetization measurements show ferromagnetic behavior at 300 K. Most interesting result of the paper is that after irradiation, columnar defects (tracks) have been observed in insulating ($R \approx 10$ M Ω /sq) whereas point defects in conducting ($R_s \approx 40$ Ω /sq) $\text{Sn}_{0.9}\text{Mn}_{0.1}\text{O}_{2-\delta}$ samples. In this paper the role of carrier concentration and mobility to create different types of defects (track/point) in $\text{Sn}_{0.9}\text{Mn}_{0.1}\text{O}_{2-\delta}$ samples has been discussed in detail.

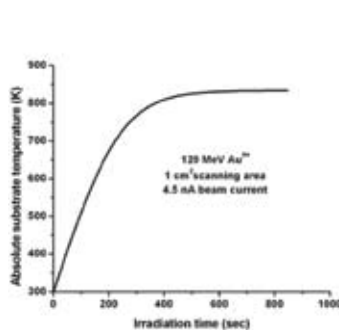


Figure 5.2.27: The transient substrate/film temperature.

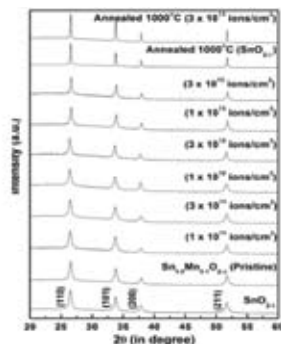


Figure 5.2.28: X-ray diffraction patterns of pristine and irradiated samples.

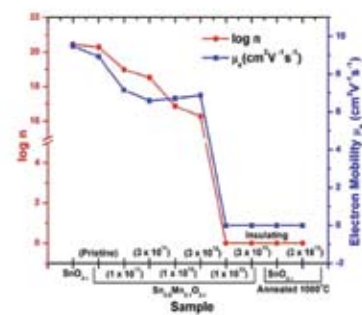


Figure 5.2.29: Changes in the carrier concentration (n) and electron mobility (μ_e) of respective samples.

REFERENCES

- [1] G. Szenes, Phys. Rev. B 51, 8026 (1995).
 [2] J. Nakata, Phys. Rev. B 43, 14643 (1991).
 [3] Sushant Gupta et. al., Material Research Bulletin 48, 3315 (2013)
 [4] I. Hamberg et. al., Phys. Rev. B 30, 3240 (1984).

5.2.19 Structural and Magnetic Properties of 100 MeV Ag^{7+} Ion Irradiated $\text{Ti}_{1-x}\text{Co}_x\text{O}_{2-\delta}$ Thin Films on LaAlO_3 substrate

P. Mohanty and Chandana Rath

School of Materials Science and Technology, Indian Institute of Technology (Banaras Hindu University) Varanasi-UP-221005, India

Discovery of room temperature ferromagnetism (RTFM) in Co-doped TiO_2 (CTO) thin films paved the way for the application of oxide-diluted magnetic semiconductors in the field of spintronics [1]. However, whether the origin of RTFM is due to the defects created by the dopants or the clusters of magnetic elements is still unclear. Nevertheless, it is widely accepted that the necessary defects such as oxygen vacancies can manipulate the magnetic properties in such oxide semiconductors [2]. Even undoped TiO_2 also demonstrate room temperature ferromagnetism due to oxygen vacancies [3]. In the previous study, we have explored the effect of 100 MeV Ag^{7+} ion irradiation on structural and magnetic properties of Co doped TiO_2 thin films grown on Si substrate [4]. For the polycrystalline Co doped TiO_2 film, we observed that the saturation magnetization decreases exponentially with ion fluence. We attribute this decrease in saturation magnetization as a consequence of the formation of magnetically disordered region surrounding the ion path. From the calculation, we observe the diameter of the magnetically disordered region to be higher than the track diameter [4].

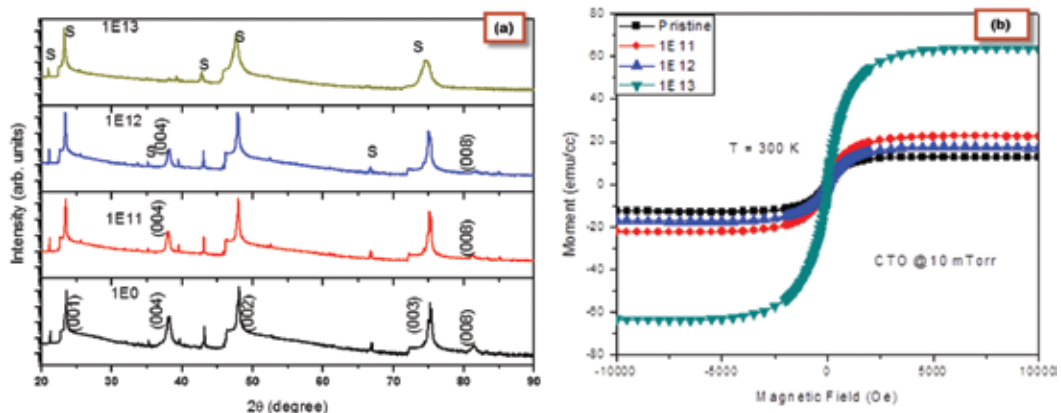


Figure 5.2.30: (a) XRD pattern of $\text{Ti}_{1-x}\text{Co}_x\text{O}_{2-\delta}$ ($x=0.05$) thin films deposited on LaAlO_3 substrate and irradiated with different fluence. (b) Magnetization as a function of applied magnetic field measured at 300 K.

To study the effect of ion irradiation on epitaxial thin films of $\text{Ti}_{1-x}\text{Co}_x\text{O}_{2-\delta}$, we have deposited the films on c-axis oriented LaAlO_3 substrate and they were irradiated with 100 MeV Ag^{7+} ions with fluence 1×10^{11} , 1×10^{12} and 1×10^{13} ions. cm^{-2} (For $S_e > S_{\text{eth}}$ energy regime) at IUAC, New Delhi. Fig. 5.2.30(a) shows the XRD pattern of Co doped TiO_2 thin film deposited at 10 mTorr oxygen

partial pressure. Besides the reflections from (004) and (008) planes, reflections from all other planes are suppressed suggesting epitaxial growth of the films. With increasing ion fluence, the peak corresponding to (004) and (008) are gradually suppressed. At a fluence of 1×10^{13} ions/cm², the film becomes completely amorphous. The diameter of the latent track calculated for these films is same for the polycrystalline films deposited on Si substrate. However, the magnetic properties demonstrate anomaly with ion fluence (see Fig. 5.2.30(b)). With a fluence of 1×10^{11} ions/cm², the saturation magnetization increases comparatively with ion dose. The observed magnetism in Co doped TiO₂ system has been explained on the basis of RKKY or bound magnetic polaron (BMP) model. RKKY is applicable for conducting films whereas BMP model is considered for insulating materials. The anomaly observed in the present case may be explained due to the competition of the RKKY and BMP models [5]. To get further insights, transport as well as magneto-transport measurements are essential.

REFERENCES

- [1] Matsumoto *et al. Science* **291** (2001) 854
- [2] Sundaresan *et al. Phys. Rev. B* **74** (2006) 161306R
- [3] Mohanty *et al. J. Magn. Magn. Mater* **355** (2014) 240.
- [4] Mohanty *et al. J. Phys D: Appl. Phys.* **47** (2014)315001
- [5] Mohanty *et al.* (to be communicated)

5.2.20 Effect of Swift Heavy Li³⁺ Ions Irradiation on Mn Doped ZnO Thin Films

H. A. Khawa¹, K. Asokan², S. Chopra², B. N. Dole^{1*}

¹Advanced Materials Research Laboratory, Department of Physics, Dr. Babasaheb Ambedkar Marathwada University, Aurangabad-431 004, India.

²Inter-University Accelerator Centre, Aruna Asaf Ali Marg, New Delhi 110 067, India

Thin films of Zn_{1-x}Mn_xO (x = 0.00, 0.01, 0.02, 0.03, 0.04 and 0.05) were synthesized using the successive ionic adsorption layer and reaction (SILAR) technique. The surface and structural modifications induced by Swift Heavy Ions irradiation on pure and Mn doped ZnO thin films were observed. Thin films were irradiated by swift heavy ions with fluence of 5×10^{11} ions/cm², 1×10^{12} ions/cm² and 5×10^{12} ions/cm². Pristine and Swift Heavy Ions irradiated thin films have been characterized by X-Ray Diffraction (XRD), Scanning Electron Microscopy (SEM) and Raman Spectroscopy.

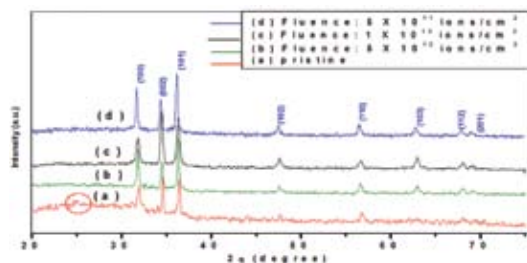


Figure 5.2.31: XRD patterns of Pristine and irradiated pure thin films.

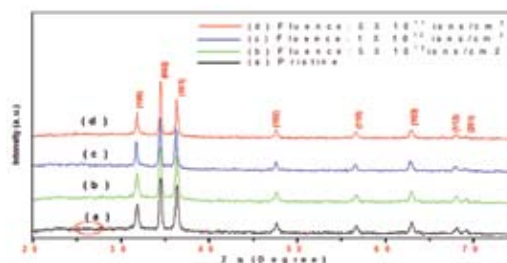


Figure 5.2.32: XRD pattern of Pristine and irradiated 3% Mn doped ZnO thin films.

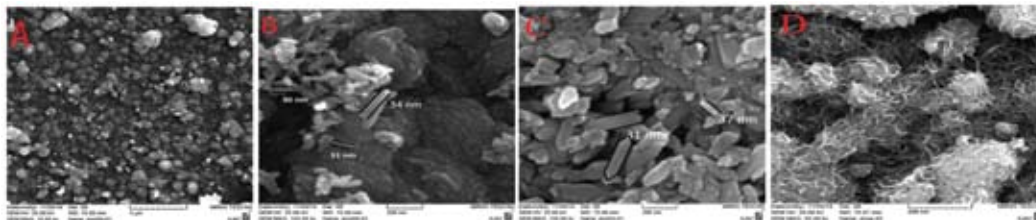


Figure 5.2.33: (a) SEM micrographs of the pristine pure ZnO thin films. (b) SEM images of the irradiated ZnO thin films. (c) SEM images of the 3% Mn doped ZnO thin films. (d) SEM images of 5 % Mn doped ZnO thin films.

The XRD peak revealed that all the samples exhibit hexagonal (wurtzite) structures [1-3]. Intensity of diffraction peaks increase for the films irradiated as compared to the pristine samples. Impurity peak disappeared just after irradiation on the samples as shown in figure 5.2.31&5.2.32. This indicates that the impurity phases were dissolved & samples become a plane phase as hexagonal structure. The Atomic Packing Fraction and Surface to volume ratio were calculated using XRD data. The values of lattice parameters increase with increasing Mn content as well as on enhancing fluences compared to the pure ZnO samples. The average crystallite size and X- Ray density of thin films were found to decrease on increasing the fluences and Mn concentration. It is due to the substitution effect of Mn in ZnO lattice and SHI irradiation on the samples. Surface morphology of samples was investigated by scanning electron microscopy (SEM). It was observed that pristine samples of ZnO thin film has spherical structures on the surface but for 3 % Mn doped ZnO thin films irradiated with 5×10^{12} ions/cm² fluence structures are rod-like. Nanowires like structure was found for 5 % Mn doped ZnO thin films[4-5]. The pristine ZnO sample appears as discontinuous having small spherical structure over the glass substrate as shown in figure 5.2.33(a,b,c,d). SEM images for 5×10^{12} ion/cm² irradiated samples clearly show rod like structure it is due to the electronic energy loss of the samples. SEM images for 3% and 5 % Mn concentration with fluence 5×10^{12} ion/cm² clearly reflect rod like and nanowires like structure as shown in figure 5.2.33 (c, d). It is due to the effect of fluences. Raman spectra of the Pristine and SHI irradiated samples show different phonon modes which reflects red shift. It was understood from Raman spectra that intensity goes on decreasing as Mn content increases it is owing to presence of oxygen content in the samples.

REFERENCES

- [1] N.S. Ridhuan, R. K. Abdul, Z. Lockman, A. A. Abdul PLoS ONE **7(11)** (2012) e50405.
- [2] V. D. Mote, B. N. Dole, Advanced Materials Research, Vol. **678**, (2013), 234-238.
- [3] V. D. Mote, J. S. Dargad, B. N. Dole, Nanoscience and Nanoengineering **1(2)**, (2013) 116-122.
- [4] S. K. Neogi, S Chattopadhyay, A. Banerjee, S. Bandyopadhyay, A. Sarkar and R. Kumar, J. Phys Condens. Matter **23** (2011) 205801.
- [5] S. Balamurali, R. Chandramohan, N. Suriyamurthy, P. Parameswaran, M. Karunakaran, V. Dhanasekaran, T. Mahalingam, J Mater Sci: Mater Electron, DOI 10.1007/s10854-012-1012-2.

5.2.21 Luminescence properties of sol-gel derived 100 MeV Si⁸⁺ ion bombarded pure and Nd³⁺ doped Y₂O₃ nanophosphor

N.J. Shivaramu¹, B.N. Lakshminarasappa¹, K.R. Nagabhushana², Fouran Singh³

¹Department of Physics, Jnanabharathi Campus, Bangalore University, Bangalore- 560 056, India

²Department of Physics, PES Institute of Technology, Bangalore-560085, India

³Inter-University Accelerator Centre, Aruna Asaf Ali Marg, New Delhi 110 067, India

Yttrium oxide (Y_2O_3) also known as yttria is an important material in many fields such as optics, optoelectronics, radiation dosimetry etc. It is a promising host for high performance composite material due to its high chemical durability and thermal stability. Thermoluminescence (TL) is a simple technique to obtain information on the nature of defects present in the solids. TL and optically stimulated luminescence (OSL) dosimeters have many advantages conventional dosimeters in radiotherapy with heavy charged particles (HCPs) and in space dosimetry. Heavy ion beam have been used for diagnostic and therapeutic purposes [1]. The treatment with highly energetic ion beams has several advantages in comparison with conventional irradiation with photons. Highly energetic cosmic rays have range of energies from keV to GeV and include light charged particles such as electrons and protons as well as HCPs. They constitute a serious dosimetric problem for air crew and space dosimetry. The high energy particle radiation present in the environment, where the components used in various subsystems of the air crew and space craft get exposed to such radiations. These are several ways of measuring doses of radiation. Presently, they are measured largely using thermoluminescent dosimeter (TLD) badges. There are several techniques to study TLD materials to understand their TL properties by ion beam irradiation [1]. Swift heavy ions (SHI) interacting with material loses its electronic energy and nuclear energy and cause intense electronic excitations along the ion trajectory that may result in defect clusters and/or ion tracks along the range. The defects created in the target materials depend on types of ions, energy, and fluences. Thus, it is quite interesting to know the effect of strong electronic excitation by energetic heavy ions in the surface region of materials

In the present work, nanoparticles of yttrium oxide (Y_2O_3) have been prepared by sol-gel method. The powder X-ray diffraction (PXRD) pattern of as synthesized sample showed the amorphous nature. The as synthesized Y_2O_3 powders are annealed at 900 °C for 2 hrs. Sol-gel synthesized Y_2O_3 irradiated with 120 MeV swift Ag^{9+} ion induces phase transformation from cubic to monoclinic phase at fluence of 1×10^{13} ions cm^{-2} and above. Phase transformation from cubic to monoclinic structure of yttrium oxide was observed with 100 MeV swift Si^{8+} and Ni^{7+} ions. XRD studies show that the structure of the ion irradiated Y_2O_3 and RE doped Y_2O_3 loses their crystallinity and was more in the case of the Ag^{9+} ion irradiated samples. Fourier transformed infrared spectroscopy (FTIR) revealed absorption with peaks at 3434, 1724, 1525, 1400, 847, 562 and 465 cm^{-1} . Photoluminescence (PL) of 100 MeV Si^{8+} ion irradiated samples shows emission with peaks at 417, 432, 465 nm as shown in Fig. 5.2.34. It is found that PL intensity increases with increasing in ion fluence up to 3×10^{12} ions cm^{-2} and then decreases with further increase in ion fluence. A well resolved thermoluminescence (TL) glow with peak at ~ 430 K (T_{m1}) and an unresolved ones with peaks at ~ 538 (T_{m2}) and 584 K (T_{m3}) are observed in ion irradiated samples[2].

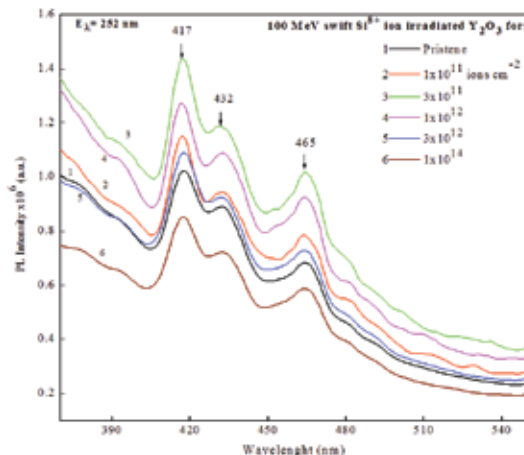


Figure 5.2.34: PL emission spectra of sol-gel synthesized 900°C heat treated 100 MeV Si^{8+} ion irradiated Y_2O_3 .

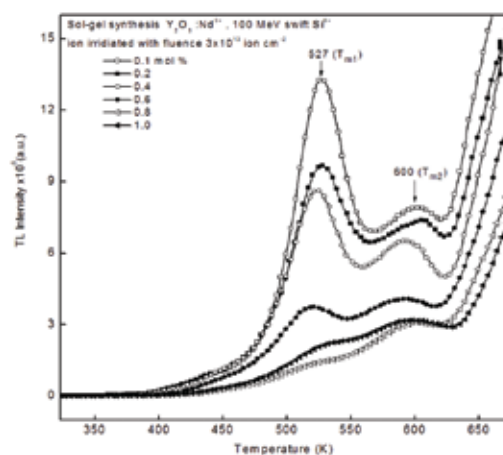


Figure 5.2.35: TL glow curves of 100 MeV Si^{8+} ion irradiated $Y_2O_3: Nd^{3+}$ for fluence of 3×10^{13} ions cm^{-2} .

Crystallites size of nanocrystalline Nd^{3+} doped Y_2O_3 was found to be in the range 28-30 nm. FTIR revealed Y-O, -OH stretching and C-O bending bonds. Pellets of $\text{Y}_2\text{O}_3:\text{Nd}^{3+}$ were irradiated with 100 MeV swift Si^{8+} ions for fluence in the range 3×10^{11} - 3×10^{13} ions cm^{-2} . A prominent TL glow with peak at 527 K and a weak one with peak at 600 K were observed as shown in Fig. 5.2.35. It indicates that SHI induces large number of deep level traps. The swift heavy ion creates oxygen vacancies and other structural lattice defects in the lattice [3]. The first glow peak intensity (T_{m1}) decreases with increasing ion fluence continuously while, the second TL glow peak intensity (T_{m2}) increases with increasing ion fluence up to $\sim 1 \times 10^{12}$ ions cm^{-2} and then decrease with further increasing ion fluence.

The relative TL efficiency of 100 MeV Si ion beam and γ -ray (^{60}Co) irradiated $\text{Y}_2\text{O}_3:\text{Nd}^{3+}$ is found to be 0.059. The TL kinetic parameters were calculated using Chen's peak shape method. It is observed from the present studies that $\text{Y}_2\text{O}_3:\text{Nd}^{3+}$ finds some uses in space dosimeter application.

REFERENCES

- [1] N. Salah et al., J. Phys. D: Appl. Phys. 41 (2008) 085408.
- [2] B.N. Lakshminarasappa, N.J. Shivaramu, K.R. Nagabhushana, Fouran Singh, Nucl. Instrum. and Meth. in Phys. Res. B 329 (2014) 40-47.
- [3] N.J. Shivaramu, B.N. Lakshminarasappa, K.R. Nagabhushana, Fouran Singh, J. of Alloy. Com. 637 (2015) 564-573.

5.2.22 Swift heavy ion induced modification on the structural, luminescence and optical studies of rare earth doped alkali-alkaline based oxide phosphors

Vinay Kumar and A. K. Bedyal

School of Physics, Shri Mata Vaishno Devi University, Katra-182320 (J&K) India

This research work is focused to study the effect of 120 MeV Ag^{9+} ion irradiation on the structural, optical and luminescence properties of the phosphors. The phosphors were synthesized by the conventional solid state method and combustion method. The synthesized material ($\text{NaSrBO}_3:\text{Sm}^{3+}$, $\text{NaSrBO}_3:\text{Dy}^{3+}$, $\text{SrAl}_2\text{O}_4:\text{Eu}^{2+}$, Dy^{3+}) were irradiated with 120 MeV Ag^{9+} SHIs at fluences in the range of 1×10^{12} ions cm^{-2} to 1×10^{13} ions cm^{-2} . The unirradiated as well as irradiated samples were characterized by powder X-ray diffraction (PXD), Diffuse Reflectance (DR) and PL techniques. PXD confirms no change in the phase of the phosphor after irradiation except loss of crystallinity, which may be due to the fragmentation caused by the SHI. A blue shift in the absorption band of the DR was observed, resulting in an increase in the band gap after ion irradiation. An increase in photoluminescence intensity was observed with increased ion fluences. In case of $\text{NaSrBO}_3:\text{Dy}^{3+}$, the ratio of the blue to yellow emission peaks (I_{483}/I_{577}) was calculated and found to be varying with ion fluences suggesting that the white light can be achieved by tailoring this yellow to blue ratio. The CIE coordinates were found to move toward the white region after irradiation for $\text{NaSrBO}_3:\text{Dy}^{3+}$ [1].

For Sm^{3+} doped NaSrBO_3 phosphor, comparative study among the different synthesis techniques before and after irradiation had been done. DR spectra reflect a blue shift in the absorption band with increasing fluences, for phosphors prepared using both solid state reaction and combustion method, resulting in an increase in the band gap from 5.64 to 6.06 eV. The PL intensity of the phosphors was enhanced with an increase in ion fluences, with the samples prepared using combustion method exhibiting prominent intensity. The CIE coordinates of the phosphor represent the orange-red

to a highly symmetric crystallographic structure (austenite) upon heating and a reverse martensitic transformation in the opposite direction upon cooling [2]. Thin films of Ni-Ti shape memory alloy are deposited on Si substrate by using Magnetron co-sputtering technique. These prepared thin films were irradiated by 120 MeV Au ions provided by the 15 UD Pelletron accelerator at Inter University Accelerator Centre (IUAC), New Delhi. The vacuum in the chamber during the irradiation was $\sim 7 \times 10^{-7}$ torr. Ion fluence was varied from 1×10^{12} to 3×10^{13} ions/cm².

The orientation and crystallinity of as deposited and irradiated films were studied using a standard x-ray diffractometer (Bruker D8 Advance) equipped with Cu K α x-rays source in θ - 2θ geometry at a scan speed of 0.6°/min. The film thickness and composition was measured using Rutherford backscattering spectrometry measurement. XRD spectra (Fig. 5.2.36) revealed that both the phase martensitic as well as austenitic phase exists in pristine sample and the intensity of the peak is decreased with increasing ions fluences. The RBS spectrum (Fig. 5.2.37) was simulated by using the SIMNRA. The thickness was found to be ~ 270 nm and Ni atomic fraction was calculated 56.7 at. % of Ti atoms. AFM micrograph shows that the grain size decreases with increasing ion fluence.

REFERENCES

- [1] Miyazaki S. et al., Thin film shape memory alloys: fundamental and device application. Cambridge University Press (2009)
- [2] Chang L. C. and Read T. A., Trans. AIME, 47 (1951), 189.

5.2.24 100 MeV induced SHI irradiation phase transformation in CdS_{1-x}Se_x thin films

Deepak S. Upadhye^{1,2}, Fouran Singh³ and Ramphal Sharma^{1,2*}

¹Department of Nanotechnology, Dr. Babasaheb Ambedkar Marathwada University, Aurangabad-431004, India.

²Thin Film and Nanotechnology Laboratory, Department of Physics, Dr. Babasaheb Ambedkar Marathwada University, Aurangabad-431004, India.

³Inter-University Accelerator Centre, Aruna Asaf Ali Marg, New Delhi-110067, India.

The Cadmium Sulphoselenide is one of the important semiconducting chalcogenide materials and varies its electrical properties by tailoring the energy band [1]. It has wide range of applications in photovoltaics, optoelectronics, solid state devices etc [2]. Many of techniques such as vacuum evaporation, electrochemical deposition, spray pyrolysis, are available to synthesis CdS_{1-x}Se_x thin films. In present work we have prepared the ternary CdS_{1-x}Se_x alloy by Chemical Bath Deposition technique on glass

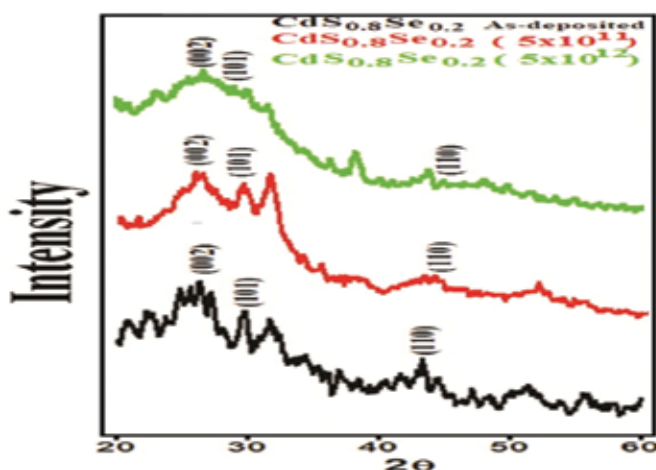


Figure 5.2.38: (a) XRD spectra of pristine and irradiated CdS_{1-x}Se_x by 100 MeV Au⁺⁹ with 5×10^{11} ions/cm² and 5×10^{12} ions/cm²

due its simplicity and cost effectiveness and these samples were irradiated by Au⁺ ions having energy 100 MeV at IUAC, New Delhi.

Fig. 5.2.38(a) indicates XRD spectra of Pristine and irradiated CdS_{1-x}Se_x thin films. In above figure three well defined diffraction peaks along lattice plane (002), (101) and (110) were observed having hexagonal symmetry for pristine and irradiated CdS_{1-x}Se_x samples. From fig. 5.2.38(a), it is observed that peak intensity decreased with increase in ion fluence and peak FWHM increased and decrease in crystallinity for fluence 5×10^{11} ions/cm² and observed peaks disappeared for the fluence 5×10^{12} ions/cm² due to phase transformation from polycrystalline to amorphous phase. So, we may conclude that SHI irradiation technique can be used to tailor material properties in controlled manner.

REFERENCES

- [1] Alaa A.Akl and A.S.Hassanien., Microstructure and crystal imperfections of nanosized CdS_xSe_{1-x} thermally evaporated thin film, in superlattice and microstructure. 2015. p. 67-81.
- [2] Vipin Kumar and D.K. Dwivedi., Optik, 2013. 124: p. 2345-2348.

5.2.25 Characterization of PZT thin films using SPM and NSOM Measurements

J. Kumar¹, R.Mohankumar¹, N.Syed Kaleemullah¹, K. Asokan², D.Kanjilal²

¹Crystal Growth Centre, Anna University, Chennai, India

²Inter-University Accelerator Centre, Aruna Asaf Ali Marg, New Delhi 110 067, India

Perovskite structured ferroelectric thin films have been of great interest for many years for their applications in electronic devices, such as non-volatile memories, infrared sensors, optical shutters, electro-optic device modulators, actuators, multilayered capacitors (MLCs), etc. Lead-Zirconium-Titanium Oxide (PbZr_{1-x}Ti_xO₃ or PZT) is considered as one of the most important polar piezoelectrics due to its high bulk piezoelectric properties (e.g., longitudinal piezoelectric coefficient $d_{33} = 300\text{--}600$ pC/N) depending on the specific composition. Near-field Scanning Optical Microscopy (NSOM) overcomes the principal diffraction limit in conventional light microscopy and belongs to the family of scanning probe microscopes (SPM). It provides simultaneously an optical and topographical image of the surface of a sample. PFM (Piezo Force Microscopy) is a spectral SPM mode enables to measure the piezo response of the sample to the applied voltage with high lateral resolution. SHI irradiation works were done on PZT thin films with Ni, N and Ag ions at a fluence of 1×10^{12} , 6×10^{12} and 5×10^{12} respectively. The irradiated samples were characterised using techniques such as AFM, PFM, SEM and Raman analysis (Fig. 5.2.39 and Fig. 5.2.40).

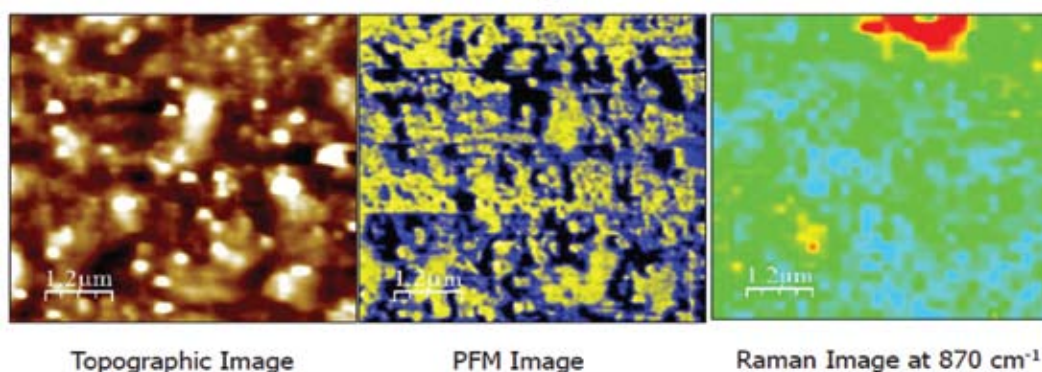


Figure 5.2.39: AFM/PFM/Raman measurements of Pristine PZT thin films

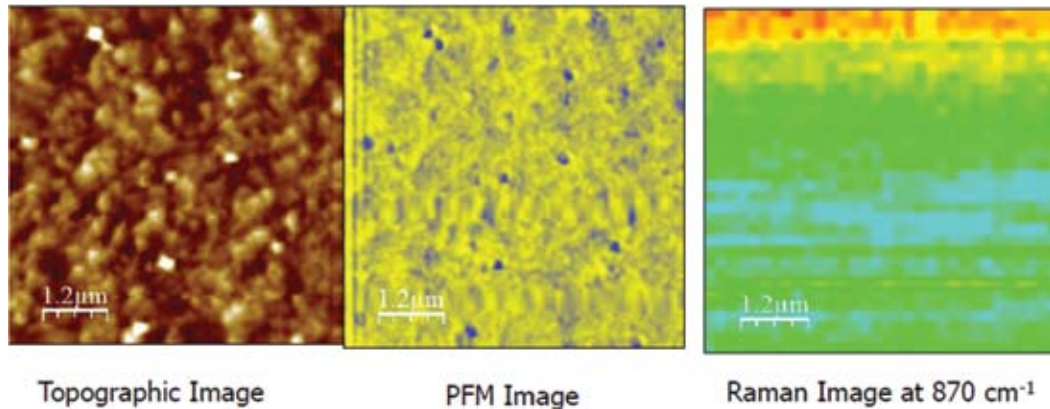


Figure 5.2.40: AFM/PFM/Raman measurements of Ag ions (5×10^{12} ions/cm²) irradiated on PZT thin films

Topographic image shows the height variations. Bright colors correspond to the high topographic features; dark colors correspond to the low topography. PFM Image shows the piezoelectric response of the sample. In order to know the actual orientation of as grown films, the regions were scanned with positive and negative voltages of about 8V. During the scanning the phase of the oscillations were acquired. The phase is proportional to the domain polarization. Films of pure PZT grown on Si substrate showed upward polarization corresponding bright yellow colors, while the dark blue regions corresponds to the polarization pointed down.

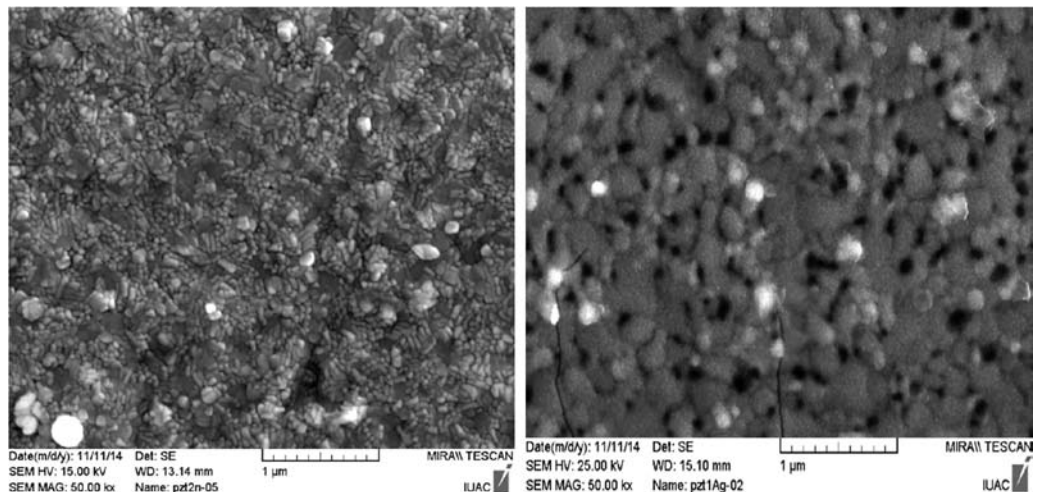


Figure 5.2.41: SEM images (left) of Pristine PZT and (right) Ag ions irradiated PZT samples.

The SEM micrograph (Fig. 5.2.41) clearly reveals the surface morphology of the PZT layer. However, the interface between Si and PZT is smooth with no trace of any inter-diffusion in case of pristine sample. The irradiated sample shows cracks and it is rough due to the lattice deformation caused by the irradiated ions.

REFERENCES

- [1] S.K. Pandey, A.R. James, Chandra Prakash, T.C. Goel, K. Zimik, *Materials Science & Engineering B* 112 (2004) 96–100.
- [2] P. Verardi, F. Craciun, M. Dinescu, 1997 IEEE ULTRASONICS SYMPOSIUM –569
- [3] Zhenxing Bi, Zhisheng Zhang and Panfeng Fan, *International Conference on Nanoscience and Technology (ICN&T 2006)*.
- [4] Yi Yanga, Kyekyoon Kim, Hyungsoo Choi, *Thin Solid Films* 396 (2001) 97–102.
- [5] Mahamudu Mtebwa, Ludwig Feigl, Nava Setter, 2013 Joint UFFC, EFTF and PFM Symposium.

5.2.26 Surface modification of PVA containing Zn incorporated HAp coatings on titanium by Gold ion irradiation

K.R. Karthikeyan¹, K.Thanigaiaru¹, J. Ramana Ramya¹, K. Asokan², D. Kanjilal², S. Narayana Kalkura¹

¹Crystal Growth Centre, Anna University, Chennai – 600025, India

²Inter-University Accelerator Centre, Aruna Asaf Ali Marg, New Delhi – 110067, India

Hydroxyapatite (HAp, $(Ca_{10})(PO_4)_6(OH)_2$) is the main inorganic constituent of bone and teeth. Bulk form of HAp cannot be used as implant to replace large bone defects due to its poor mechanical strength. HAp coated on titanium substrates is used for load bearing application (orthopaedic and dental implants). The surface properties of implants, such as surface roughness, electrical charge and wettability [1] play an important role in binding of the living cells [2]. Swift heavy ion irradiation provides selective surface modification without affecting the bulk properties of the materials. Here, the surface modification of polyvinyl alcohol–zinc-HAp (PVA-Zn-HAp) nanocomposite coatings method by Au ion irradiation is attempted.

The XRD patterns of pristine and Au ion irradiated PVA-HAp nanocomposite coatings (Fig. 5.2.42(1)) contains all major phases of HAp, in good agreement with JCPDS data (card number 09-0432). On Au ion irradiation, the crystallite size was reduced by 40%, which may be due to the formation of defects and localized heating of the samples. However, at lower fluence, lattice parameter (c) decreased compared to the other samples due to the stress created by Au ions. There was no significant variation in the lattice parameter of the samples on irradiation.

The PL spectra of the samples were shown in the fig. 5.2.42(2). The samples were excited at 244 nm and the emission was at about 300 nm to 600 nm. There was an enhanced PL intensity at low ion fluence. The enhancement in PL intensity of 1×10^{11} ions/cm² could be due to the ion irradiation and radiative recombination of electron/hole pair. Whereas, it was reduced in the case of 1×10^{12} ions/cm² and 1×10^{13} ions/cm² due to non-radiative recombination of the electron / hole pair. The ion irradiated samples could assist in the fabrication of a biosensor for monitoring in situ bone growth [3]. The study of the biological properties of the irradiated samples is under progress.

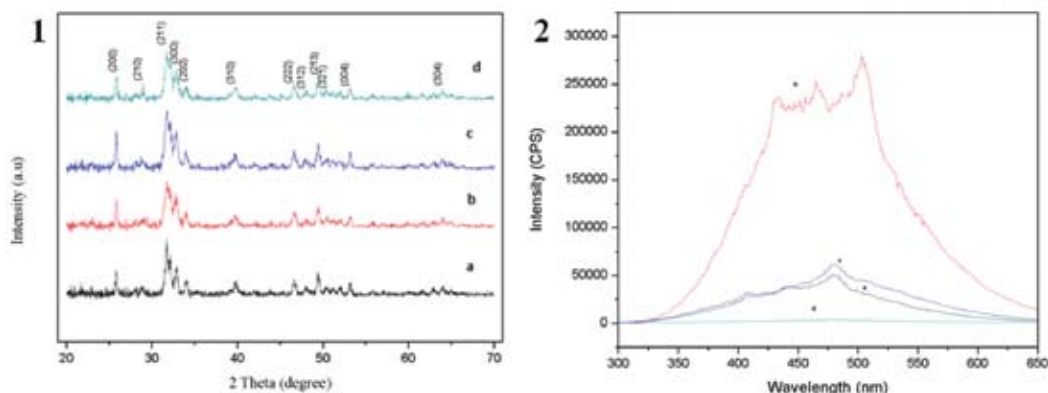


Figure 5.2.42: (1) XRD patterns of (a) Pristine, (b) 1×10^{11} ions/cm², (c) 1×10^{12} ions/cm² and (d) 1×10^{13} ions/cm². (2) PL spectra of (a) Pristine, (b) 1×10^{11} ions/cm², (c) 1×10^{12} ions/cm² and (d) 1×10^{13} ions/cm²

REFERENCES

- [1] Waugh D G and Lawrence J. 2011. Applied Surface Science, 257, 8798-8812
 [2] Shanthini G M et al. 2015. Applied Surface Science, 329, 116-126.
 [3] Thanigaiarul K et al. 2013. Ceramics International, 39, 3027-3034.

5.2.27 Effect of low energy ion irradiation on the transport and structural behaviour of organic hole conductors

Kumaraswamy GN¹, Damle R², Pravin Kumar³, Kanjilal D³

¹Department of Physics, Amrita Vishwa Vidyapeetham, Bengaluru – 560 035

²Department of Physics, Bangalore University, Jnanabharathi, Bengaluru – 560 056

³Inter University Accelerator Centre, Aruna Asaf Ali Marg, New Delhi – 110 067

Organic conductors have attracted considerable interest due to their electrical conductivity, chemical stability, processability and transparency properties. They are widely used in organic devices, including small-molecule OLEDs, PLEDs, and OPV devices. The PEDOT:PSS is one such polymer which is extensively used as an integral part in many devices [1,2]. The PEDOT:PSS suffers with low conductivity (<1 S/cm) due to the presence of PSS, limiting its application. In the present work, TiO₂ inorganic nanoparticles have been incorporated into PEDOT:PSS matrix with an aim to improve the conductivity. This polymer being an integral part of OPVs, is likely to be exposed to the radiation environment. Hence, we have presented the studies on radiation damage and radiation tolerance of PEDOT:PSS.

The pure sample recorded a conductivity of 0.8 S/cm. The nanocomposite systems showed enhanced conductivity. The sample with 7.5 wt.% of TiO₂ showed highest conductivity of 48 S/cm. These nanocomposites along with pure samples were subjected to O⁺ ion irradiation.

The variation in electrical conductivity in pure PEDOT:PSS and PEDOT:PSS/TiO₂ nanocomposites as function of ion fluency is tabulated in Table 5.2.3. The conductivity of PEDOT:PSS shows a continuous decrease as function of fluency when subjected to ion irradiation severely restricting its usage in any form as conducting medium. The reason might be the scission of PEDOT chains and thus increase in amorphous phase restricting the tunnelling of holes from one conjugate point to another. The nanocomposites show a similar trend of reduction in conductivity as function of increase in ion fluency. However, the amount of reduction is quite low compared to the pure PEDOT:PSS. The XRD patterns represented in figure 5.2.43(a) clearly show that, the amorphous region in PEDOT:PSS increases when exposed to ion irradiation. The figure

Table -5.2.3

Sample	Fluency (ions/cm ²)	Conductivity (S/cm)
PEDOT:PSS	Un-irr	0.8
	1×10 ¹²	0.2
	0.5×10 ¹³	0.13
	1×10 ¹³	0.06
	0.5×10 ¹⁴	0.02
	1×10 ¹⁴	0.01
PEDOT:PSS/TiO ₂	Un-irr	48
	1×10 ¹²	37
	0.5×10 ¹³	33
	1×10 ¹³	30
	0.5×10 ¹⁴	29
	1×10 ¹⁴	26

5.2.43(b) represents the XRD plot of PEDOT/PSS nanocomposites, which indicates that the chain scission is not prominent as in the earlier case, may be due to the presence of TiO_2 nanoparticles. Hence, we may conclude that, the degradation of PEDOT:PSS to ion beam is controlled in the presence of TiO_2 nanoparticles in the system.

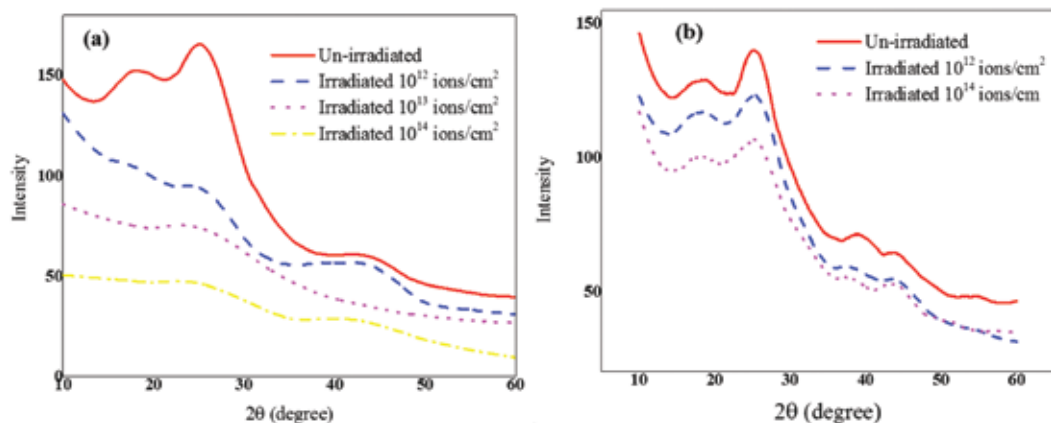


Figure 5.2.43: XRD graphs of (a) PEDOT:PSS and (b) PEDOT:PSS/ TiO_2 irradiated at different fluences

REFERENCES

- [1] TW Koh, JM Choi, S Lee, S Yoo; *Adv. Mater.* **22** (2010) 1849
 [2] J Kawahara, PA Ersman, I Engquist, M Berggren; *Org. Electron.* **13** (2012) 469

5.2.28 Ion Irradiation Induced modifications of P3HT Polymer

Trupti Sharma¹, R. Singhal¹, R. Vishnoi², G. B. V. S. Lakshmi³, S. Chand⁴, S. K. Biswas⁵, and D. K. Avasthi³

¹Department of Physics and Materials Research Centre, Malaviya National Institute of Technology, Jaipur-302017, India

²Department of Physics, Vardhman Degree College, Bijnor- 246701, India

³Inter-University Accelerator Centre, Aruna Asaf Ali Marg, New Delhi 110 067, India

⁴National Physical Laboratory, New Delhi 110012, India

⁵Department of Metallurgical and Materials Engineering, Malaviya National Institute of Technology, Jaipur-302017, India

Poly (3-hexylthiophene) (P3HT) is a conducting polymer which consists of a π -conjugated backbone with polythiophene units and pendent alkyl side group. It has a band gap of about 1.9 eV and mobility 0.1 cm^2/Vs . This conducting polymer can be used in flexible optoelectronic devices such as field effect transistor, organic photovoltaic devices, organic light emitting diode etc. Using high energy ion beam irradiation technique chemical, structural, optical etc. properties can be modified in a controlled manner. P3HT thin films deposited on different substrate such as double side polished Silicon, glass and ITO coated glass with thickness ~ 300 nm were irradiated by 90 MeV Ni^{+7} ion beam with current 0.2 pA. The nuclear and electronic energy loss of 90 MeV Ni ions in P3HT is 0.839 $\text{eV}/\text{\AA}$ and 4.78×10^2 $\text{eV}/\text{\AA}$. The fluences for irradiation was from 1×10^9 ions/ cm^2 to 1×10^{11} ions/ cm^2 . The pristine and irradiated thin films have been characterized by UV-visible spectroscopy,

Raman spectroscopy and AFM analysis. The enhancement in the vibrational mode corresponding to the C=C mode in P3HT Raman spectra (Fig. 5.2.44) shows ordering mechanism takes place at low fluences. The narrower FWHM and enhanced relative intensity corresponding to C-C mode to C=C mode ($I_{c-c} / I_{c=c}$) also supports the ordering results. The lamellar structure of P3HT remains undamaged during high energy irradiation as confirmed by UV-visible spectra (Fig. 5.2.45). A marginal change was observed in the optical band gap after irradiation. The decrease in roughness is observed with increasing fluence which was analysed by AFM. The ordering in P3HT films is due to heating effect created in halo regions of ion paths upto fluence 1×10^{10} ions/cm². At higher fluence disordering was observed due to the overlapping of ion paths. The enhanced ordering may enhance electrical properties, mobility, etc. which can be used in photovoltaic devices.

REFERENCES

- [1] A. Dhillon, A. Kaur, D.K. Avasthi, Thin Solid Films, 519 (2010) 998-1002.
 [2] G.B.V.S. Lakshmi, Azher M. Siddiquia and M. Zulfeqar, Radiation Effects & Defects in Solids, 166 (2011) 427-434.

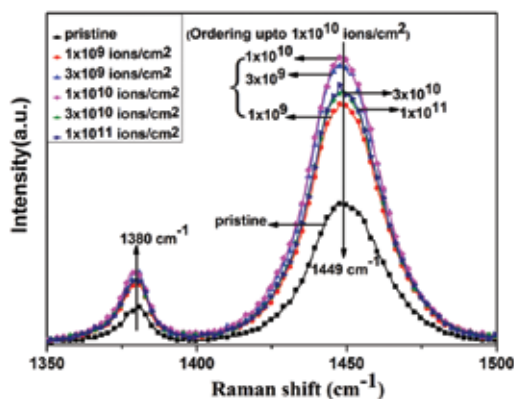


Figure 5.2.44: Raman spectra

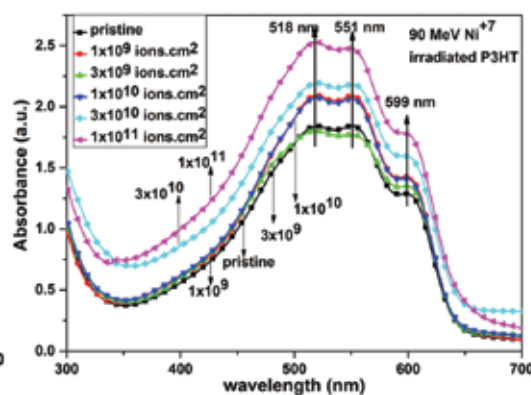


Figure 5.2.45: UV-visible spectra

5.2.29 Heavy Ion Irradiation study in SS316

Aniruddha Biswas¹, Sarita¹, Sudip Kumar Sarkar¹, Manju Bala², Compesh Pannu², Debdulal Kabiraj²

¹Glass and Advanced Materials Division, Bhabha Atomic Research Centre, Mumbai - 400085, India

²Inter-University Accelerator Centre, Aruna Asaf Ali Marg, New Delhi- 110067, India

SS316 is mainly used in internal structure of Pressurized water reactor (PWR) which is located close to reactor core, and hence, are exposed to high neutron dose [1,2]. This high irradiation results in degradation of mechanical properties which are directly correlated with the microstructural evolution. Therefore, it is important to study the changes in microstructure under irradiation to determine the life time of internal parts [3]. With this objective, we prepared three different types of samples: (i) TEM samples by jet polishing (ii) Atom probe pins by two stage electro-polishing (iii) Flat plate samples (1 cm×1 cm) of thickness around 0.4 mm polished from one side. To simulate the effect in the way it occurs in the reactor core, all these samples were irradiated using Pelletron facility available in IUAC Delhi. For the exploratory study of irradiation, two different beams namely, (i) Ag⁹⁺ (120 MeV) and (ii) Au(100 MeV) were used. Samples were irradiated for three different fluences (1×10^{13} , 5×10^{13} , 1×10^{14} ions/cm²) for each beam for comparative study. Damage produced by both the beams is simulated using TRIM software. To analyse the microstructure,

optical microscopy has been carried out for SS316 and microstructure is as shown in fig. 5.2.46(a). This result gives information about the grain size which is of the order of a few microns. SANS experiments have already been carried out for all the ion-damaged samples in ILL, Grenoble, France. A detector distance of 2 m has been used in ILL to cover the entire range of interest. SANS plots for Au and Ag ion irradiated samples are shown in fig. 5.2.46(b & c). For both the ion beams, it has been observed that there is some variation in slope of the curves as well as in intensity for different fluences, which can be directly correlated with the evolution of features in the sample. Detailed structural analysis using a combination of 3DAP, TEM and SAS is underway.

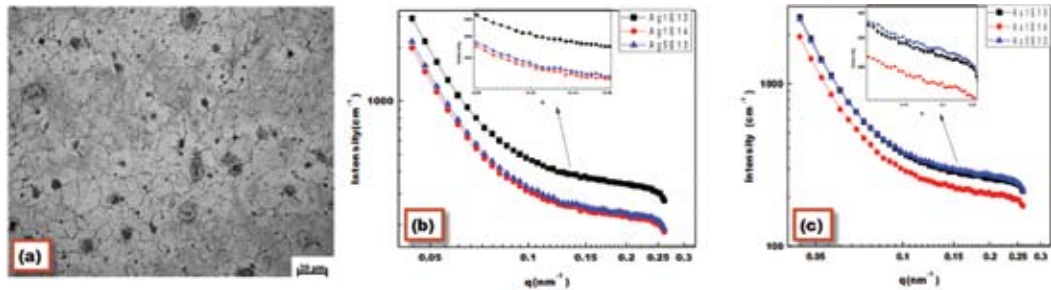


Figure 5.2.46: (a) Optical Micrograph, (b) and (c) SANS plots for samples irradiated by Ag and Au ions

REFERENCES

- [1] T. Toyama et al., J. of Nuclear Materials 418 (2011) 62–68
- [2] A. Etienne, B. Radiguet, N.J. Cunningham, G.R. Odette, R. Valiev, P. Pareige, Ultramicroscopy 111 (2011) 659–663
- [3] A. Etienne, B. Radiguet, P. Pareige, J.-P. Massoud, C. Pokor, J. of Nuclear Materials 382 (2008) 64–69

5.2.30 Structural evolution in III-V semiconductors by high energy ion irradiation

Shramana Mishra

Department of Physics, Indian Institute of Technology, Kharagpur. Pin 721302

Group III-V semiconductors, like GaAs and InP, have direct band gap and hence are smart choices for the development and fabrication of various optoelectronic devices. As ion irradiation is an established technique to tune various physical properties (e.g. mechanical, optical, etc) of a system. It is important to know how the crystal structure of a material evolves by this device processing approach. Here we focus on the structural evolution in above mentioned semiconductors, GaAs and InP, by high energy ion irradiation.

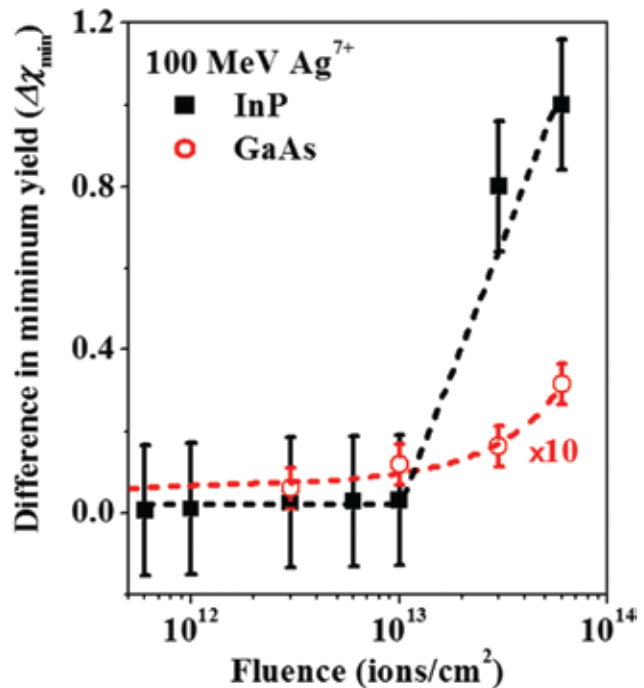


Figure 5.2.47: shows the evolution of the difference in minimum yield ($\Delta\chi_{\min}$) with fluence

As the energy of the ion beam, the mass of the ions used in the beam and the beam fluence play important roles in determining the changes in the structural properties of a target material, we have subjected the targets to both light (50 MeV lithium (Li^{3+})) and heavy (100 MeV silver (Ag^{7+})) ions of different fluences. Fig. 5.2.47 shows the evolution of the difference in minimum yield ($\Delta\chi_{\text{min}}$) with fluence as observed from Rutherford back-scattering ion channeling (c-RBS) measurements, for 100 MeV Ag^{7+} ion irradiated SI-GaAs and SI-InP. It is to be noted that, for 50 MeV Li^{3+} ion irradiated SI-GaAs and chromium doped GaAs (GaAs:Cr), no detectable structural damage was observed from c-RBS measurements.

The Table 5.2.4 summarizes the effect of high energy light ion (HELI) and swift heavy ion (SHI) irradiation on the damage evolution of these target materials, as emerged from our studies based on c-RBS and Raman scattering measurements. The role of the characteristics of the target materials in determining the extent of defect formation by high energy ions could be revealed when we compared 50 MeV Li^{3+} ion irradiated SI-GaAs and GaAs:Cr or 100 MeV Ag^{7+} ion irradiated SI-GaAs and SI-InP. The table also includes the values of the electronic and nuclear energy losses (ϵ_e and ϵ_n , respectively) of the ions in the respective targets. We have shown that these energy losses mostly determine the damage evolution in the target on irradiation.

Table 5.2.4

		Energy loss (keV/nm)		
Target	Ions and Fluence (ions/cm ²)	Electronic (ϵ_e)	Nuclear (ϵ_n)	Lattice damage [fluence (ions/cm ²)]
SI-GaAs (001)	50 MeV lithium (Li^{3+}) (HELI) Fluence: 1×10^{12} - 1×10^{14}	0.16	8.0×10^{-5}	Lattice disorder only in the high fluence regime: 3×10^{13} - 1×10^{14}
GaAs:Cr (001)	50 MeV lithium (Li^{3+}) (HELI) Fluence: 5×10^{11} - 1×10^{14}	0.16	8.0×10^{-5}	No large scale structural changes. Only change in medium range ordering in the structure.
SI-GaAs (001)	100 MeV silver (Ag^{7+}) (SHI) Fluence: 6×10^{11} - 6×10^{13}	16.0	0.11	Monotonic increase in lattice disorder. Fluence range for significant damage /disorder : 1×10^{13} - 6×10^{13} Observation of sub-surface lattice strain
SI-InP (001)	100 MeV silver (Ag^{7+}) (SHI) Fluence: 6×10^{11} - 6×10^{13}	13.5	0.09	Continuous increase in lattice disorder. Formation of heavily damaged zones in high fluence (6×10^{13} ions/cm ²). Fluence range for significant damage /disorder : 1×10^{13} - 6×10^{13} Observation of sub-surface lattice strain

In addition to the above findings on damage formation in the irradiated targets, we would like to highlight a couple of other important points, which we have addressed—

The extent or scale of amorphization by high energy ion irradiation in a target material demands a special attention. In general, the structure of tetrahedrally coordinated amorphous semiconductors is interpreted by a continuous random network (CRN) of the host atoms. An additional amorphous structure also exists with a specific medium range ordering (MRO) of atoms in a crystal. We have demonstrated that Raman spectroscopy can be used to study the MRO of the atoms in the high energy ion irradiated GaAs. The same technique has been exploited to study the fractal characteristics of this MRO related structure. It is important to note that it is non-trivial to visualize such MRO in the structure of a crystal directly, either by high-resolution transmission electron microscopy or by atomic force microscopy. Thus, the above mentioned studies indicate a scope of studying low level amorphization in various targets at the microscopic scale, by Raman spectroscopy.

Thermal spike model (TSM) has been extensively used in the literature to understand damage evolution and the formation of amorphous tracks in numerous targets. We have developed a three dimensional (3D) unified TSM to study the lattice temperature evolution and the structural modification of semiconductors on ion irradiation. Our model includes both inelastic thermal spike (effect of ε_e) and elastic collision spike (effect of ε_n) along with the effect of latent heat. The validity of the model has been established by explaining the measured structural damage in InP, as obtained from the literature. We have demonstrated that this model is crucial in the sub-threshold regime of a stable track formation, where ε_n plays an important role in the structural modification of the target. The model provides the dynamics of phase transition during irradiation which is difficult to obtain experimentally. From the proposed 3D simulation, we obtain the depth of the damaged layers in the target. It is to be noted that, when on irradiation, a stable amorphous track does not form in the target; it is non-trivial to measure the depth of the damaged zone. We believe that our model can be effectively used to study the amorphization in ion irradiated targets when ε_e and ε_n are comparable.

In summary, we have tried to carry out a comprehensive study, addressing the structural evolution in GaAs and InP by irradiated ions of different mass, energy and fluence.

5.2.31 Electric and Dielectric Characteristics of Ni/*n*-GaAs Schottky Diode under Swift Heavy Ion Irradiation

A Bobby¹, N Shiwakoti¹, P M Sarun¹, S Verma², K Asokan² and B K Antony¹

¹Department of Applied Physics, Indian School of Mines, Dhanbad – 826004, India.

²Inter-University Accelerator Center, Aruna Asaf Ali Marg, New Delhi – 110067, India.

Rectifying metal-semiconductor (MS) contacts viz. Schottky barrier diodes (SBDs) finds applications in environments such as space, nuclear reactor, nuclear and particle detectors etc, [1]. However, the device under such harsh conditions can introduce large amount of S_e loss mainly in the interface, which drastically modifies the device properties [2, 3]. Inorder to have a comprehensive study on irradiation induced electric and dielectric properties, the Ni/*n*-GaAs Schottky barrier diode (SBD) were subjected to 25 MeV C⁴⁺SHI irradiation in the fluence range of 5×10^{10} - 5×10^{13} ions/cm² at the 15 UD Pelletron accelerator facility, IUAC, New Delhi.

The ideality factor (n) and barrier height (BH) were found to change with irradiation fluence. The respective n and BH values were found to be 1.92 and 1.37 eV for pristine. After an irradiation dose of 5×10^{13} ions- cm^{-2} , the values were increased to 2.83 and 1.64 eV respectively. However, the values of charge density N_D for the pristine diode which was of the order of 10^{16} , were decreased to 10^{14} after the final fluence of 5×10^{13} ions- cm^{-2} . The investigation also shows reduction in capacitance (Fig. 5.2.48) implying widening of the depletion width resulting from the reduction of charge carrier concentration. This in turn is related to the generation of swift heavy ion induced acceptor trap centers at the interface due to electronic energy loss mechanism. Subsequent changes were observed in parameters such as conductance/dielectric constant, dielectric loss, tangent loss and electric modulus parameters. The parameters also displays dispersion/relaxation peaks, which are related to the polarization and relaxation mechanisms of defects formed during irradiation [4]. The frequency dependent study show decrease in capacitance with increase in ion fluence at low frequencies (Fig 5.2.49). Interestingly, a negative capacitance effect was also observed in this frequency range in all the samples. At high frequencies, the capacitance reaches the geometric value ' C_0 '. The results were interpreted in terms of the generation of irradiation induced traps, carrier capture and emission from deep and shallow states and its frequency dependent saturation effects [5].

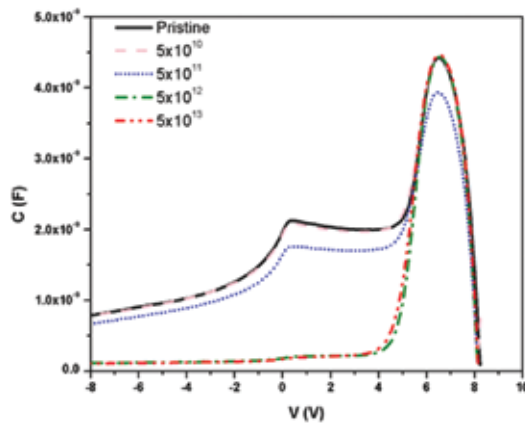


Figure 5.2.48: The variations of capacitance with applied voltage of Ni/n-GaAs Schottky diode at various fluences.

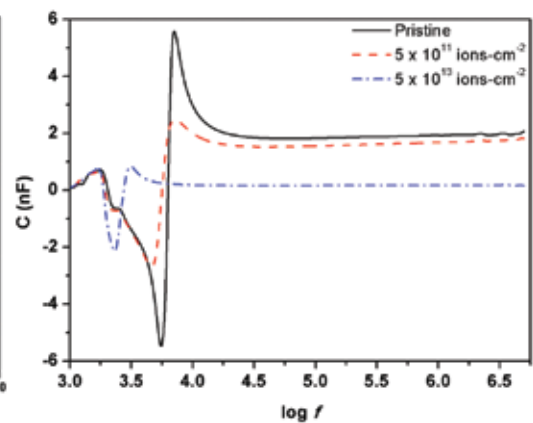


Figure 5.2.49: The frequency dependent capacitance plot of Ni/n-GaAs Schottky diode at various fluence. The frequency independent capacitance in the higher frequency range corresponds to the geometric capacitance C_0 with the respective fluence.

REFERENCES

- [1] Reliability Characterisation of Electrical and Electronic Systems by TMI Bajenescu and M I Bazu p-73 edited by Jonathan Swingler, Woodhead Publishing, UK, 2015.
- [2] A T Sharma, S Kumar, Y S Katharria, and D Kanjilal, Appl. Surf. Sci., 254 (2007) 459.
- [3] A Bobby, N Shiwakoti, S Verma, P S Gupta and B K Antony, Mater. Sci. Semicond. Process. 21 (2014) 116.
- [4] 'Capacitance and Dielectric Properties of Ni/n-GaAs Schottky diode Under Swift Heavy Ion Irradiation Environment' by A Bobby, N Shiwakoti, P M Sarun, S Verma, K Asokan and B K Antony, Cur. Appl. Phys., (Accepted 2015).
- [5] L. E. Byrum et al., J. Appl. Phys., 106 (2009) 053701.

5.2.32 Generation of calibration curve for neutron dosimetry via LET spectrometry

G.S. Sahoo, S. Paul, S.P. Tripathy, T. Bandyopadhyay

Health physics Division, Bhabha Atomic Research Centre, Mumbai, India

We have irradiated CR-39 detectors with 4 different ions of different energies, viz. 30 and 45 MeV Li, 50 and 80 MeV C, 50, 60 and 80 MeV O, 60 and 70 MeV F. The experiment was performed in

a low flux chamber, fixed with general purpose scattering chamber (GPSC) at an angle of 15° with respect to primary beam direction. There was a provision to introduce a target ladder in the low flux chamber, which can be moved vertically upward or downward without disturbing the vacuum in the chamber. The aim of the investigation was to generate the calibration curve for Linear Energy Transfer distribution (LET spectra) with respect to different track parameters. The samples have been processed for 2 hours with an etching step of 1 h interval to develop the tracks and the images of the tracks were taken in each step using an optical microscope with 5 MP camera. The track parameters were analysed and the preliminary results are presented below. Fig. 5.2.50 shows the track area distribution corresponding to the ions of different LET (in water) values.

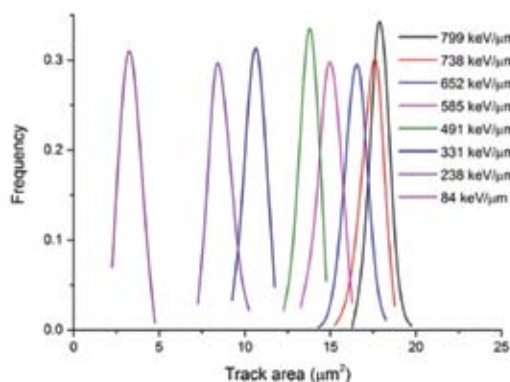


Figure 5.2.50: Track area distribution in CR-39 detectors corresponding to the ions of different LET values.

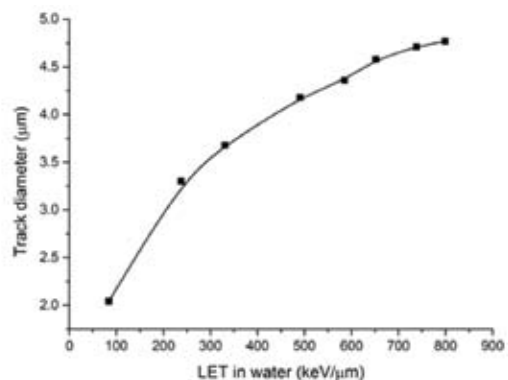


Figure 5.2.51: Variation of track diameter with LET in water.

Fig. 5.2.51 shows the variation of track diameter with LET in water. The results presented here correspond to only 2 hours of etching. The fig. 5.2.51 is a signature curve that will lead to generate the calibration curve. Further analysis is in progress to achieve the objective of the investigation.

5.2.33 Radiation damage and H/D retention studies in ion-irradiated Tungsten

P. M. Raole¹, Shishir Deshpande¹, Sameer Khirwadkar¹, C. Dube¹, P.N.Maya¹, C. Jariwala¹, Sai Krishana¹, P. Kulriya²

¹Institute for Plasma Research, Gandhinagar

²Inter-University Accelerator Center, Aruna Asaf Ali Marg, New Delhi – 110067, India.

Fusion energy production relies on the reaction of hydrogen isotopes deuterium (D) and tritium (T), forming helium and releasing 14-MeV neutrons. In the magnetic confinement approach to fusion, D-T plasma at a temperature of around 15 keV (about 150 million $\text{\AA}^\circ\text{K}$) is trapped in a toroidal magnetic field inside a vacuum vessel. The confinement is not perfect and the plasma interacts with the vacuum vessel wall, which may cause erosion of the surface and may also cause D/T to become trapped in the wall material, making it unavailable for fusion. Simultaneously, neutrons and ion bombardment create damage in the wall material and some of the D/T may escape through surface of the wall material back in plasma, making the situation at and near the surface very complex.

Tungsten is identified as Plasma facing candidate material for fusion reactors due to its favourable properties such as high melting point, low sputtering yield, high thermal conductivity and low T retention. To study the defect structure and the dependence of H/D transport and retention on

various aspects of irradiated Tungsten such as structural and microstructural changes, Irradiation parameters, substrate-temperature, presence of Helium and Helium Bubbles, Impurities/alloying elements etc., accelerators at IUAC have been used for irradiation of high energy (80 MeV) and low energy (100 keV) heavy (Au) ions in pristine and annealed (900 °C) Tungsten at various fluences from 6.2×10^{14} to 1×10^{17} ions/cm². In the first phase of investigation, the samples are subjected to X-ray diffraction (XRD), Positron Annihilation spectroscopy (PAS), Atomic force microscopy (AFM) and Scanning electron microscopy (SEM) analysis for studying the structural, micro-structural, morphological changes. XRD analysis reveals that there is considerable stress produced in irradiated zone of 80 MeV Au implanted samples as compared to pristine samples. Such stress may play an important role in H/T transport in tungsten bulk. AFM results show (Fig. 5.2.52) nano-structuring in 80 MeV Au implanted pristine samples. However, irradiation after annealing does not show considerable nano-structuring. The SEM shows smooth surface with some voids in 100 keV Au irradiated pristine and annealed (Fig. 5.2.53) samples. The mechanism for this nano-structuring and smooth morphology is being investigated. Positron Annihilation spectroscopy (PAS) results indicate that in 80 MeV Au implanted samples the vacancy clusters are more than mono-vacancy type defects.

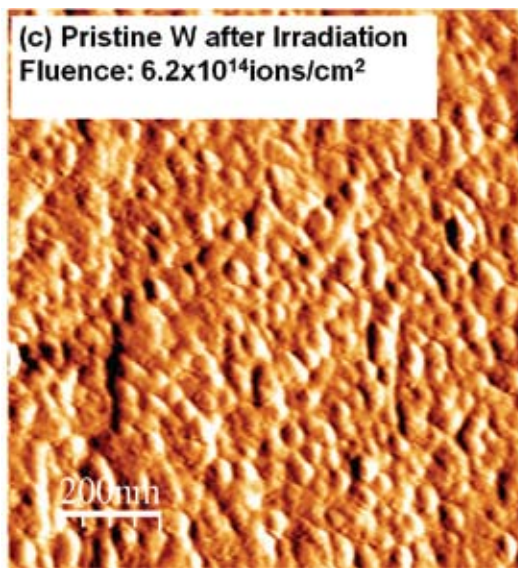


Figure 5.2.52: AFM image of Pristine Tungsten after 80 MeV Au ion irradiation.

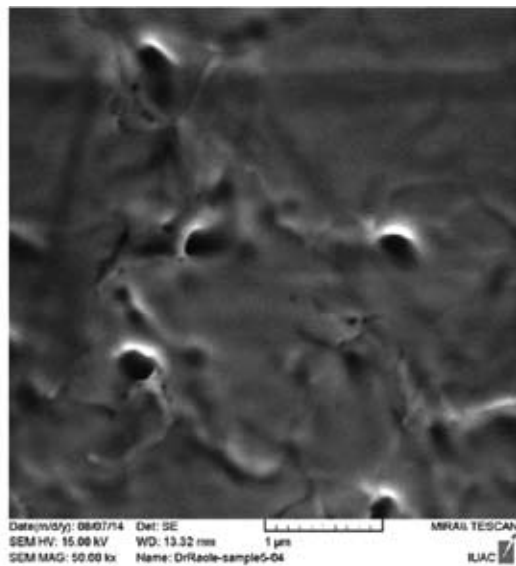


Figure 5.2.53: SEM image of Annealed W after Irradiation for the Fluence of 1×10^{17} ions/cm².

5.2.34 Nanoscale resistive switching in Ar⁺-ion irradiated TiO₂ layers on Pt

Barman¹, C.P. Saini¹, D. Kabiraj², D. Kanjilal², S. Dhar¹, and A. Kanjilal¹

¹Department of Physics, School of Natural Sciences, Shiv Nadar University, NH-91, Tehsil Dadri, Gautam Buddha Nagar-201314, India

²Inter-University accelerator centre, Aruna Asaf Ali Marg, New Delhi 110067, India

In last decades transition metal oxides (TMO) have emerged as the potential candidates for the next generation resistive switching (RS) non-volatile memory (NVM) application as it satisfies the basic requirements like high speed and endurance, long data retention along with simple miniaturized structure compatible with the present CMOS industry [1, 2]. Among several TMOs, TiO₂ has

proved itself as a possible candidate for such application, not only for fulfilling the aforementioned criteria of NVM but also for its cost effectiveness, and above all its superior physical and chemical properties [3]. However, the mechanism behind RS in TiO_2 is not yet clear and hence several models have been proposed in literature till date. Although, the oxygen vacancy (OV) migration is well accepted model to the scientific community, but yet need more systematic study to meet the agreement with experimental results [3]. We therefore study effect of vacancy in the TiO_2 -based memory devices by intentionally introducing defects by Ar^+ bombardment.

To execute the proposed plan we have partially generated OV-dominated TiO_2 layers by irradiating with 50 keV Ar^+ ions while the fluence (i.e. ions/cm²) were varied from 5×10^{14} to 5×10^{16} ions/cm². The ion irradiated samples have been characterized by conducting atomic force microscopy (cAFM) (Fig. 5.2.54(a)-(f)) and its complementary current-voltage (I-V) spectroscopy for investigating localized RS property. A systematic improvement in RS behavior was observed with increasing fluence (Fig. 5.2.54(g)). For understanding underlying process, structural property before and after irradiation was carried by GI-XRD, whereas the microscopic property was examined by high-resolution transmission electron microscope (HRTEM).

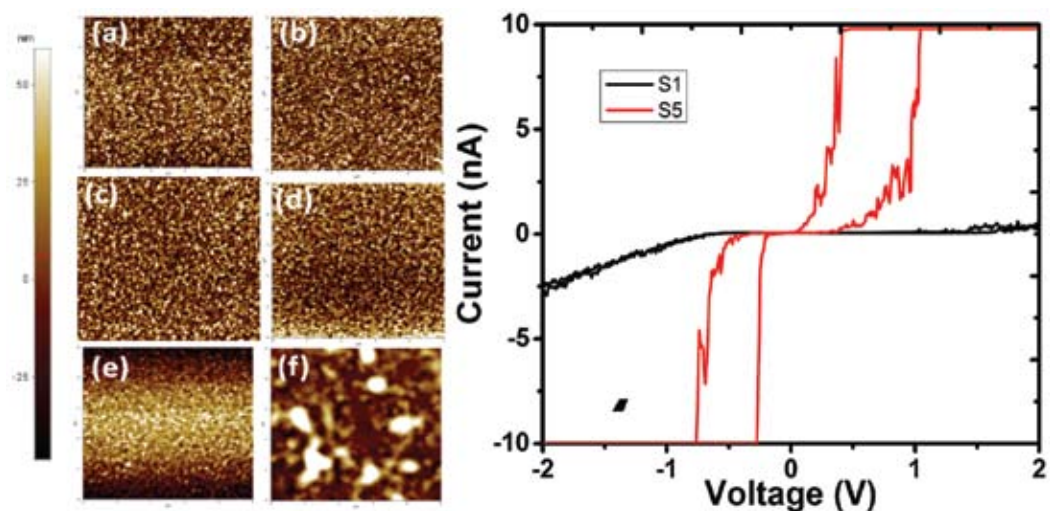


Figure 5.2.54: The AFM topographies of (a) as grown TiO_2 layer, and after Ar^+ -ion bombardment with (b) 5×10^{14} , (c) 1×10^{15} , (d) 5×10^{15} , (e) 1×10^{16} , and (f) 5×10^{16} ions/cm². (g) I-V characteristics with fluences of 5×10^{14} ions/cm² (S1) and 5×10^{16} ions/cm² (S5) using 10 nA compliance.

REFERENCES

- [1] Mario Lanza, *Materials* 7 (3), 2155 (2014).
- [2] H-SP Wong et al., *Proceedings of the IEEE* 100 (6), 1951 (2012).
- [3] Rainer Waser, Regina Dittmann, Georgi Staikov, and Kristof Szot, *Adv. Mater.* 21 (25-26), 2632 (2009).

5.2.35 Enhanced Photo-absorption and Super Paramagnetic behaviour from TiO_2 Nanostructures

Vanaraj Solanki¹, Subrata Majumder¹, I. Mishra¹, P. Dash², Shalik Ram Joshi¹, Pramita Mishra¹, N. C. Mishra², D. Kanjilal³, and Shikha Varma^{1*}

¹Institute of Physics, Bhubaneswar, 751005, India.

²Utkal University, Bhubaneswar, 751004, India.

³Inter-University Accelerator Centre, Aruna Asaf Ali Marg, New Delhi 110 067, India

The papers discuss the Photo-absorption and Magnetic behaviour of two dimensional rutile TiO₂ nanostructures after ion beam sputtering of TiO₂(110) surfaces. The results show that the photo-absorption response depends, in a complex fashion, on the size of 2d nanostructures that are created post irradiation. These results have been obtained in the absence of any dopant material and can have extensive implications for photocatalytic activity of TiO₂ based devices [1,3]. Nanostructures also show superparamagnetic behaviour [2]. TiO₂ single crystals were irradiated with 60 keV Ar⁺ ions from ECR source at a variety of fluences varying from 5×10^{15} to 5×10^{17} ions/cm².

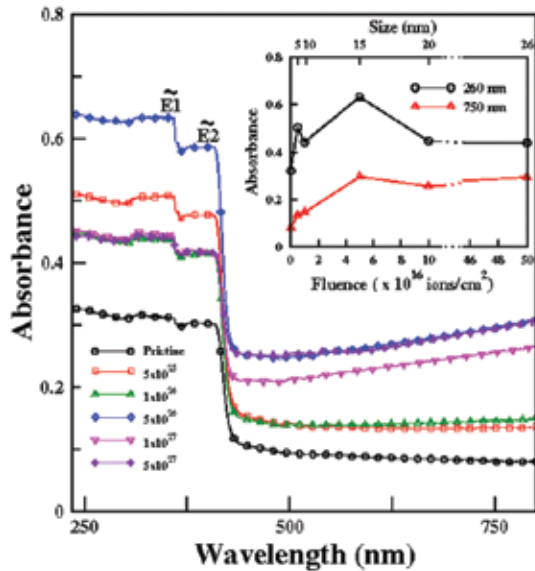


Figure 5.2.55: Optical absorbance for pristine and irradiated sample. Inset shows absorbance at the wavelengths of 260 and 750 nm, respectively.

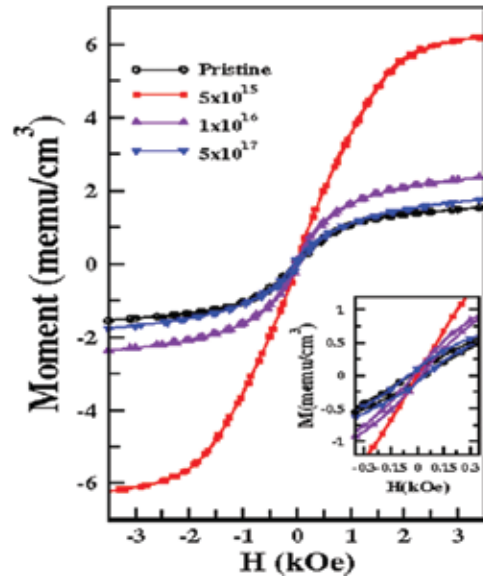


Figure 5.2.56: M-H curve measured at RT

Optical absorption spectra from ion irradiated and pristine TiO₂ surfaces are shown in the fig. 5.2.55 and display two absorption band edges, $\tilde{E}1$ and $\tilde{E}2$, with the former being related to the direct bandgap transition and the later to transition due to the oxygen vacancy states. A significant intensification of absorbance, compared to pristine, is demonstrated at all the fluences. Surprisingly the maximally absorbing response is generated by nanostructures of 15nm size created at fluence of 5×10^{16} ions/cm² and not by smallest nanostructures (created at 5×10^{15} ions/cm²). Results presented here [1] reflect a complex dependence of photo-absorption on the size of nanostructures. Detailed quantitative investigation of oxygen vacancy states show that competition between the size of nanostructures and the number of vacancy states controls the photo-absorption properties.

Pronounced quantum confinement effects in TiO₂ nanodots and a direct correlation between the size of nanostructures (NS) and magnetic behaviour (Fig. 5.2.56) has also been observed [2]. This suggests that the size of NS plays crucial role in the evolution of magnetic nature. Though the smallest (~ 5 nm) NS display superparamagnetic (SPM) behaviour, ferromagnetism is observed for larger nanostructures. Single domain nature of TiO₂ quantum dots is responsible for the observed SPM behaviour.

REFERENCES

- [1] Vanaraj Solanki et al., J. of Appl. Phy. 115 (2014) 124306.
- [2] Vanaraj Solanki et al., Nucl. Instru. Meth, B (2015) in press.
- [3] Vanaraj Solanki et al., Rad. Eff. Def. Solids 168 (2013) 518.

5.2.36 Synthesis and characterization of α -Fe₂O₃ thin films

Indra Sulania¹, Jyoti Kaswan²

¹Inter-University Accelerator Centre, Aruna Asaf Ali Marg, New Delhi 110 067, India

²Amity University, Haryana

In recent years, research on transition metal oxide (TMOs) thin films such as Iron oxide has attracted much attention for their potential technological applications such as light-induced water splitting [1], gas sensors [2], solar cells [3], magnetic recording [4] etc. Iron oxide exhibits different phases such as FeO, α -Fe₂O₃, γ -Fe₂O₃, β -Fe₂O₃ and Fe₃O₄. Hematite (α -Fe₂O₃) is the most stable iron oxide with rhombohedrally centred hexagonal structure [5, 6].

In this work, thin films of α -Fe₂O₃ are synthesized on Si (100) using resistive heating method and annealed at 400°C in oxygen for 2 h. We studied the structural, morphological and transport properties of the samples upon 10 keV N⁺ ion implantation at a fluence of 1×10^{17} ions/cm².

The structural properties of the film were studied using X-ray diffractometer (Bruker D 8 Advance, Germany) with Cu K α radiation of wavelength 1.54 Å. Fig. 5.2.57(a) shows the XRD of the α -Fe₂O₃ thin films. The peaks at 24.66° (012), 32.94° (104), 40.68° (113), 57.69° (018) are identified by matching with the JCPDS data files. The films were found to be polycrystalline in nature. The average crystallite size was found to be 5 nm using the Debye Sherrer's formula. The films were also analysed by Raman spectroscopy. Fig. 5.2.57(b) shows the Raman spectra taken with a Reinshaw Raman spectrometer using a 514 nm Ar⁺ laser as the excitation source. The peak located at 226 cm⁻¹ corresponds to the A_{1g} mode and the four peaks at about 245, 293, 413 and 612 cm⁻¹ are attributed to the E_g mode [7].

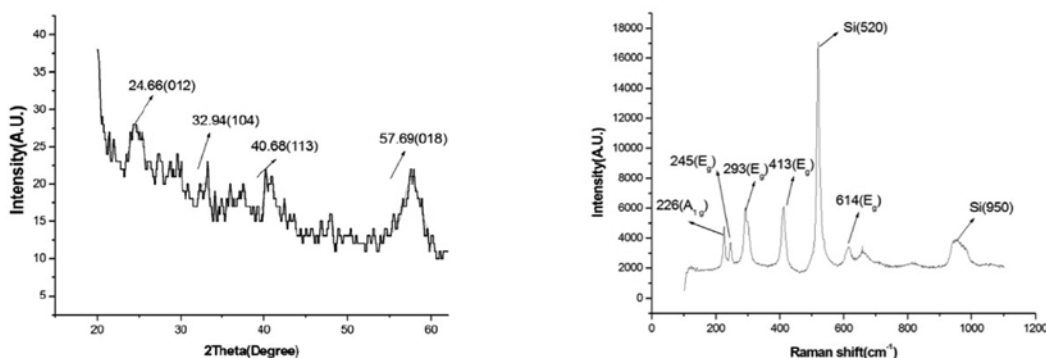


Figure 5.2.57: (a) XRD and (b) Raman spectra of annealed α -Fe₂O₃ thin film.

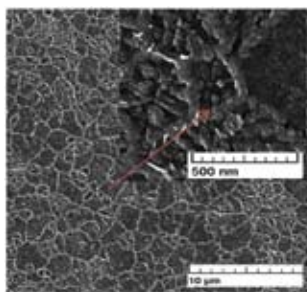


Figure 5.2.58: SEM image of annealed α -Fe₂O₃ thin film

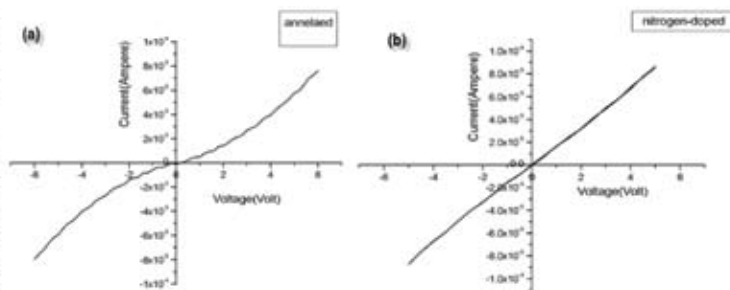


Figure 5.2.59: IV curves for (a) annealed and (b) doped α -Fe₂O₃ film samples

Fig. 5.2.58 shows SEM images of the annealed samples taken with MIRA/TESCAN with electrons of energy 25 keV. The image shows the formation of porous or mesh kind structures which comprises of Fe and O as seen with EDAX. The average grain size was found to be approximately 20 nm. It is also observed that the nanowalls forming the porous film are parallel to the plane of the sample and are about 60 nm in width. The inset of fig. 5.2.58 shows a high-magnification SEM image of the surface, from which we see that the film consists of grains which comprises of many smaller grains or clusters of nanoparticles.

There are reports that the α -Fe₂O₃ films formed by thermal evaporation have n-type semiconducting behaviour. The I-V characteristics for our samples in fig. 5.2.59 show the semiconductor to Ohmic characteristics upon doping with N⁺ ions. The thin films of α -Fe₂O₃ were synthesized successfully and showed a transition from semiconducting characteristics to Ohmic characteristics upon doping with N⁺ ion.

REFERENCES

- [1] I. Cesar, A. Kay, J.A. Gonzalez Martinez and M. Grätzel, J Am Chem Soc 128 (2006) 4582.
- [2] X. Gou, G. Wang, J. Park, H. Liu and J. Yang, Nanotechnol 19 (2008) 125606.
- [3] H. Zhou and S.S. Wong, ACS Nano 2 (2008) 944.
- [4] C.Z. Wu, P. Yin, X. Zhu, C.Z. OuYang and Y. Xie, J Phys Chem B 110, 17806 (2006).
- [5] N. Beermann, L. Vayssieres, S.-E. Lindquist and A. Hagfeldt, J Electrochem Soc 147, 2456 (2000).
- [6] M.F. Al-Kuhaili, M. Saleem and S.M.A. Durrani, J Alloys Comp 521, 178 (2012).
- [7] D L A Faria, Venaüncio Silva S and M T de Oliveira J. Raman Spectrosc. 28 (1997) 873

5.2.37 Influence of ion flux and fluence on evolution of phonon modes of Zinc Oxide thin films under 300 keV Argon ion Irradiation: Micro-Raman studies

Kanchan Joshi^{1*}, Fouran Singh², Subodh K. Gautam², R.G. Singh³, S. Ojha², R.C. Ramola¹

¹Department of Physics, Badshahi Thaul Campus, H.N.B.Garhwal University, Tehri Garhwal 249199, India

²Inter-University Accelerator Centre, Aruna Asaf Ali Marg, New Delhi 110 067, India

³Department of Physics, Bhagini Nivedita College University of Delhi, New Delhi 110043, India

Recent advances in Zinc oxide (ZnO) have shown potential for transparent conductors in solar cells, UV light emitters, as component in electronics and gas and chemical sensors [1]. In order to understand the modifications due to defects in the lattice after irradiation Raman scattering has been used as the characterization tool in our case. This fundamental research can lead to various industrial and technological applications of ZnO worldwide. ZnO thin films were deposited using sol-gel spin coating for a thickness of about 300 nm on silicon substrates and were post annealed at 850 °C for 1 hour in controlled oxygen environment. The annealed films were irradiated using 300 keV for the varying fluxes from 1 μ A to 20 μ A for the same ion fluences. Films were investigated to understand the phonon evolution kinetics mainly in the region of longitudinal optical modes of A_1 and E_1 symmetry, which is otherwise forbidden in the backscattering geometry of measurements. Raman studies depending on varying flux from 1 μ A to 20 μ A at a constant fluence of 1×10^{14} ions/cm² visible from Fig.5.2.60(a) show that the sharp peak of E_2 (high) mode in pristine ZnO is very much suppressed after irradiation at 1 μ A flux [2]. Also there is evolution of A_1 (LO) mode at this flux whose intensity keeps on increasing with increase in flux. The evolution kinetics of this mode was previously studied under swift heavy ions (SHIs) irradiation for the origin of this mode and investigated with increase in ion fluences [3]. It is better to note that evolution kinetics of A_1 (LO)

mode with increase in ion flux for the same fluence is similar to behaviour with increase in ion fluences for the SHI irradiations as observed in fig. 5.2.60(b). However, the softening of this mode is not observed under low energy ions.

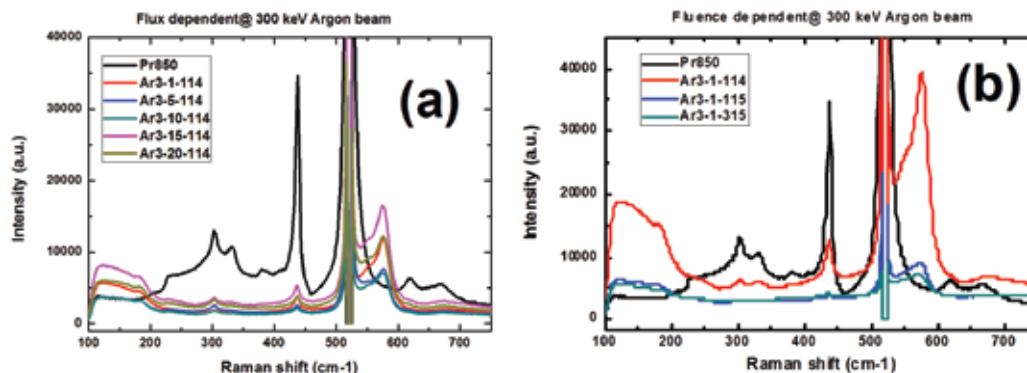


Figure 5.2.60: (a) Flux dependent Raman spectra at 1×10^{14} fluence. (b) Fluence dependent Raman spectra at 300keV Ar beam of pristine and irradiated films.

The evolution kinetics of A1(LO) mode is attributed to the creation of high density of defects, while the non-observations of softening for low energy ions is understood in framework of the thermo-elastic model [4]. Detailed results micro-Raman studies along with grazing incidence X-ray diffraction, and Atomic Force Microscopy (AFM) will be presented later. The creation of defects and disorder by ion irradiation in the films is indirectly evidenced by Raman analysis, and it is concluded that evolution kinetics of phonon modes can be thus modified as the effect of energetic ion irradiation.

REFERENCES

- [1] R.G.Singh, F.Singh et al. J.Phys.D: Appl.Phys.42/FTC,062002(2009)
- [2] J. M. Calleja and M. Cardona, Phys. Rev. B 16, 3753 (1977).
- [3] F. Singh et al. J. Appl. Phys. 110,083520(2011)
- [4] F.Singh, J.P. Stoquert, and J.C. Pivin, J. Phys. D: Appl.Phys. 46, 325305(2013)

5.2.38 Effect of 200 keV Si- ion irradiation on g-C₃N₄

B.Varalakshmi¹, K.V.Sreenivasulu¹, K.Asokan², V.V.S.S.Srikanth¹

¹School of Engineering Sciences and Technology, University of Hyderabad, Hyderabad

²Inter-University Accelerator Centre, Aruna Asaf Ali Marg, New Delhi 110 067, India

In the present work, effect of ion beam irradiation on structural and morphological aspects of graphite like carbon nitride (g-C₃N₄) was investigated. The g-C₃N₄ material is prepared by using simple atmospheric thermal decomposition process. The as-prepared g-C₃N₄ was pelletized under a pressure of 3 Tonne. These pellets, of ~10 mm in diameter, were irradiated with Si [1] ion beam of energy 200 keV with 2×10^{15} , 3×10^{15} , 5×10^{15} , 1×10^{16} , 2×10^{16} and 3×10^{16} ions/cm² fluencies. The irradiated samples are characterized by X-ray diffraction (XRD), field emission scanning electron microscopy (FESEM). FESEM micrographs (Fig. 5.2.61) revealed that the morphology changed to sheet like surfaces from network structure after irradiation. Presence of Si, C and N elements was confirmed by EDS analysis.

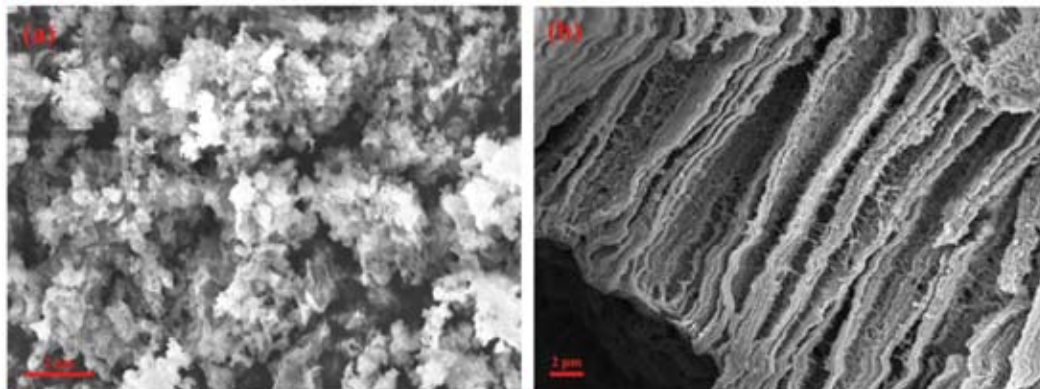


Figure 5.2.61: FESEM micrographs of $g\text{-C}_3\text{N}_4$ (a) pristine and (b) irradiated with 200 keV Si ion

REFERENCES

- [1] Po Wu et al., conference paper: January-2012

5.2.39 Fabrication of p-n junction diode by doping p-type impurity in n-type Indium antimonide nitride / Indium antimonide Bismide

Manisha Deshpande^{1,5}, Dilip Maske^{2,5}, Devarani Devi³, Rashmi Choudhari⁵, Brij Mohan Arora⁴, Dattatray Gadkari⁵

¹Department of Physics Jai Hind College, Mumbai-400020, India

² Department of Physics D. G.RuparelCollege, Mumbai-400016, India

³Inter-University Accelerator Centre, Aruna Asaf Ali Marg, New Delhi-110 067, India

⁴Department of Electrical Engineering Department, IIT, Mumbai-400076, India

⁵Department of Physics MithibaiCollege, Mumbai-400056, India

The fabrication and characterization of p-n junction by ion implantation of Te ions on p type InSb substrate grown by VDS was reported by D. B. Gadkari [1]. The leakage current in this case was very low and the diodes formed using ion implantation of tellurium atoms show rectifier like characteristics. The study of p-n junction diodes was also reported on thin film of InSb:N formed using molecular beam epitaxy where Carbon was used as p type dopant [2]. In another literature, nitrogen implantation to form InSb: N is reported [3]. In this study the diodes were formed on bulk substrates of InSb:N, InSbBi, GaSb and GaSbSe using ion implantation of Boron ions. Boron implantation was carried out using negative ion accelerator. Boron atoms were chosen for implantation as the Boron atoms are suitable as p type dopant and they are suitable for negative ion implantation.

The depth of implanted ions was estimated using software, The Stopping and Range of Ions in Matter (SRIM). The simulation indicates ion range in InSb:N was 201.4 nm where the atoms straggled about 95 nm for 100 keV. The distribution of ions is not uniform over depth for single stage ionization. Hence two step ion implantation was carried out where energy of ion beam used

in second implantation was 50keV. The simulated range for 50keV is 122.4 nm. The beam size was $5\text{mm} \times 6\text{mm}$. The implantation dose of Boron ions was $1 \times 10^{17} / \text{cm}^3$ and ion current was 300nA to 450nA. The as-implanted sample was used for measurements. The wafer was not annealed to avoid further boron diffusion in the wafer. The damage of crystal surface due to ion implantation was studied using Raman spectra at IUAC lab. As shown in Fig.5.2.62, the forbidden LO peak intensity increased after ion implantation.

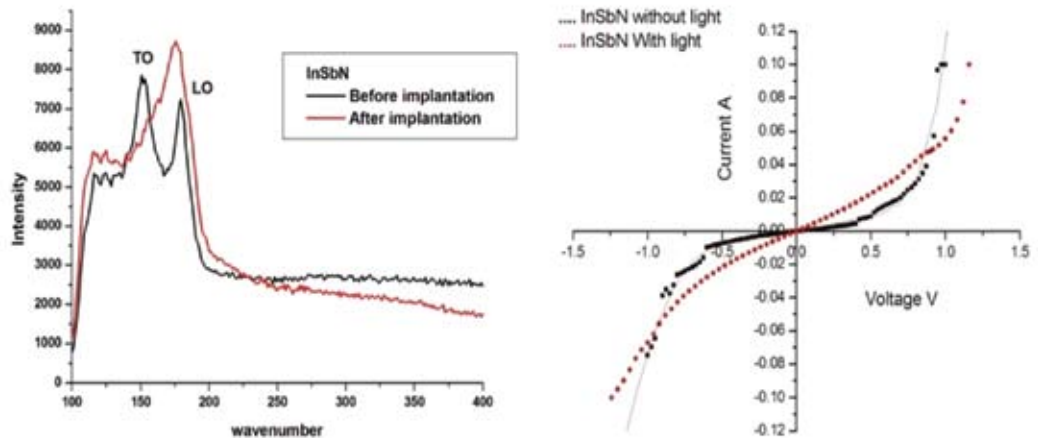


Figure 5.2.62: Raman Spectra of InSb:N substrate Figure 5.2.63: I-V characteristics of p-n junction diode

SIMS analysis indicated presence of bond formation of Sb-B. The incorporated Boron atoms were active. I-V characteristics of the p-n junction diode formed on the substrate of InSb:N is shown in Fig. 5.2.63. The ideality factor at room temperature was 1.2. The forward current was limited by contact resistance. The reverse current was large and did not saturate. The p-n junction formed by boron implantation shows photosensitive nature.

REFERENCES

- [1] Dattatray Gadkari, International Journal of Engineering and Applied Sciences (IJEAS), Volume-2, Issue-4, (2015), pp 39-44.
- [2] H T Pham, S F Yoon, K P Chen and D Boning, J. Phys. D: Appl. Phys. 41 (2008) pp- 025304.
- [3] D. H. Zhang, W. Liu, Y. Wang, X. Z. Chen, J. H. Li, Z. M. Huang, and Sam S. Y. Zhang, App. Phy. Lett. 93, (2008), pp 131107 (1-3)

5.2.40 Ion beam induced Optical and surface modification in coupled plasmonic nanostructures

Udai B. Singh, Subodh K. Gautam, Sunil Kumar, Sonu Hooda and Fouran Singh

Inter-University Accelerator Centre, Aruna Asaf Ali Marg, New Delhi 110067, India

Coupled plasmonic nanostructures, such as nanoparticles dimers or larger clusters of nanoparticles have been studied extensively. Controlling and tuning the optical properties of these structures relies heavily on the ability to precisely manipulate the gap size between them, effectively determining how strongly they couple. As a result, much effort have been devoted towards fabrication techniques that guarantee control over this has also been achieved in close proximity to each other.

Film-coupled nanoparticle systems have established a trustworthy stage for investigating the field enhancement connected with sub-nanometer sized gaps between plasmonic nanostructures. Several methods are used for fabrication of these types of systems. Among them, ion irradiation is a well-established tool for synthesis of nanostructures on the surface or embedded NPs [1]. This is one of the standard ways to synthesize of noble metal NPs which offers control over the depth distribution of NPs by properly adjusting ion beam parameters, such as ion energy, ion dose, dose rate and substrate temperature. Zinc oxide (ZnO) is an interesting material due to its large band gap and large exciton binding energy. Ion irradiation of ZnO has proven a potential role in materials due to formation of defects which is very useful for applications. The film-coupled nanostructures present the advantage in enhancement of optical properties due to coupling effect. Therefore, ion beam irradiation can be used to understand and control the evolution of optical properties of ZnO due to coupling of nanostructures and thin film. In this report, the origin of Raman mode and variation in band gap is reported with 1200 keV Xe ion irradiation.

Thin films of Au (10nm)/ZnO/Au (30nm)/Glass were irradiated with 1200 keV Xe ions with constant current 2.89 μ A in Low energy ion beam facility at IUAC, New Delhi at angle of 70 degree from surface normal. The optical absorption spectra of samples were recorded using a dual beam Hitachi U-3300 UV-VIS spectrophotometer. Micro-Raman measurements were performed using Renishaw InVia Raman microscope at IUAC, New Delhi. Micro-Raman measurements were carried out in back-scattering geometry under the excitation by 514.5 nm (TEM00) photons of 50 mW Argon ion laser from Spectra Physics. The surface morphology of the pristine and irradiated samples was recorded using field emission scanning electron microscopy (FE-SEM) [MIRA\\, TESCAN] at IUAC, New Delhi.

Surface morphology of the pristine and irradiated films as studied by SEM is shown in Fig. 5.2.64(a)-(c). The image of the pristine film shows compact distribution of grains on the surface of the film. The ion-induced dewetting causes the formation of percolated structures with ion beam irradiation. The band gap is determined using Tauc's plot as shown in the Fig. 5.2.64 (d) reveals a red shift from 3.09 to 2.64 eV for pristine film and irradiated at highest fluence of 1×10^{16} ions/cm². The decrease in the band gap can be understood due to increase in the defects with increase in ion fluence. The micro-Raman spectra of pristine and irradiated films at the fluence of 1×10^{15} ions/cm² and 1×10^{16} ions/cm² are shown in Fig. 5.2.64(e). The all the observed phonon modes are marked in the figure. The spectra display peaks at 701, 767, 440, 373, 353, 333 cm⁻¹. It is observed that pristine film does not show any mode in the region from 573 to 580 cm⁻¹. However, the irradiation by 1×10^{15} ions/cm² ions, the appearance of a mode at 573 cm⁻¹ the film, which shows increase in intensity and width along with a softening of mode from 573 to 569 cm⁻¹ with increase in ion fluences.

The origin of the low energy ion bombardment induced phonon mode around 573 cm⁻¹ is very interesting as it develops and red shifted with increase in ion dose. The development of these Raman modes can be attributed to the effect of disorder and lattice defects induced by low energy irradiation [2]. The softening in this Raman peak is explained due to the combined effects of phonon localization by lattice defects and structural strain in the lattice induced by energetic heavy ions.

REFERENCES

- [1] Udai B. Singh et al., Beilstein J. Nanotechnol. 2014, 5, 105-110
- [2] Fouran Singh et al., Journal of Applied Physics 110, 083520 (2011)

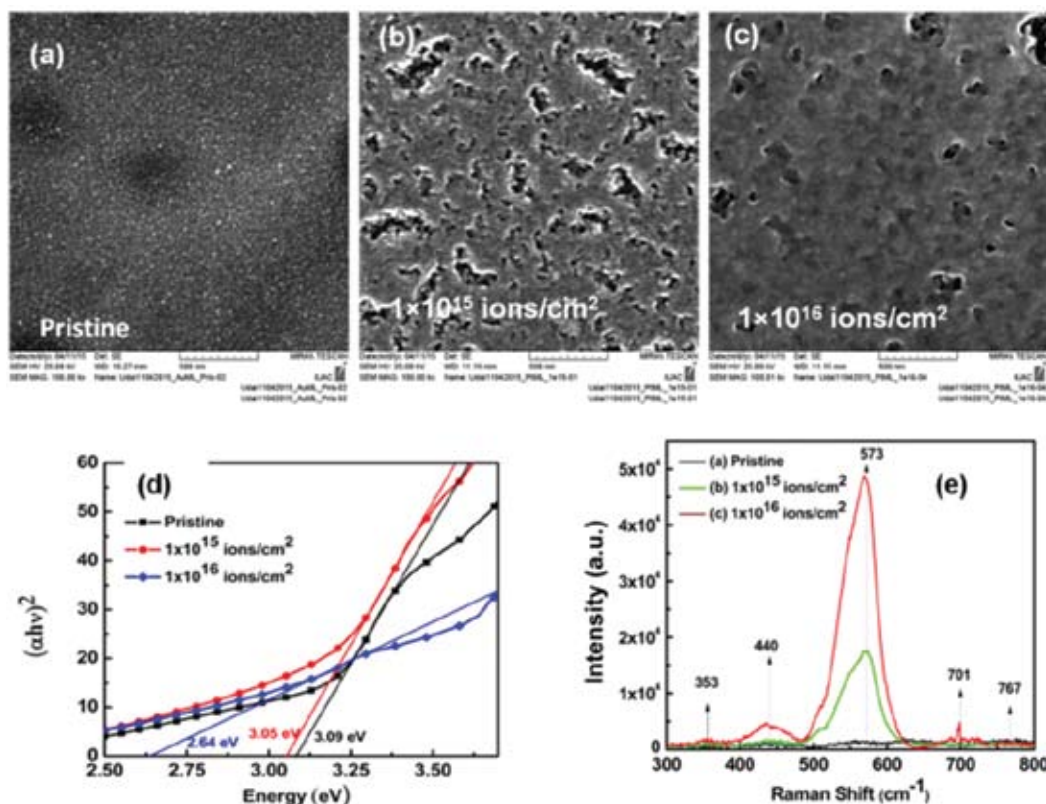


Figure 5.2.64: SEM micrograph of (a) Pristine and irradiated films (b) at the fluence of 1×10^{15} ions/cm² (c) at the fluence of 1×10^{16} ions/cm² (d) Tauc's plot of pristine and irradiated film and (e) Raman spectra of pristine and irradiated films

5.2.41 To study the effect of low energy Ar ion irradiation on the optical properties of gold nanogratings and its application in biological sensing

Saswat Mohapatra¹, M. Rakesh Singh¹, D. Kabiraj²

¹Department of Applied Physics, Indian School of Mines, Dhanbad-826004

² Inter-University Accelerator Centre, Aruna Asaf Ali Marg, New Delhi-110067, India

Ion beam irradiation is a distinctive method for synthesis and modification of nanostructures[1]. Irradiation of ion beam or electrons in the metallic thin films, normally gives the formation of atomic defects or patterning in the metallic thin films [2]. In this research work, we have fabricated two types of polymer nanogratings structures from CD and DVD template by using soft UV nanoimprinting lithography. A set of samples prepared from CD template, we named as S1 and another set of samples prepared using DVD template was named as S2 respectively. We have coated 25 nm gold on 14 samples each of S1 and S2. Another 4 samples (without nanostructures) were also deposited with 25 nm of gold film as reference samples. In addition, 80 nm gold coated were coated on 2 samples each of S1 and S2. Gold films were deposited using high vacuum thermal evaporator at Target Lab, IUAC. The measured vacuum pressure before evaporation was 7×10^{-7} mbar and during evaporation was 3.8×10^{-6} mbar. The voltage of the evaporator was 220 V and current was 10 mA. We have taken the source-substrate and source-quartz crystal distance 17 cm each.

After successful gold deposition, the samples were loaded on the sample holder for Ar ion beam irradiation at LEIBF unit. The energy of the ion beam used in the experiment were 80 keV and 1 MeV under normal incidence at fixed fluences 5×10^{14} ions/cm²; beam current was 500 nA; working chamber pressure was 2.8×10^{-6} torr. To obtain the beam energy of 1 MeV, 4+ charge state of argon ion was chosen. Different fluences of Ar ion were chosen as, 1×10^{13} ions/cm², 5×10^{13} ions/cm² and 1×10^{14} ions/cm². After the Ar ion irradiation, the samples were characterized using scanning electron microscope (SEM) to study the surface morphology. Figure 5.2.65 show the SEM images of the ion irradiated samples with fluences of, 1×10^{13} ions/cm², 5×10^{13} ions/cm² and 1×10^{14} ions/cm² respectively on S1 [see (a)-(c)] and S2 [see (d)-(f)]. As seen from the SEM images, there is fracture of the gold film after ion irradiation and samples were burn after irradiating with higher ion fluences of 5×10^{14} ions/cm². The fracture regions of gold film with nanometer gap could have very strong light confinement. This could be hotspots for Surface Enhance Raman Spectroscopy (SERS) for ultrasensitive detection of biological/chemical molecules at single molecular level. This will be final goal of this project.

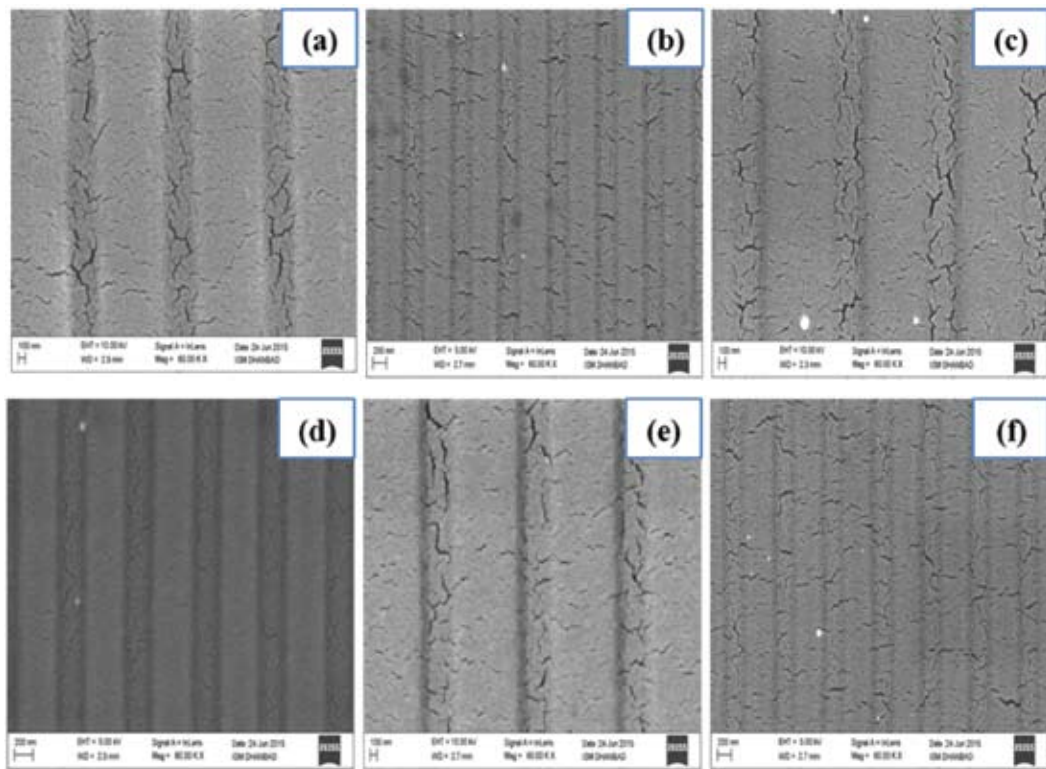


Figure 5.2.65: SEM images of grating sample with Ar ion irradiation with different fluences of gold thickness 25 nm (a) S1; 1×10^{13} ions/cm², (b) S1; 5×10^{13} ions/cm², (c) S1; 1×10^{14} ions/cm², (d) S2; 1×10^{13} ions/cm², (e) S2; 5×10^{13} ions/cm² (f) S2; 1×10^{14} ions/cm².

REFERENCES

- [1] Jai Prakash et al., J. Phys D: Appl. Phys, 44 (2011), 125302.
- [2] A.V. Krashennnikov and K. Nordlund, Journal of Applied Physics, 107, (2010), 071301.

5.2.42 Native defects and optical properties of Argon ion irradiated ZnO

S. Pal¹, A. Sarkar², D. Sanyal³, T. Rakshit⁴, D. Kanjilal⁵, P. Kumar⁵, S. K. Ray⁴ and D. Jana¹

¹Department of Physics, University of Calcutta, 92, Acharya Prafulla Chandra Road, Kolkata 700 009, India

²Department of Physics, Bangabasi Morning College, 19, R. C. Sarani, Kolkata 700 009, India

³Variable Energy Cyclotron Centre (VECC), 1/AF, Bidhannagar, Kolkata 700 064, India

⁴Department of Physics, Indian Institute of Technology, Kharagpur 721302, India

⁵Inter-University Accelerator Centre, Aruna Asaf Ali Marg, New Delhi 110067, India

Large direct band gap (3.37 eV at 300 K), high exciton binding energy (~ 60 meV) and extreme radiation hardness makes Zinc Oxide (ZnO) a suitable material for optoelectronic devices to be operated in radiation rich environment [1, 2]. Here, changes in optical and electrical properties of polycrystalline ZnO have been studied due to 1.2 MeV Argon ion irradiation (using LEIBF, IUAC, New Delhi) [3]. White coloured ZnO turns to yellowish with low fluence irradiation (1×10^{14} ions/cm²) and finally it becomes reddish brown in colour after irradiation with highest fluence 1×10^{16} ions/cm². UV-Visible absorption spectra of irradiated ZnO have been correlated with their changes in colour. In the absorption spectra [Fig. 5.2.66 (solid line)] of irradiated samples huge tailing in the low energy regime has been observed. The difference curve [Fig. 5.2.66 (dashed line)] of low fluence absorption spectra clearly shows a broad absorption in blue spectral region with a tailing in green region causing yellow colouration. This blue absorption can be considered as a single Gaussian peak with centroid at ~ 3.05 eV arises due to presence of oxygen vacancies (V_O). The absorption extends across blue, green and red spectral region in case of high fluence irradiated spectra and makes the sample reddish brown in colour. Interestingly, it is seen that the sheet resistance have been increased with 1×10^{14} ions/cm² fluence. However, at a fluence of 1×10^{16} ions/cm², sheet resistance decreased up to three orders of magnitude compared to the pristine one. From GAXRD pattern of all samples, it is seen that FWHM of (002) peak increased monotonically with increasing fluence which can be related with zinc sub-lattice disorder inside the sample. The Raman peak representing wurtzite structure of the ZnO material (~ 437 cm⁻¹) decreased with increase of irradiation fluence [Fig. 5.2.67]. Besides that, evolution of the 575 cm⁻¹ Raman mode in the irradiated samples shows increase of oxygen deficient disorder like zinc interstitials (I_{Zn}), V_O inside ZnO. Photoluminescence spectra of low fluence irradiated sample show overall luminescence quenching whereas high fluence irradiated spectra show a pure blue-violet emission [Fig. 5.2.68]. Zinc vacancy (V_{Zn}) type defects act as luminescence quencher in ZnO which is also electrically acceptor like. This makes the sheet resistance of low fluence irradiated ZnO highest. The blue-violet emission can be associated with I_{Zn} related transition. The I_{Zn} which is very unstable in ZnO is stabilized by V_O and this defect pair acts as an origin of n-type conductivity making the sample's sheet resistance lowest.

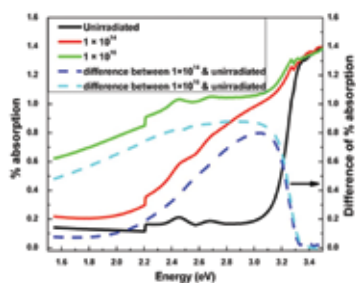


Figure 5.2.66: UV-visible absorption spectra of unirradiated and irradiated ZnO samples

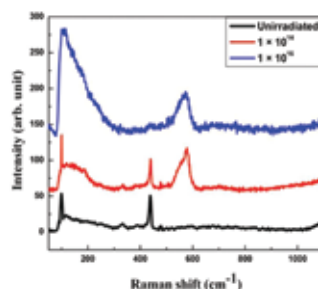


Figure 5.2.67: Raman spectra of unirradiated and irradiated ZnO samples

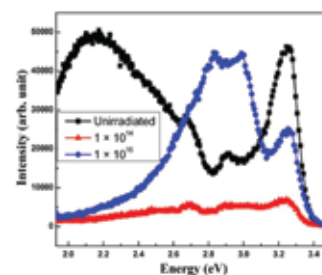


Figure 5.2.68: Room temperature photoluminescence spectra of unirradiated and irradiated ZnO samples

REFERENCES

- [1] S. Dutta, S. Chattopadhyay, A. Sarkar, M. Chakrabarti, D. Sanyal and D. Jana, Prog. Mater. Sci. 54, 89 (2009).
- [2] S. O. Kucheyev, J. S. Williams, C. Jagadish, C. Evans, A. J. Nelson, and A. V. Hamza, Phys. Rev. B 67, 094115 (2003).
- [3] S. Pal, A. Sarkar, D. Sanyal, T. Rakshit, D. Kanjilal, P. Kumar, S. K. Ray and D. Jana, Adv. Mater. Lett. 6, 365 (2015).

5.3 RADIATION BIOLOGY RESEARCH

5.3.1 Sodium fluoride toxicity & its combined effect with ^{12}C -ion beam radiation on A549 lung cancer cell line

Nitin Ghoshal*, A. N. Bhatt#, Asitikantha Sarma*

* Radiation Biology Lab, Inter-University Accelerator Centre, New Delhi

Institute of Nuclear Medicine & Allied Sciences, Delhi

Sodium fluoride (NaF) is an anti-glycolytic agent (inhibits enolase) thus blocking formation of pyruvate. According to recent reports NaF, at lower concentrations, although not significantly cytotoxic and genotoxic, induced oxidative stress leading to apoptotic cell death (Jyothiramajayam, M. *et al*, 2014). In an important study conducted using 980 probe sets (Tabuchi, Y. *et al*, 2014), 432 up-regulated and 548 down-regulated genes were identified, that were differentially expressed by >2.5 fold in the cells treated with 2 mM of NaF. The gene networks included various up-regulated genes which were primarily associated with the biological function of induction or prevention of cell death, respectively, such as *Atf3*, *Ddit3*, *Fos*, *Atf4* and *Haspa5*.

Tissue consequences of radiation exposure are dependent on radiation quality and high linear energy transfer (high-LET) radiation, e.g. heavy ions, known to deposit high amount of energy in tissues and cause extensive cluster DNA damage than low-LET (Cheema, A.K. *et al*, 2014). Therefore, considering such metabolic effects such as an increase in ROS, it could be interesting to explore any possible involvement of NaF in sensitizing cancer cells in collaboration with ^{12}C -ion beam irradiation.

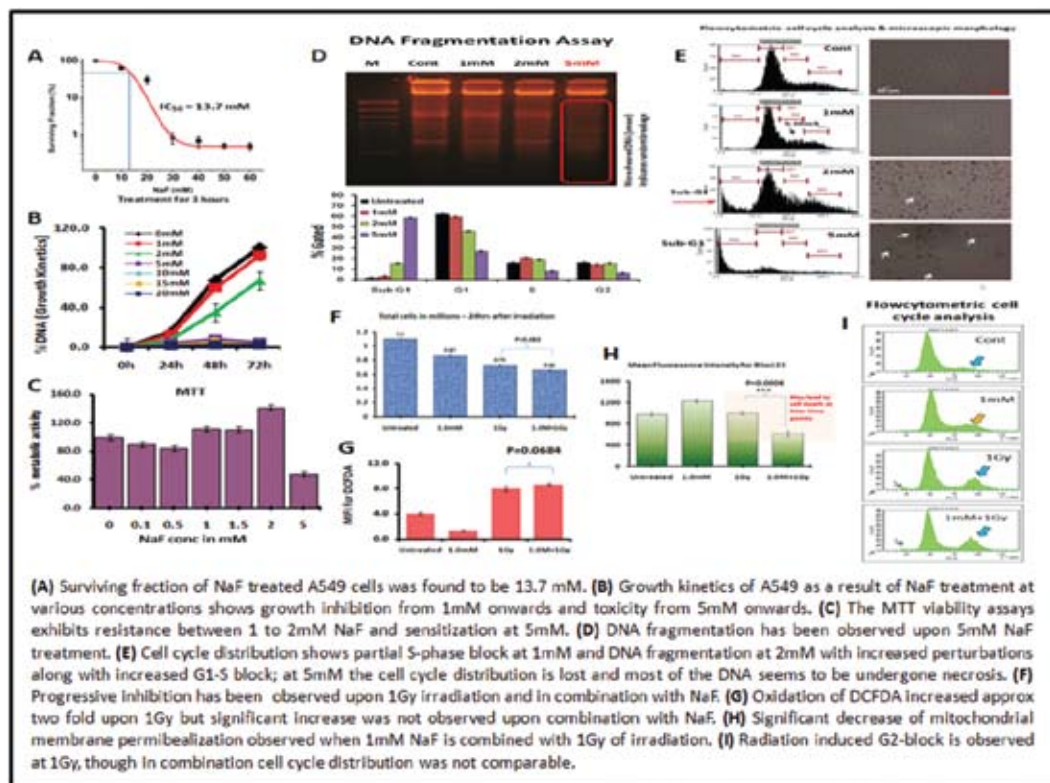


Fig. 5.3.1 The experimental observations

Not much has been documented about its radio-sensitization properties except in our earlier work (Podder, S. *et al*, 2015), where the interaction of DNA-lesions induced by sodium fluoride and radiation and its influence in apoptotic induction in cancer cell lines were explored. We are trying to explore its synergism with high LET radiation to sensitizing cancer cells. The irradiation methodology has been utilized in reference to (Kothari, A. 2015). We have determined the IC_{50} of NaF in A549 cell line to be 13.7 mM and cellular response have been checked at various concentrations of NaF on the basis of proliferation, morphological, cell cycle studies. A minimum dose of 1mM NaF was selected to be used in combination with a ^{12}C -ion beam dose of 1 Gy. NaF is administered for 24 h prior to irradiation and then assayed for sensitivity after 24 h of post irradiation incubation. Cell growth decreased in the combination treatment in comparison to radiation alone. Cell cycle analysis reveals G2-block upon 1Gy irradiation in addition to the DNA fragmentation in the combination treatment. Metabolic activity as measured by MTT assay increased gradually along with ROS as evident in DCFDA assay. The results are shown in Fig. 5.3.1. An important observation is the significant reduction in mitochondrial membrane potential in the combination treatment compared to radiation treatment alone as observed in total fluorescence of Rhodamine 123. We, hereby, aim to minimize the radiation dose by synergizing with optimum dose of NaF which would contribute to more efficient and economical heavy ion therapy protocols. Since only the mitochondrial sensitivity obtained is significant & therefore other cellular events that may lead to cell death in combination with different concentrations of NaF combined with radiation is being further investigated, therefore signifying the use of high-LET radiation, needs further exploration and is therefore under investigation.

REFERENCES

- [1] Jyothiramajayam, M.; Sinha, S.; Ghosha, M.; Nag, A.; Jana, A.; Mukherjee, A. Sodium fluoride promotes apoptosis by generation of reactive oxygen species in human lymphocytes. *J. Toxicol. & Env. Health.* (2014) 1269-1280.
- [2] Tabuchi, Y.; Yunoki, T.; Hoshi, N.; Suzuki, N.; Kondo, T. Genes and gene networks involved in sodium fluoride elicited cell death accompanying endoplasmic reticulum stress in oral epithelial cells. *Int.J. Mol. Sci.* (2014) 15(5): 8959-8978.
- [3] Cheema, A.K.; Suman, S.; Kaur, P.; Singh, R.; Fornace, A.J. Jr.; *et al.* Long term differential changes in mouse intestinal metabolomics after gamma and heavy ion radiation exposure. *PLoS ONE.* (2014) 9(1):e87079
- [4] Podder, S.; Ghoshal, N.; Banerjee, A.; Ganguly, B.; Upadhyay, R.; Chatterjee, A. Interaction of DNA-lesions induced by sodium fluoride and radiation and its influence in apoptotic induction in cancer cell lines. *Toxicology Reports.* (2015) 2:461-471
- [5] Kothari, A.; Barua, P.; Archunan, M.; Rani, K.; Subramanian, E.T.; Pujari, G.; Kaur, H.; Satyanarayanan, V.V.V.; Sarma, A.; Avasthi, D.K. ASPIRE: An automated sample positioning and irradiation system for radiation biology experiments at Inter University Accelerator Centre, New Delhi. *Radiation Measurements* 76 (2015) 17e22

5.3.2 Radiosensitization of A549 lung cancer cells with antiEGFR conjugated Au nanoparticles

Geetanjali Pujari, Asitikantha Sarma, Devesh Kumar Avasthi

Inter University Accelerator Centre, Aruna Asaf Ali Marg, New Delhi-110067

In this study, we have investigated the synergistic effect of antiEGFR conjugated Gold nanoparticle (antiEGFR-AuNP) with ^{12}C ion beam for enhanced cell killing on exposure to radiation. Epidermal Growth Factor Receptor (EGFR) is a key biomarker for lung cancer detection and its over expression leads to poor treatment and prognosis of the disease. Thus, we have made an approach to conjugate gold nanoparticles with antiEGFR monoclonal antibody for targeting EGFR of lung cancer cells, A549. The antiEGFR-AuNP treated cells are irradiated with different dose of ^{12}C ion beam to study the radiosensitizing property of antiEGFR-AuNP.

Cell Survival: Survival Fraction of ^{12}C ion beam irradiated A549 cells was compared with ^{12}C

ion beam irradiated antiEGFR-AuNP treated A549 cells. Treatment of A549 cells with antiEGFR-AuNP before radiation enhanced the cell killing at same dose of ^{12}C ion as studied by colony forming assay. There is approximately 30% dose reduction with antiEGFR-AuNP treatment prior to radiation in order to achieve 90% cell killing (Figure 5.3.2). Radiosensitization Enhancement Factor (REF) was calculated to be 1.5.

Nuclear Fragmentation: Detection of Apoptosis by Nuclear Fragmentation was studied and compared. We observed significant increase in nuclear fragmentation by antiEGFR-AuNP treatment in cells prior to radiation compared to respective control (Figure 5.3.3).

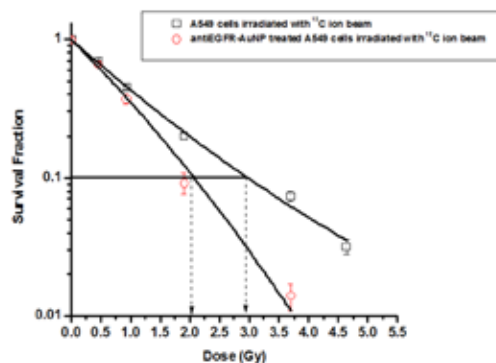


Fig. 5.3.2 Survival Fraction of ^{12}C ion beam irradiated A549 cells with or without antiEGFR-AuNP

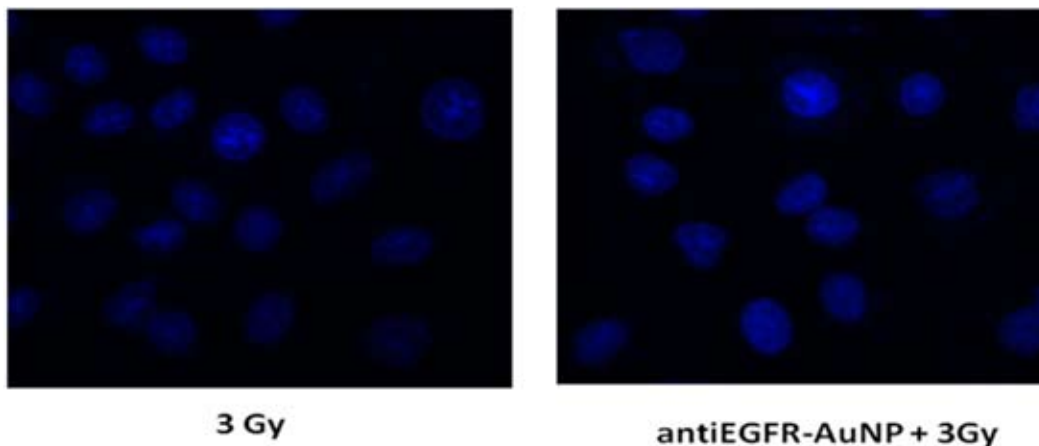


Fig. 5.3.3 Nuclear Fragmentation percent increased in A549 cells with antiEGFR-AuNP treatment prior to ^{12}C ion beam irradiation

EGFR Expression: The expression of EGFR in A549 cells was observed by Immunofluorescence. It is noticed that in unirradiated cells, the EGFR expression is present in the cytoplasmic region of the cells. Upon exposure of cells to radiation, the trend tends to change. Within 30 minutes after radiation exposure, the EGFR expression is seen in the nucleus but not remarkably in cytoplasm. This can be explained by the role of EGFR in DNA repair pathway. Several studies have shown association of EGFR with catalytic subunit of DNA dependent protein kinase (DNA-PKcs), that is a key enzyme of Non homologous end joining (NHEJ) pathway involved in the repair of DNA strand breaks. We measured the intensity of EGFR expression of these immunolabelled samples. It was observed that intensity of EGFR expression increased with increase in radiation dose. However, treatment of cells with antiEGFR-AuNP prior to radiation results in decrease in EGFR expression.

Cell cycle: Cell cycle distribution was studied by flow cytometry in A549 cells with or without antiEGFR-AuNP treatment prior to ^{12}C ion beam irradiation. We observed that A549 cells irradiated with ^{12}C ion beam showed accumulation of cells in G2/M phase with increase in radiation dose. On treatment of A549 cells with antiEGFR-AuNP prior to radiation increased the G2/M phase significantly compared to respective control. Similarly S-phase population also increased significantly with antiEGFR-AuNP pre treatment. The observation interprets that the treatment of

cells with antiEGFR-AuNP sensitizes the cells more compared to control cells by activating G2/M and S phase.

Targeted radiotherapy and use of monoclonal antibody to cancer therapy have been of much importance as this can lead to better result of survival with less risk of normal cells being damaged. At present, the clinical trials of anti EGFR-AuNP combined with radiotherapy in advanced non small cell lung carcinoma are under way. The treatment of A549 cells with antiEGFR-AuNP prior to radiation result in radiosensitization of A549 cells. EGFR inhibition leads to blocking the signalling cascade that leads to cell survival and proliferation. Presence of Au further enhances the response of radiation that is seen with increased cell death. Our results have showed increased radiosensitization of antiEGFR-AuNP treated cells compared to that of untreated cells. Almost 30% reduction of ^{12}C ion dose can be achieved with antiEGFR-AuNP pre treatment. Also Au nanoparticles may activate certain apoptotic enzymes that may lead to increase cell death. From our observation we can say that antiEGFR-AuNP sensitizes the cells more than the control by activating S and G2/M checkpoint proteins. This strategy could be used as a generalized approach for the treatment of lung cancer.

5.4 ATOMIC & MOLECULAR PHYSICS RESEARCH

5.4.1 Role of surface wake field in forming beam-foil circular Rydberg states

G. Sharma^{*1}, N. K. Puri^{*}, Adya P. Mishra[#], and T. Nandi^{†2}

^{*} Delhi Technological University, Shahbad Daultpur, Main Bawana Road, New Delhi 110042

[#]Atomic and Molecular Physics Division, Bhabha Atomic Research Centre, Trombay, Mumbai 400085

[†]Inter University Accelerator Centre, Aruna Asaf Ali Marg, New Delhi 110067

Beam foil is popularly known to populate Rydberg states abundantly with a vast range of n [1] in addition to plenty of low lying states. In this present work, we aim to understand the concerned excitation mechanisms responsible for, which is a long lasting debate. One set of analysis favors that these states are formed inside the bulk of the foil [2] while the other suggests for last layer effect [3]. By no means, such contradiction is acceptable; the experimental data can never be wrong, however, analysis can be faulty.

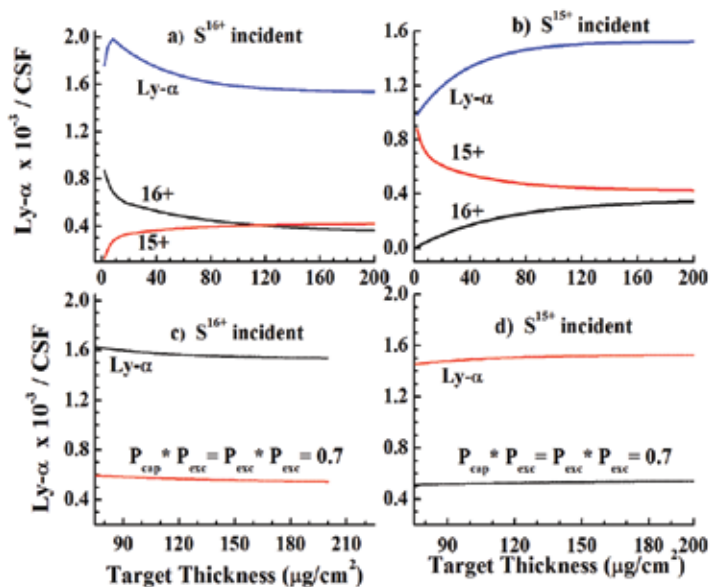


Fig. 5.4.1 Ly- α and CSF of S^{16+} and S^{15+} for incident ion: (a) S^{16+} (b) S^{15+} , whereas (c), (d) are weighted CSF (S^{16+} and S^{15+}) showing parallel behavior with Ly- α . Here P_{cap} & P_{exc} are capture and excitation probability, respectively

Keeping this fact in mind, we have decided to reanalyze the data set for Ly- α x-ray cross section reported as a function of foil thickness in Betz et al. [2]. Delayed Ly- α x-ray intensity for the incident ions S¹⁶⁺ and S¹⁵⁺ as a function of foil thickness are compared with charge state fraction (CSF) of S¹⁵⁺ and S¹⁶⁺ as obtained from the ETACHA code [4] in Fig. 5.4.1 (a) and (b). Fig. 5.4.1(a) shows that Ly- α intensity varies fairly parallel to CSF of S¹⁶⁺ except the low foil thickness region. Such parallelism at low thickness was not found [2] because the CSF was measured using magnetic spectrograph which involves atomic processes occurring inside the target and at the target surface.

In low foil thickness region, fraction of incident charge state dominates; however, both CSFs (S¹⁵⁺ and S¹⁶⁺) become comparable as it approaches to equilibrium thickness. Excitation of the electron in S¹⁵⁺ to Rydberg states is also possible at the last layers. Hence, it is highly plausible to consider that contribution to Rydberg states comes from both the ions, electron capture to S¹⁶⁺ in the Rydberg states and excitation from low lying states to the Rydberg states in S¹⁵⁺. Now an interesting point is to note that power law decay due to cascades from elliptic Rydberg states is ineffective at long delay (ns); only circular Rydberg states (CRS) would be prevalent [5]. Further, we see that surface wake field (SWF) strength [6] varies with foil thickness; SWF is small for low foil thickness and saturates with the thickness similar to charge equilibrium. If, the SWF plays a role in converting elliptic to CRS, we ought to notice the departures at the low foil thicknesses. Therefore present analysis includes the contribution from both the charge states S¹⁵⁺ and S¹⁶⁺ and assumed that the conversion from the elliptic to the CRS is taking place in the SWF region. The results are shown in Fig. 5.4.1(c) & (d). Interestingly we found total probability combining these two processes is high about 70%. To conclude, present model reveals the last layer effects on the Rydberg state formation in the beam-foil excitation and further suggests that the SWF plays a vital role in converting elliptical Rydberg states to CRS at the surface of the foil.

REFERENCES

- [1] H.G. Berry 1982 Ann. Rev. Nucl. Part. Sci. 32 1
- [2] H. -D. Betz *et al* 1983 Phys. Rev. Lett. 50 34
- [3] G. Schiwietz *et al.* 1987 Phys. Rev. Lett. 59 1561
- [4] J.P. Rozet *et al.* 1996 Nucl. Instr. Meth. B 107 67
- [5] T.Nandi 2008 Astrophys. J. 673 L103-L106
- [6] T.Nandi *et al.* 2013 Phys. Rev. Lett. 110 163203

5.4.2 Observations of autoionizing Rydberg states of Li-like V

G. Sharma*, Y. Kumar[#], K. Harish, G. Singh*, B. Kumar[†], S. Karmakar⁺, N. K. Puri*, A. P. Mishra[#], and T. Nandi^{††}

* Delhi Technological University, DTU, Delhi 110042

† Inter University Accelerator Center, IUAC, New Delhi 110067

[#]Atomic and Molecular Physics Division, Bhabha Atomic Research Centre, Trombay, Mumbai 400 085

^hAligarh Muslim University, Aligarh 2022002

[†]Jai Prakash Vishwavidyalaya, Chapra, Bihar 841301

^{††}Lalbaba College, 117 G.T. Road, Belur Math, Howrah 711202

Atomic Li and Li-like ions realize the simplest four-body Coulomb problem and when all three electrons are excited the system exhibits distinct electron–electron correlation effects. Several experimental such as [1] and theoretical investigations like [2], aiming at an understanding of this fundamental system, can be found in the literature. Review articles [e.g.3] have devoted to have detailed perspective on the system. All these works include H^2 , He-, Li atom to Li like Ne. However, no studies are available yet on this system in highly charged ions. Excitation mechanism of such exotic systems is an important aspect. The interactions between highly charged ions and solid surfaces [4] lead to the hollow states like triply excited states possible to form. Further, multi-electron capture from the surface by highly charged ions increases with its charge state. Hence, beam-foil excitation is a highly efficient technique to produce such exotic systems. Recently in our beam foil experiment with V ion beam of energies 100-150 on $80\mu\text{g}/\text{cm}^2$ C, certain transitions originating from short lived states and some others from long lived states are observed (Fig.5.4.2). Li-like states ($\tau \ll 1\text{ps}$) such as $2p^2np\ ^4S-1s^2p^2\ ^4P$ ($n \sim 12$) at 7keV and two doubly excited states of He-like V originating from long lived autoionizing Rydberg states decaying through two step single autoionization have been observed at delayed times of ~ 100 -150ps. First of these two is observed at 7.5keV and second at 11.6keV and assigned to decay of $3p^2\ ^3P-1s2p\ ^3P$ and $2s3p\ ^3P-1s^2\ ^1S0$ state. Transitions shown in Table 1 have been assigned by Hartee-Fock calculations with configuration interactions using the Cowan code.

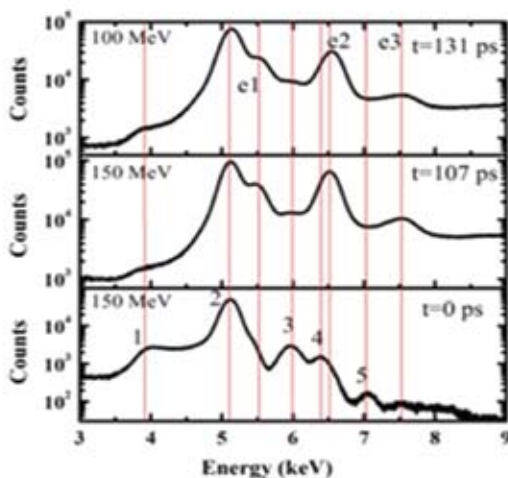


Fig. 5.4.2 Prompt (integers) and delayed lines (ei) observed in x-ray spectrum with different beam energies

Peak ³	E keV	Assignment	Theory
1	4.0	$1s2s2p\ ^4P_{5/2} - 1s^23s\ ^2S_{1/2}$	4.261 ⁺
		$1s2s2p\ ^4P_{5/2} - 1s^24s\ ^2S_{1/2}$	3.958 ⁺
		$1s2s2p\ ^4P_{5/2} - 1s^25s\ ^2S_{1/2}$	3.818 ⁺
2	5.12	$1s2p\ ^3P_2 - 1s^2\ ^1S0$	5.186 ^{&}
		$1s2s\ ^3S_1 - 1s^2\ ^1S0$	5.154 ^{&}
		$1s2s2p\ ^4P_{5/2} - 1s^22s\ ^2S_{1/2}$	5.142 ^{&}
e1	5.4	$2s\ ^2S_{1/2} - 1s\ ^2S_{1/2}$	5.43 ⁺
		$2p\ ^2P_{3/2,1/2} - 1s\ ^2S_{1/2}$	5.44 ⁺
		$2p^2\ ^3P_1 - 1s2p\ ^3P_2$	5.41 ^s
3	5.99	$1s3p\ ^3P_{0,1,2} - 1s^2\ ^1P_1$	6.11 ⁺
		$1s3s\ ^3S_1 - 1s^2\ ^1S0$	6.11 ⁺
		$1s2s3p\ ^4P_{5/2} - 1s^22s\ ^2S_{1/2}$	5.99 ⁺
	4.8	$1s2s3p\ ^4P_{5/2} - 1s^24s\ ^2S_{1/2}$	4.81 ⁺
	4.6	$1s2s3p\ ^4P_{5/2} - 1s^25s\ ^2S_{1/2}$	4.66 ⁺
4	6.35	$2p23p\ ^4S - 1s2p^2\ ^4P$	6.34 ^s
e2	6.5	$3d\ ^2D_{5/2,3/2} - 1s\ ^2S_{1/2}$	6.44 ⁺
		$2p\ ^2P - 1s\ ^2S^*$	6.442 ⁺
		$2s\ ^2S - 1s\ ^2S^*$	6.424 ⁺
5	7.0	$2p^212p\ ^4S - 1s2p^2\ ^4P$	6.966 ^s
e3	7.5	$3p^2\ ^3P - 1s2p\ ^3P$	7.344 ^s

Table 1. Assignment of transitions observed in the figure

REFERENCES

- [1] E. J. Knystautas et al. 1992 Phys. Rev. Lett. 69 2635
 [2] K. M. Aggarwal 2012 Phys. Scr 85 065301
 [3] L. B. Madsen 2003 J.Phys. B 36 R223
 [4] H. P. Winter and F. Aumayr 1999 J. Phys. B. 32 R39

5.4.3 Sudden Enhancement in Ionization of Projectile Ions at the Coulomb Barrier Energies

Prashant Sharma and Tapan Nandi

Inter University Accelerator Centre, Aruna Asaf Ali Marg, New Delhi-110067

We have measured the mean projectile charge state [1] due to ion-solid collisions as a function of ion-beam energies with special emphasis to studying the nature around the Coulomb barrier energies of the two body systems using the x-ray spectroscopy technique. A typical x-ray spectrum is shown in Fig. 5.4.3. The centroid of the projectile x-ray peak represents the mean charge state of the projectiles ions in the target. Since the mean charge state is varied with the projectile energy, the centroid of the x-ray peak keeps on shifting with the beam energies. The centroid energies are plotted against the beam energies as shown in Fig. 5.4.4. The curve so obtained exhibits an unusual kink at certain beam energy. Further, a dip observed around the same energy in the K-shell cross section versus beam energy plot as shown in Fig. 5.4.5. Such observations cannot be explained in terms of any atomic processes involved in the ion-solid collisions. Thorough analysis suggests that the extra contribution to the ionization must be originating from some other sources. Since, the kink occurs right at the Coulomb barrier for different two body systems, the strong nuclear force can be responsible to alter the ionization process. Consequently we attribute the phenomenon to the momentary increment of the effective nuclear charge of the projectile ion while crossing the strong force regime.

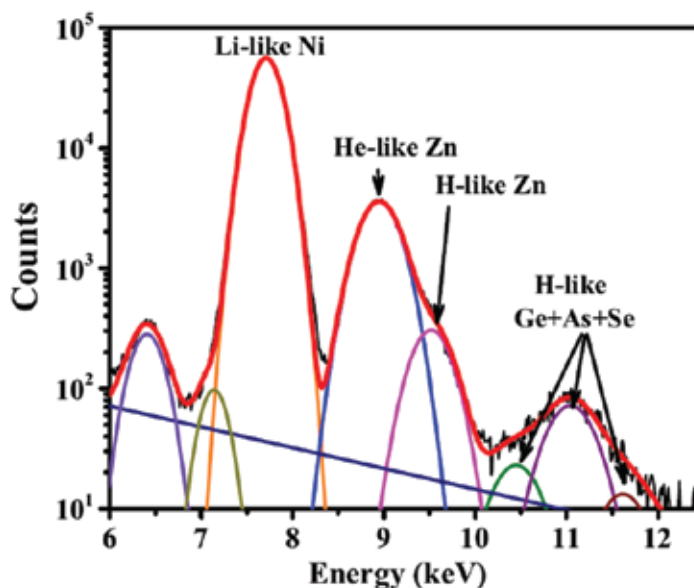


Fig. 5.4.3 . Typical x-ray spectrum for ion-solid collisions at $t=0$ for 156 MeV Ni^{12+} on 80 g/cm^2 carbon foil showing x-ray peaks from projectile and projectile-like fragment ions including compound nucleus (see text). Projectile x-ray peak corresponds to many unresolved charge states. Its centroid represents x-ray line energy corresponding to the mean charge state.

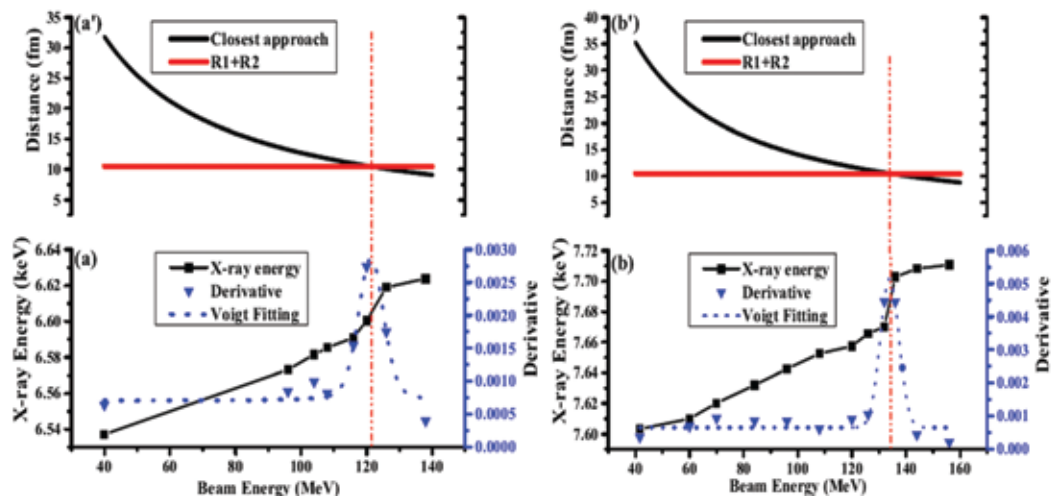


Fig. 5.4.4 Centroid of the projectile x-ray peaks versus beam energies (a) Fe beam and (b) Ni beam on $80 \mu\text{g}/\text{cm}^2$ C-foil. Closest approach or touching distance versus beam energy for two body system of (a') ^{56}Fe on ^{12}C and (b') ^{58}Ni on ^{12}C . Error bars are tiny and smeared in the symbol size. All solid lines are to guide eye only. The dash-dot vertical lines represent the Coulomb barrier of the corresponding systems, which are just centroid of the Voigt function of the kink observed.

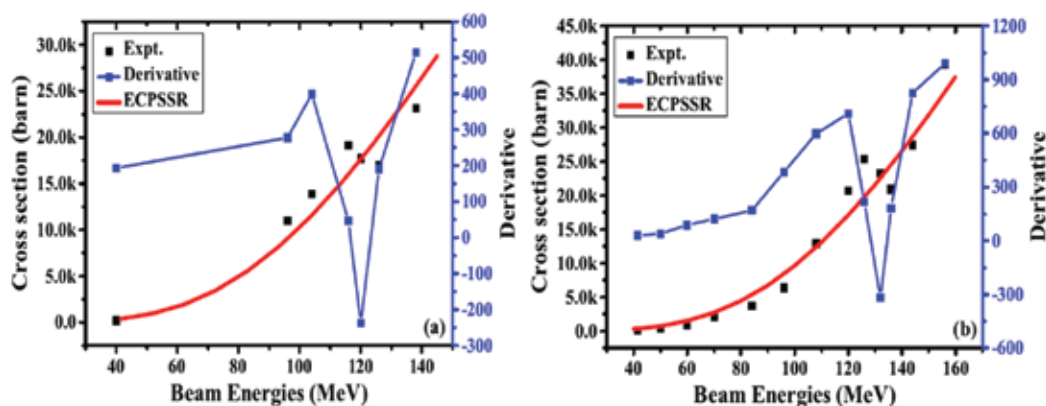


Fig. 5.4.5 K-shell ionization cross section versus beam energies (a) Fe beam and (b) Ni beam on $80 \mu\text{g}/\text{cm}^2$ C-foil. The ionizations cross sections are calculated from ECPSSR code [2]. Error bars are tiny and smeared in the symbol size. All solid lines are to guide eye only. Theoretical curves are smooth throughout, whereas the experimental curves exhibit dips around the corresponding Coulomb barrier energies as more clearly visible in the derivative spectra.

REFERENCES

- [1] V. P. Shevelko et al., Nucl. Instruments Methods Phys. Res. B 269, 1455 (2011).
- [2] J. P. Rozet et al., Nucl. Instruments Methods Phys. Res. B 107, 67 (1996).

5.4.4 A parameterized model for Coulomb barrier heights

D. Swami, P. Sharma and T. Nandi

Inter University Accelerator Centre, New Delhi-110067

Coulomb barrier height is a basic parameter to describing the nuclear reactions. Recently it is found that ions produce from nuclear reactions can be used to study electron loss and capture processes. Hence determining the Coulomb barrier becomes important in both nuclear and atomic physics. The different models such as the CCFULL & WONG [1] and CW [2] are used to calculate the barrier heights. Moreover, the parametrized formula can be developed from the experimentally obtained barrier heights. We have formulated one of such formula and compared the results with several models including the CCFULL & Wong and CW, and with available experimental data.

It is known that the Coulomb barrier (V_c) is defined as

$$V_c = \frac{Z_p Z_t e^2}{R} \quad \text{and} \quad R = R_c (A_p^{\frac{1}{3}} + A_t^{\frac{1}{3}}) \quad (1)$$

where Z_p and Z_t represent the charge numbers of projectile and target nuclei, respectively, $e^2 = 1.44$ MeVfm, A_p and A_t stand for the mass numbers of projectile and target nuclei, respectively; R_c is the composite radius. The R_c taken the major role in above equation as except this all others are physical constants. One may notice that different values of R_c are used in the literature ranging from 1.1 to 1.4 fm [13].

In this report experimental data available in the literature have been used to plot $\frac{d^2(\sigma E)}{dE^2}$ vs E and then the major peak was fitted with a Gaussian function. The centroid of the peak represents the Coulomb barrier height and the FWHM the uncertainty. According to this Coulomb barrier height, the value of R_c has been calculated from equation (1) and plotted against charge product $Z_p Z_t$ of the corresponding binary systems as shown in Figure 5.4.6. It is to note that R_c varies from 1.4 to 1.8. The curve so obtained has been fitted with a parameterized function given in following equation.

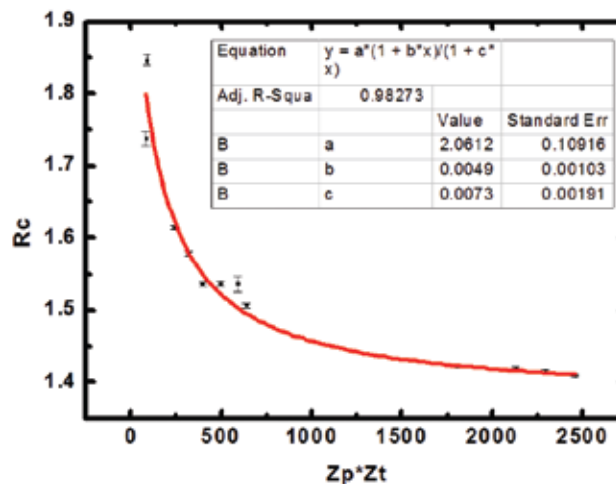


Fig. 5.4.6 Composite radius (R_c) is plotted against charge product ($Z_p Z_t$).

$$R_c = a \times \frac{(1-b*Z_p Z_t)}{(1+c*Z_p Z_t)} \quad \text{where } a = 2.06127, b = 0.00493, c = 0.00739 \quad (2)$$

Equation (2) have been used to estimate the Coulomb barrier height for an unknown binary system and the corresponding error in the barrier height is evaluated by

$$\Delta V_c = \pm \frac{\Delta R_c}{R_c} V_c = \left(\frac{\Delta a}{a} + \frac{\Delta b Z_p Z_t}{1+b Z_p Z_t} - \frac{\Delta c Z_p Z_t}{1+c Z_p Z_t} \right) V_c \quad (3)$$

Where $\Delta a = 0.10916$, $\Delta b = 0.00103$, $\Delta c = 0.00191$ as obtained from the fitting errors. According to this R_c , Coulomb barrier of different binary systems have been calculated and compared with different models and experimental results in the following table.

Table: Comparison of experimental CB heights for various binary systems with different model predictions. CCFULL & WONG allow only that system having charge product $Z_p Z_t$ less than 1800.

System	Experimental	CW	CCFULL	WONG	Ours
$^{32}\text{S}+^{90}\text{Zr}$	79.88±0.174 [3]	79.31	81.58±0.03	81.62±0.03	80.52±0.21
$^{32}\text{S}+^{96}\text{Zr}$	78.88±0.165 [3]	78.59	79.55±0.03	79.58±0.03	79.51±0.20
$^{40}\text{Ca}+^{124}\text{Sn}$	114.09±0.29 [4]	115.81	121.66±0.02	121.70±0.02	117.57±0.01
$^{40}\text{Ca}+^{132}\text{Sn}$	115.18±0.35 [4]	114.76	120.29±0.02	120.32±0.02	116.12±0.01
$^{48}\text{Ca}+^{124}\text{Sn}$	114.16±0.30 [4]	113.67	118.90±0.03	118.93±0.03	114.65±0.01
$^{48}\text{Ca}+^{132}\text{Sn}$	112.86±0.16 [4]	112.66	117.60±0.03	117.63±0.03	113.27±0.01
$^{16}\text{O}+^{154}\text{Sm}$	58.99±0.094 [5]	60.29	60.41±0.03	60.46±0.03	59.55±0.22
$^{16}\text{O}+^{144}\text{Sm}$	59.72±0.088 [5]	60.96	61.19±0.03	61.24±0.03	60.46±0.22
$^{16}\text{O}+^{186}\text{W}$	67.44±0.46 [5]	69.76	70.43±0.03	70.47±0.03	68.94±0.20
$^{16}\text{O}+^{92}\text{Zr}$	41.52±0.09 [5]	42.14	41.35±0.58	41.41±0.001	41.49±0.17
$^6\text{Li}+^{64}\text{Ni}$	11.95±0.075 [6]	12.61	11.01±0.25	11.12±0.12	11.56±0.09
$^6\text{Li}+^{64}\text{Zn}$	12.07±0.054 [7]	13.51	12.00±0.32	12.12±0.001	12.47±0.09
$^7\text{Li}+^{64}\text{Zn}$	12.10±0.057 [7]	13.36	11.87±0.36	11.97±0.11	12.26±0.09
$^{17}\text{O}+^{64}\text{Zn}$	32.55±0.058 [8]	33.12	31.97±0.30	32.02±0.02	32.41±0.10
$^{16}\text{O}+^{124}\text{Sn}$	49.95±0.08 [9]	50.33	49.90±0.25	49.95±0.03	49.55±0.20
$^{18}\text{O}+^{120}\text{Sn}$	49.70±0.19 [9]	50.10	49.65±0.25	49.69±0.03	49.25±0.20
$^{18}\text{O}+^{124}\text{Sn}$	49.49±0.18 [9]	49.84	49.35±0.009	49.40±0.002	48.89±0.20
$^{56}\text{Fe}+^{12}\text{C}$	21.41±0.11	22.62	21.14±0.41	21.21±0.02	21.69±0.002
$^{58}\text{Ni}+^{12}\text{C}$	23.08±0.055	24.24	22.79±0.41	22.86±0.02	23.36±0.01
$^{16}\text{O}+^{16}\text{O}$	10.61 [10]	10.52	9.12±0.32	9.22±0.002	9.93±0.12
$^{16}\text{O}+^{40}\text{Ca}$	23.06 [10]	23.64	22.21±0.02	22.28±0.001	22.96±0.003
$^{40}\text{Ca}+^{40}\text{Ca}$	52.8 [10]	53.65	53.93±0.01	53.97±0.002	54.38±0.22
$^{40}\text{Ca}+^{48}\text{Ca}$	52.00 [10]	52.51	51.27±0.01	51.31±0.001	52.73±0.22
$^{48}\text{Ti}+^{208}\text{Pb}$	191.04±0.18 [11]	189.90			190.97±0.64
$^{56}\text{Fe}+^{208}\text{Pb}$	221.96±0.42 [11]	221.05			222.34±0.94
$^{64}\text{Ni}+^{208}\text{Pb}$	235.37±0.30 [11]	234.85			235.70±1.08
$^{70}\text{Zn}+^{208}\text{Pb}$	250.17±0.20 [11]	249.29			249.91±1.23
$^{54}\text{Cr}+^{208}\text{Pb}$	205.8 [12]	204.79			205.75±0.79

Our model does not have any limitation on $Z_p Z_t$ like the model CW. It is evident from table 1 that the predictions from our model are in good with accord with other models and experimental values. Further only our model predicts uncertainty in the calculated values.

REFERENCES

- [1] K. Hagino et.al., Comput. Phys. Commun. 123, 14 (1999).
- [2] P. R. Christensen et.al., Phys. Lett. 65, 19 (1976).
- [3] C. Beck, FIAS Interdisciplinary Science Series 2013, pp 105-118.
- [4] J. Kolata, et.al. Phys. Rev. C 85, 1 (2012).
- [5] J. C. Mein, et.al. Nucl. Phys. A 584, 190 (1995).
- [6] M. Shaikh, et.al. DAE Symp 58, 360 (2013).
- [7] M. Zadro, et.al. Phys. Rev. C87, 054606, (2013).
- [8] J. Huiza, et.al. Phys. Rev. C 82, 1 (2010).
- [9] S. Sinha, et.al. Phys. Rev. C64, 246071 (2001).
- [10] K. Washiyama, et.al. Phys. Rev. C78, 1 (2008).
- [11] G. Pollarolo, et.al. Phys. Rev. Lett. 100, 1 (2008).
- [12] S. Mitsuoka, et.al. Phys. Rev. Lett. 99, 1 (2007).
- [13] Nuclear Physics by D.C. Tayal, Himalaya Publishing House, 1997.

5.5 ACCELERATOR MASS SPECTROMETRY RESEARCH

5.5.1 Geochronological Applications of Cosmogenic Radionuclides in the Neogene-Quaternary Deposits of Siwaliks (Himachal Pradesh) and Narmada Valley (Madhya Pradesh)

Navjot Kaur¹, Rajeev Patnaik¹, Pankaj Kumar², Rajeev Sharma² and Sundeep Chopra²

¹ Department of Geology, Panjab University, Chandigarh-160014

² Inter University Accelerator Center, Aruna Asaf Ali Marg, New Delhi-110067

Recent developments in accelerator mass spectrometers allow precise analysis of cosmic-ray produced nuclides in terrestrial materials. Cosmogenic nuclides (³He, ²¹Ne, ¹⁰Be, ²⁶Al, & ¹⁴C) build-up predictably with time in minerals exposed to cosmic rays. Measuring their concentrations permit determination of how long rocks have been exposed at or near the surface of the earth. Production rates of these radionuclides vary with location and time and are scaled to account for a number of factors including depth within a target, altitude and latitude, topographic shielding and sample surface slope. Half life of ¹⁰Be is 1.36×10^6 years and that of ²⁶Al is 7.17×10^5 years, both of these cosmogenic radionuclides are very useful for analyzing Quaternary and Late Tertiary period. Study areas include Siwaliks and Narmada valley deposits. Siwaliks range in age varies from Middle Miocene to Lower Pleistocene, representing the last ~18 million years of continuous sedimentary and fossil record. A distinct faunal as well as floral turnover is observed at the Neogene-Quaternary Boundary coinciding with the Tatrot -Pinjor Boundary in India. At about this time (2.6 Ma) a global change towards a cooler, drier and more variable climate associated with the Northern Hemisphere glaciations has been observed and monsoonal circulation was also greatly strengthened by the Plio-Pleistocene uplift of the Himalaya.

Recent works on magnetic stratigraphy of Siwalik sequences show immense potential for palaeomonsoonal studies in the Siwaliks. Direct evidence for repeated human occupation is shown by many sites from Lower Paleolithic to the Chalcolithic Period in Narmada Valley. The stratigraphy comprises a basal conglomerate and gravel layer, the 'Boulder Conglomerate'. Quartz is present in closed system between the boulder conglomerates making it a very good area for cosmogenic radionuclide dating. Narmada Valley is important for human origin studies. Therefore, dating various sections in this area containing fossil human remains and palaeoclimatic reconstruction will help in understanding evolution of hominids.

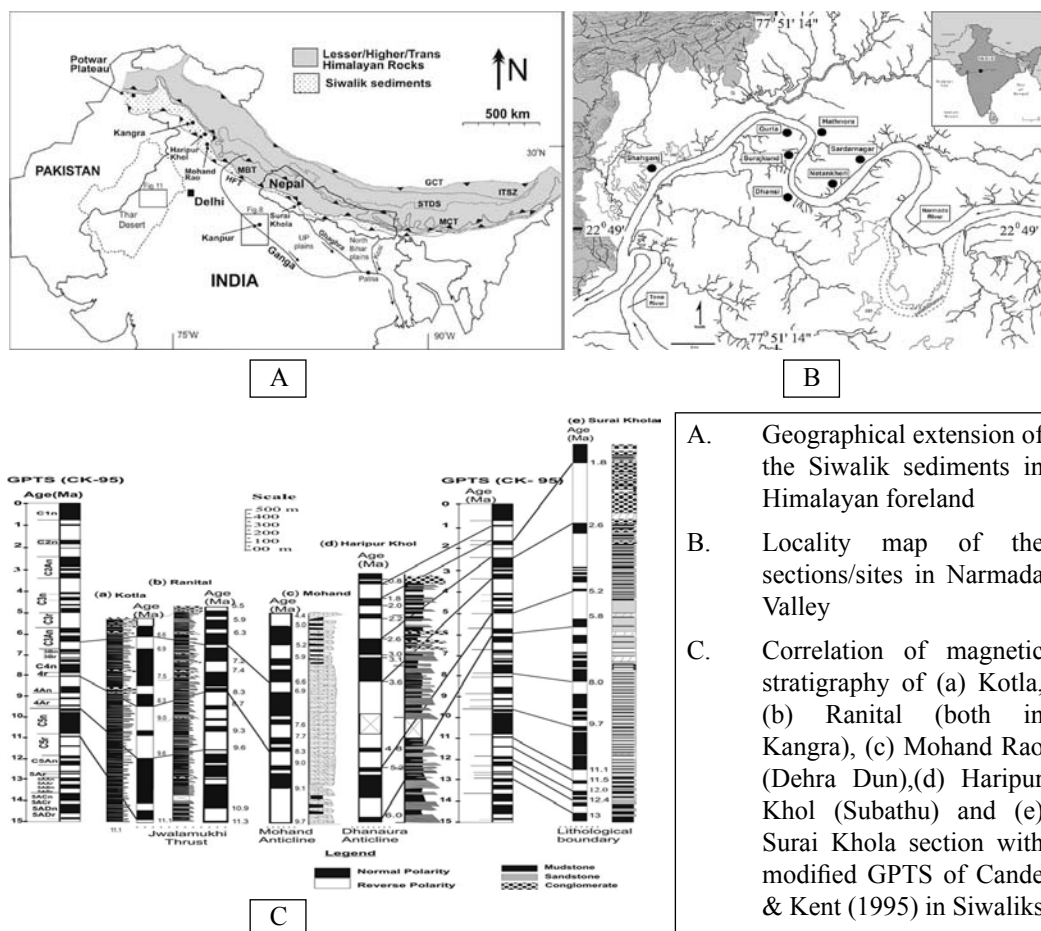


Fig. 5.5.1

The primary objectives of studies in these two areas are to use the cosmogenic nuclide production rate to infer climatic activities at that point of time to know palaeoclimates such as palaeomonsoon variability and to use the palaeoclimate data to understand the influence of past climate changes on the emergence and evolution of hominids in India. For both ^{10}Be and ^{26}Al analysis, generally quartz is taken because it is a ubiquitous, resistant mineral that can be systematically cleaned of meteoric Be_{10} . Therefore, quartzitic pebbles and sand have been collected from the study area i.e. Dhansi, Pilikarar, Surajkund Formation of Narmada Valley and Siwaliks areas near Paonta Sahib, Nahan, Ghaggar River and Khetpurali.

Pure quartz was obtained by selective dissolution in a hot ultrasonic bath or a shake table, A carrier of Be^9 (~ half a milligram in solution) was added to the pure quartz mineral separate and then it was completely dissolved with concentrated HF and HNO_3 . Be and Al were separated and purified with ion exchange methods and selective PH precipitation. The chemical processing work is carried out at clean chemistry laboratory at IUAC.

Ratios of $^{10}\text{Be}/^9\text{Be}$ or $^{26}\text{Al}/^{27}\text{Al}$ will then be measured with Accelerator Mass Spectrometer (AMS) at IUAC. After dating with Be^{10} and Al^{26} isotopes, the results will be correlated with the already existing data of Siwaliks and Narmada valley. For Example, in Siwaliks, the observed data will be correlated with the existing palaeomagnetic logs. This data will be considered as a standard and will be applied to undated sites/sections.

REFERENCES

- [1] Kohl, C.P., Nishizumi, K. 1992. Chemical isolation of quartz for measurement of in-situ produced cosmogenic nuclides. *Geochimica et Cosmochimica Acta*, 56: 3583-3587.
- [2] Lal, D. 1991. Cosmic ray labeling of erosion surfaces: in-situ nuclide production rates and erosion models. *Earth and Planetary Science Letters*, 104: 424-439.
- [3] Patnaik, R., Chauhan, P.R., Rao, M.R. 2009. New geochronological, paleoclimatological, and archaeological data from the Narmada Valley hominin locality, central India. *Journal of Human Evolution*, 56: 114-133.
- [4] Sangode, S. J., Kumar, R. & Ghosh, S. K. 2003. Magnetic Polarity Stratigraphy of the Late Miocene Siwalik Group sediments from Kangra Re-entrant, H.P., India. *Himalayan Geology*, 24: 47-61.
- [5] Sanyal, P., Bhattacharya, S. K., Kumar, R., Ghosh, S. K. & Sangode, S. J. 2004. Mio Pliocene monsoonal record from Himalayan Foreland basin (Indian Siwalik) and its relation to the vegetational change. *Palaeogeography, Palaeoclimatology, Palaeoecology*, 205: 23-41.

5.5.2 Cosmogenic ^{10}Be dating of the samples collected from different locations to determine their palaeoenvironmental implications

Amit Kumar¹, Meenakshi¹, Nishi Rani¹, J.P. Shrivastava¹, Pankaj Kumar², Rajveer Sharma², Sundeep Chopra², G. S. Roonwal²

¹Department of Geology, University of Delhi, New Delhi-110007

²Inter-University Accelerator Centre, New Delhi-110067

Samples are collected from three different localities (from Mandla lobe, Lonar crater lake; India and East Pacific rise); Fig-1, to determine their Palaeoenvironmental implication using ^{10}Be dating. Cosmogenic ^{10}Be produced by cosmic ray spallation reaction of O and N atoms which gets react with water due to its low pH (5.5) and accumulates at the soil surface, where its relatively long half-life (1.36 m.y.) permits a long residence time before decaying to ^{10}B . ^{10}Be and its daughter product have been used to examine soil erosion, soil formation from regolith, the development of lateritic soils and the age of ice cores (Shrivastava et al., in press).

Samples are:-

Samples	Area and Location	Material Type
PLB-0	Patna-Longhatola- Badargarh, M.P., India <i>22° 59' 08" N, 81° 37' 25" E</i>	Red bole
Lonar (Outer rim)	Lonar Crater, Buldana dist., Maharashtra, India <i>19.97° N, 76.51° E</i>	Glass rock
EPR	149G East Pacific Rise, Pacific Ocean <i>21°28.85' S, 114°16.60' W</i>	Glass rock
	338G <i>14°26.85' S, 112°35.94' W</i>	Glass rock
	403G <i>8030'18" S, 1070 29'W</i>	Glass rock

PLB-0 sample was collected from Mandla lobe (Eastern Deccan traps) and volcanic eruption occurs at K/T boundary (63 M.y.). They marks quiescent period between two volcanic eruptions and the exposure time of bole horizon was very less. Impact glass was collected from Outer rim of Lonar Crater Lake. The crater was created by the meteorite impact during the Pleistocene epoch and the age of its creation is described to be 5.7 m.y. \pm 47,000 years. Outer ejecta blanket and alluvial soil,

highly weathered zone, moderately to highly weathered zone, moderately weathered zone, and core and the sample carried out for digestion is from highly weathered zone (Nayak, V.K, 1971). Being weathered it contains normative quartz which might have trapped the ^{10}Be atoms produced in-situ conditions. Dark grey colored glass rock samples (*EPR* 149G, 338G and 403G) belong to S040 and S062 series were collected (by GSR) onboard research vehicle Sonne during two German expeditions 'GEOMETEP IV and V', consist of both fresh and altered mid-oceanic ridge basalts (Pandey et al., 2009). East Pacific Rise (EPR), that defines plate boundary between the Pacific and Nazca Plate, is a part of more than 60,000 km long global network of Mid-Oceanic Ridges and lies on the floor of the South Pacific Ocean.

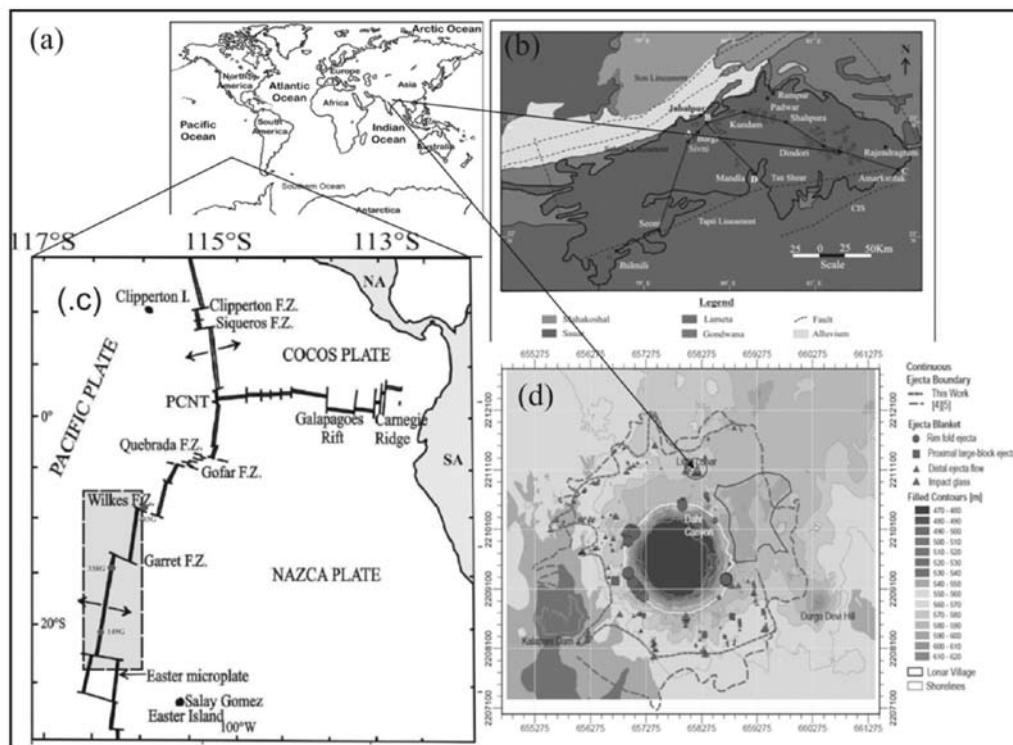


Fig. 5.5.2 Location map of samples collected for cosmogenic ^{10}Be dating

All the five samples were processed in IUAC (Inter University Accelerator Centre, New Delhi) chemistry lab under the supervision of Mr. Pankaj Baghel and Mr. Rajveer Sharma. Samples were crushed (250-500 micron) and treated with 1:1 conc. HCl: MQ, 0.03% H_2O_2 (acid bath), which later on leached using the same reaction mixture as in acid bath. Further the reaction mixture is treated with 4:1:1 HF: HNO_3 : MQ for Microwave digestion which is passed through anion and cation columns after addition of the ^9Be carrier (spike solⁿ). Collected solⁿ is precipitated at pH 8-10 and then heated in furnace to convert BeOH to BeO which is packed in quartz vials for Accelerator Mass Spectrometer (AMS) loading.

REFERENCES

- [1] Nayak, V.K. (1971) Glass objects (Impactite glasses?) A possible new evidence for meteoritic origin of the lunar crater, Maharashtra state, India; Earth and planetary science Lettr. v.14, pp.1-6.
- [2] Pandey, S. K., Shrivastava, J. P. and Roonwal, G. S. (2009) Petrography and Mineral Chemistry of Neovolcanics occurring between Pacific and Nazca Plate Boundaries; Jour. Geol. Soc. of India, v.74, pp.559-572.
- [3] Shrivastava, J.P. (in press) Cosmogenic ^{10}Be dating of the clay sediments associated with the intra-volcanic bole horizons of the Deccan Traps: palaeoenvironmental implications and duration of volcanism at KTB.